DM

Alternative Methods for the Synthesis of Electrically Conductive Bacterial Cellulose-polyaniline Composites for Potential Drug Delivery Application

MASTER DISSERTATION

Pedro Emanuel de Gouveia Alonso
MASTER IN APPLIED BIOCHEMISTRY

UNIVERSIDADE da MADEIRA
A Nossa Universidade
www.uma.pt

April | 2017

Alternative Methods for the Synthesis of Electrically Conductive Bacterial Cellulose-polyaniline Composites for Potential Drug Delivery Application

MASTER DISSERTATION

Pedro Emanuel de Gouveia Alonso
MASTER IN APPLIED BIOCHEMISTRY

SUPERVISOR
Nereida Maria Abano Cordeiro

UNIVERSIDADE da MADEIRA

Laboratório Biomateriais Bioanálises
PhytoBank - Microalgae Collection of Madeira

Alternative synthesis methods of electrically conductive bacterial cellulose-polyaniline composites for potential drug delivery application

Tese apresentada à Universidade da Madeira com vista à obtenção do grau de Mestre em Bioquímica Aplicada

Pedro Emanuel de Gouveia Alonso

Sob a orientação de:
Professora Doutora Nereida Maria Abano Cordeiro

Faculdade de Ciências Exatas e da Engenharia
Universidade da Madeira
Funchal – Portugal

Abril 2017

Acknowledgments

The accomplishment of this Master Thesis was only possible with the help of several people who I am truly grateful for them being part of my daily life.

I would like to thank Prof. Dr. Nereida Cordeiro for the guidance, support, share of ideas and constructive critics which were crucial to make this work possible.

I would also give a big thank you to my work colleagues Marisa Faria, Igor Fernandes and Tomásia Fernandes for pushing me out of my comfort zone and for helping me being the person I am today. A special hug to Marisa Faria for being a mentor and for giving me the knowledge and support that made this work possible to conclude.

I am grateful to Prof. Dr. Gabriel Gomes (Physics Department, University of Madeira, Portugal) for creating the electrical conductivity measurement system, by the availability shown, as also by clarifying any doubts regarding the measurements.

I want to acknowledge the help provided by the laboratory technicians Paula Andrade and Paula Vieira for providing the reagents as also to laboratory technician Adriano Faria for providing me the laboratory equipment and space for the antimicrobial measurements.

I would like to thank Dr. Carla Miguel (CQM, University of Madeira, Portugal) by providing me help with the contact angle measurements as also to Prof Dr. Paula Castilho (CQM, University of Madeira, Portugal) for providing me the ATR accessory.

I would like to thank Prof. Dr. Manuela Gouveia (University of Madeira, Portugal) for providing me the *Eschericia coli (E. coli)* strain as also the conditions to make the experiment successful.

I am truly grateful to prof Dr. Artur Ferreira (CICECO, University of Aveiro, Portugal) for making the TGA and XRD analysis, to Prof. Dr. Faranak Mohammadkazemi (New Technologies and Energy Engineering, Shadid Beheshti University, Iran) for the EDX analysis and for Dr. Matic Resnik (Department of Surface Engineering and Optoelectronics, Jožef Stefan Institute, Slovenia) for the AFM analysis, which substantially increased the quality of the current Master Thesis.

I want to give a big hug to my friends Magda Santos, Lisandra Sousa, Paulo Costa, Anísia Martins, Dina Maciel and Micael Leça for the support and motivation during this work.

I want to demonstrate my love to my mommy Adelaide Gouveia and auntie Leonor Gouveia for the unconditional love, support and care throughout my entire existence, which made me possible to get up to this point in life.

I would also like to thank to all whom, directly or indirectly, contributed to this thesis.

Abstract

Bacterial cellulose/polyaniline (BC/PANi) nanocomposites have been lately receiving attention by the scientific community towards the development of electronic applications. The current work aims to determine the most suitable BC modification method to obtain an effective drug delivery membrane through electric stimulus. Thus, the BC/PANi nanocomposites were synthesized through the employment of different BC matrixes (drained, freeze dried and regenerated), as well as through different polymerization methods (*in situ* and *ex situ*). Prior to modification, the effects of both drying methods (freeze drying and oven drying), and regeneration process on BC structure were studied. By freeze drying BC, the fibril network is preserved, leading to a more porous material. On the other hand, regenerated BC presented a compact surface due to the incapacity to reorganize into fibrils during the regeneration process. This way, freeze dried BC should be more suited for modification. To obtain a highly conductive nanocomposite, the *in situ* polymerization on drained BC should be employed. The introduction of PANi onto BC obstructed the pores, which led into a more compact and rougher material. Also, a decrease in the thermal stability, as well as a decrease in the BC crystallinity was observed. The nanocomposites were drug loaded with sodium sulfacetamide to evaluate the antimicrobial activity. It was observed that without electrical stimulus, only drug loaded drained *in situ* BC/PANi nanocomposite presented an inhibitory effect onto the *Escherichia coli (E. coli)* growth (13%). By applying electric stimulus onto this membrane, the inhibition in *E. coli* growth is further evidenced (20%). This way, *in situ* polymerization of aniline on drained BC presented to be an effective method to create a highly conductive membrane for drug release through electrical stimulus.

Keywords: Bacterial cellulose, Polyaniline, cellulose modification, antimicrobial activity, electrical stimulus, inverse gas chromatography

Resumo

Os nanocompósitos de celulose bacteriana/polianilina (CB / PANi) têm recebido nos últimos tempos um grande interesse por parte da comunidade científica para o desenvolvimento de aplicações eletrónicas. Este trabalho tem como objetivo determinar o método de modificação mais adequado da CB para a obtenção de uma membrana eficaz na libertação de fármacos através de estímulo elétrico. Assim sendo, os nanocompósitos CB/PANi foram sintetizados utilizando diferentes matrizes de CB (drenada, liofilizada e regenerada) bem como através de diferentes métodos de polimerização (*in situ* e *ex situ*). Antes da modificação, foram estudados os efeitos tanto do método de secagem (liofilização e secagem no forno) como também o processo de regeneração na estrutura da CB. O processo liofilização levou à preservação da estrutura tridimensional, obtendo assim um material mais poroso. Por outro lado, a CB regenerada apresentou uma superfície compacta devido à incapacidade de reorganizar-se em fibrilas durante o processo de regeneração. Desta forma, a CB liofilizada aparenta ser a matriz mais adequada para modificação. Contudo, relativamente aos diferentes nanocompósitos obtidos, para se obter uma membrana com elevada condutividade, o método mais adequado é a polimerização *in situ* na CB drenada. A introdução de PANi na CB obstruiu os poros, levando à formação de um material mais compacto e rugoso. Também foi observado uma diminuição na estabilidade térmica bem como uma diminuição na cristalinidade da CB. A sulfacetamida de sódio foi incorporada nos nanocompósitos para avaliar a atividade antimicrobiana onde, sem estímulo elétrico, apenas o nanocompósito *in situ* com CB drenada apresentou um efeito inibitório sobre o crescimento de *Escherichia coli (E. coli)* (13%). Através da aplicação de estímulo elétrico sobre esta membrana, a inibição no crescimento de *E. coli* é potenciado (20%). Assim sendo, a polimerização *in situ* da anilina numa membrana drenada mostrou ser eficaz na libertação do fármaco por estímulo elétrico.

Palavras-chave: celulose bacteriana, polianilina, modificação da celulose, atividade antimicrobiana, estímulo elétrico, cromatografia gasosa inversa

Index

Figure captions

Table captions

List of abbreviations

ΔG_s^d– Surface Gibbs free energy of the dispersive component

ΔG_s^{sp} – Surface Gibbs free energy of the specific component

γ_L^D – Liquid surface tension

γ_S^- – Donor number of the probe

γ_S^+ – Acceptor number of the probe

γ_S^D – Dispersive component of the surface energy

γ_S^{SP} – Specific component of the surface energy

γ_S^{Total} – Total surface energy

ΔG_a^M – Distance between the probe and the alkane line

^{13}C NMR – Carbon–13 nuclear magnetic ressonance

A – Adsorption potential

a_m – Cross section area of the probe molecule

FTIR–ATR – Fourier transformed infrared coupled with attenuated total reflectance

BC – Bacterial cellulose

CI – Crystallinity index

CrS – Crystallite size

DMAc – Dimethylacetamide

dTGA – Derivative of TGA

EDX – Energy dispersive X–ray spectroscopy

ES – Oven dried BC/PANi nanocomposite obtained through *ex situ* polymerization

F – Carrier gas (helium) flow rate

FD–BC – Freeze dried bacterial cellulose

FD–ES – Freeze dried BC/PANi nanocomposite obtained through *ex situ* polymerization

FD–IS – Freeze dried BC/PANi nanocomposite obtained through *in situ* polymerization

FID – Flame ionization detector

GC – Gas chromatography

H – Height equivalent to the theoretical plate

HOMO – Highest occupied molecular orbital

HS – Hestrin and Schramm culture medium

I – Current

$\mathbf{I_{110}}$ – Intensity of the crystallinity region

$\mathbf{I_{am}}$ – Intensity of the amorphous region

ICP – Intrinsically conductive polymers

IGC – Inverse gas chromatography

D–IS – Oven dried BC/PANi nanocomposite obtained through *in situ* polymerization

j – James–Martin compressibility factor

LB–ASDA – Low–bond axisymmetric drop shape analysis approach

LUMO – Highest unoccupied molecular orbital

$\mathbf{N_A}$ – Avogadro number

$\mathbf{n_m}$ – Monolayer capacity

OD–BC – Oven dried BC

p – Adsorbate pressure

$\mathbf{p_0}$ – Gas pressure

PANi – Polyaniline

R – Perfect gas constant

R–BC – Regenerated bacterial cellulose

R–IS – Regenerated BC/PANi nanocomposite obtained during *in situ* polymerization

$\mathbf{S_{BET}}$ – Brunauer–Emmett–Teller surface area

SEM – Scanning electronic spectroscopy

$\mathbf{SW_{max}}$ – Swelling maximum

TCD – Thermal conductivity detector

TGA – Thermogravimetrical analysis

$\mathbf{t_R}$ – Retention time

UDP–Glucose – Uridine diphosphate glucose

V – Voltage

$\mathbf{V_g}$ – Specific retention volume

$\mathbf{V_N}$ – Retention volume

$\mathbf{W_{adh}}$ – Work of adhesion

$\mathbf{W_{coh}}$ – Work of cohesion

XRD – X–Ray diffraction spectroscopy

Z – Z value of the I_α and I_β cellulose

ρ – Resistivity

σ – Conductivity

Chapter I – Introduction

1.1 – Cellulose

Cellulose is the most abundant biopolymer found in nature, being produced by plants, tunicates, algae and some bacteria (1). In plants, this polymer is associated with hemicellulose and lignin, and in order to obtain pure cellulose it requires harsh chemical (alkali or acid) treatment (2). Bacterial cellulose (BC) is the most pure form of cellulose found in nature, where it does not have any of the aforementioned impurities present in plant cellulose (3).

From a chemical point of view, cellulose is a homopolymer consisting of glucose monomers linked by β–1,4 glucosidic bonds in such a way that one monomer is rotated 180º relative to the other (2). It also possesses three hydroxyl groups per monomer, which gives cellulose a highly hydrophilic behaviour (4). This confers to cellulose the ability to interact via inter– and intra– hydrogen bonding, resulting in a biomaterial with high crystallinity index and high tensile strength (4). In case of BC, due to the small fibre diameter of cellulose, the overall material presents high surface area and high porosity (5). BC also possesses a high thermal stability and biocompatibility (6).

Cellulose structures present highly ordered (crystalline) and disordered (amorphous) regions and it possesses four different polymorphs named cellulose I, II, III and IV (1, 7, 8). Cellulose I is found in nature and can be either converted in cellulose II or III (1, 7). Cellulose II can be obtained either through mercerization or through regeneration (dissolution and recrystallization) (1, 7). Cellulose III can be obtained from cellulose I or II through liquid ammonia treatments and then by applying thermal treatment it can convert into cellulose IV (1, 7). Additionally, cellulose I possess two distinct structures: Iα and Iβ, which coexist and their proportion depends on the cellulose source (8, 9). Cellulose Iα is the dominant structure for most algae and bacteria whereas cellulose Iβ is dominant in plants and tunicates (9). The main difference between Iα and Iβ is the stacking of cellulose chains throughout the plane, having a triclinic and a monoclinic crystal system respectively (Figure 1).

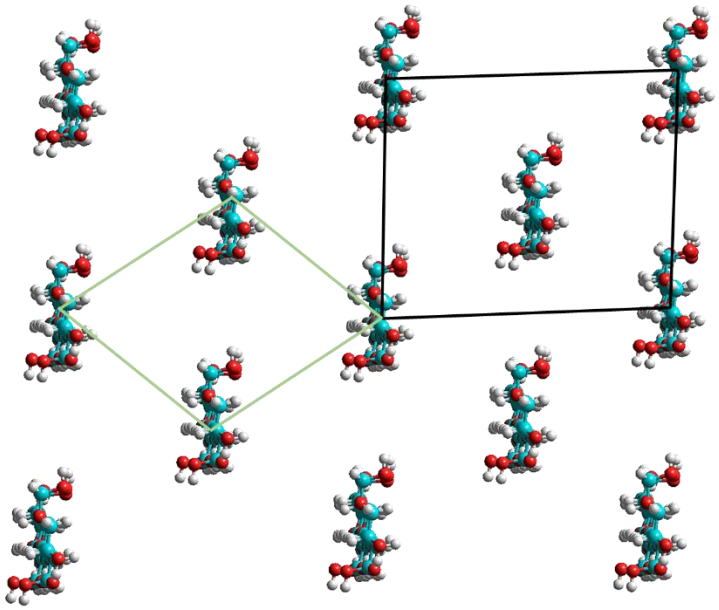

Figure 1 – Schematic representation of cellulose I*α* (-), I*β* (-) crystalline structures (based from (10)).

1.1.1 – Bacterial cellulose

Bacterial cellulose (BC) was first discovered by Adrian J. Brown through the evaluation of the fermentation of "*mother vinegar*", which produced a "*jelly–like translucent mass on the surface of the culture fluid; this growth rapidly increases until the whole surface of the liquid is covered with a gelatinous membrane, which, under very favourable circumstances, may attain a thickness of 25 mm*" (11).

In order for BC biosynthesis to occur, glucose found in culture media is uptaken by glucose permeases found in cell membranes (12). Afterwards it is converted into glucose–6–phosphate by glucokinase in order to trap glucose inside the cell and to facilitate its metabolism (13). Through phosphoglucomutase, the phosphate group is shifted from carbon 6 to carbon 1, that can be converted into UDP–glucose by UDP–glucose phosphorylase (5, 14). In this activated form, glucose is now able to be used by cellulose synthase for BC production (5, 14). Moreover, other sugars can be used as a carbon source for cellulose production, such as fructose, galactose, mannose, among others (15).

Cellulose chains are formed by the polymerization of glucose by cellulose synthase, found in cell membranes (16). These chains are extruded to the culture medium, forming

nanofibrils. The fibrils further aggregate with each other, creating a ribbon–like structure (Figure 2) (17). BC fibrils are about 100 times thinner than plant cellulose, resulting in a highly porous material (5). This biopolymer has a structural role in cellulose–producing bacteria, which confers mechanical, chemical or biological protection within the environment, as well as a functional role by aiding in the competition for substrates (14, 18). Also it protects the bacteria from UV radiation, improves nutrient transport via diffusion and protects the bacteria from heavy metals (18).

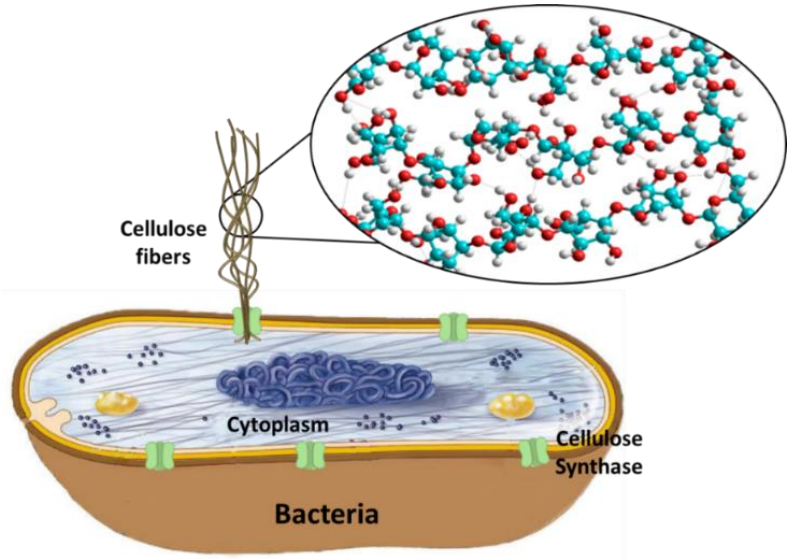

Figure 2 – Schematic representation of BC assembly (based from (19)).

Due to these remarkable properties, BC can be used in different areas, such as food (20) and pharmaceutical industry (17). For instance, in the Philippines, *Nata de coco* is a popular snack which consists in the fermentation of coconut water by *Acetobacter xylinum* (18). In biomedicine, many patents were made involving BC, such as for artificial blood vessels, skin tissue and bone tissue repair, scaffold matrix, antibacterial masks, among others (16). Biofill® is a product of BC used to treat second and third degree burns, as a temporary substitute for human skin (21). There are several advantages regarding the use of this product such as immediate pain relief, close adhesion to the wound bed, reduced infection rate, faster healing and reduced treatment time and costs (21). Sony Corp. marketed loudspeakers and headphones with BC employed, having lower harmonic distortions when compared to conventional paper (22).

Moreover, BC can also incorporate polymerizable monomers into its network, occupying its void volume and interacting with the BC fibre chains (23). Researchers exploit this property in order to change and/or improve the characteristics of BC such as its hydrophobicity, electrical conductivity, surface reactivity, mechanical and thermal resistance, among others (23). In the following section, cellulose modification mechanisms during cellulose regeneration, as well as through *in situ* and *ex situ* chemical polymerization will be presented.

1.2 – Cellulose modification

To improve and give new properties to cellulose sometimes requires chemical modifications. In order to obtain a homogeneous substitution all hydroxyl groups should be available, but in native cellulose such does not happen due to the packing of chains (24). To overcome this problem, cellulose can be dissolved by disrupting the intra– and inter–molecular interaction in cellulose (24).

Cellulose modification can also be achieved through *in situ* polymerization which consists in the polymerization of a monomer in the presence of a filler matrix (BC membrane) (25). This technique allows the filler to preserve its shape as also attain improved dispersion and higher filler–matrix interaction (25).The polymerization can be categorized between *in situ* and *ex situ*, meaning it occurs inside or outside of BC, respectively. Several researchers report the use of *in situ* polymerization, such as Hu et al. (26), Wang et al. (27), Lee et al. (28), Shi et al. (23) and Park (29). In these works, the monomer is incorporated inside of the matrix. This polymerization method allows a uniform dispersion of the monomer into the BC matrix which minimizes the aggregation of polymer–polymer molecules, increasing the interaction between BC and the growing polymer molecules (23, 26-30). The main limitations of this polymerization route are that it is only applicable when the polymerization takes place in liquid phase and that it is difficult to disperse hydrophobic monomers into the BC due to its hydrophilicity (30). In *ex situ* polymerization the dispersion of the monomer inside of BC prior to the polymerization is absent, which can cause a poor bonding between the organic matrix and the polymer (30).

The current work consists in the modification of BC through the polymerization of aniline during the regeneration process as also through *in situ* and *ex situ* polymerization. In the literature, it can be found the importance of the drying method for the properties of the BC membrane in terms of its morphology, crystallinity and swelling ability (31-33). However, it has not yet been studied the effect of using different BC matrixes for the nanocomposites synthesis. Thus, one of the main focus of this work will be the study of the BC matrix onto the synthesis of the BC/PANi nanocomposite.

1.2.1 –Cellulose dissolution

Intermolecular forces, molecular weight, crystallinity and polar groups that may take part in hydrogen bonding, play an important role in the solubility and reactivity of polymers (24). In cellulose, due to the organization of the network makes it insoluble in water and many other solvents (34). The key to successfully dissolve cellulose lies in the ability to disrupt the hydrogen bonds, isolating the chains from each other (35). This is possible if the solvent system used overcomes the intermolecular forces established between cellulose chains, eliminating the cellulose supramolecular structure (35). This treatment gives a simple pathway to transform cellulose into other forms such as fibers, membranes, beads, hydrogels, etc. (36, 37). The development of new solvent systems to create regenerated cellulose is fuelled by the increasing interest in novel techniques suitable for shaping homogeneous chemical modifications.

The first process of cellulose dissolution was discovered by Christian Schönbein, in 1846 (38). It was discovered by accident when the researcher spilled a mixture of nitric and sulfuric acids and cleaned with a cotton apron where afterwards placed near fire to dry, where it ignited almost instantly (39). This happened due to the nitration of OH groups of cellulose (substituted by NO_2 from nitric acid) creating cellulose nitrate (39). It is highly flammable and when heated it releases as much as three times more energy than gunpowder and produces far less smoke, being later on used in explosives (39). What made this material interesting is the fact that it can be dissolved, unlike native cellulose (38). The first studies regarding cellulose dissolution were made with plant cellulose, being later on also applied onto BC (34, 40, 41).

Cellulose solvent systems can be categorized into non–derivatizing and derivatizing solvents (38). Non–derivatizing solvents implies that the solvent does not establishes covalent bonds with cellulose, only directly dissolving the polymer (24, 42). On the other hand, derivatizing solvents react with cellulose, changing its moiety in such a way that it breaks the hydrogen bonds (24, 42).

One main problem regarding the dissolution of cellulose is the use of hazardous, corrosive or non–degradable solvents which hinders the dissolution process to be used in a larger scale. Also, the dissolution procedure is time consuming, being one of the reasons not to be used outside laboratory scale conditions. Quite a few liquids are able to swell cellulose but not able to dissolve it (24). Despite the difficulties regarding cellulose dissolution, there is a handful of solvent systems that can successfully do it. The most known solvent systems are dimethylacetamide/LiCl (DMAc/LiCl), NaOH/urea/water, N–methylmorpholine oxide (NMMO) and ionic liquids (40, 41, 43-46). In the current work, it will be used DMAc/LiCl for BC dissolution.

DMAc/LiCl is the most frequently used solvent systems to dissolve plant cellulose. It was first patented by McCormic in the 1981 (44), being highly efficient in dissolving high molecular weight cellulose with negligible chain degradation (24, 47). This solvent system seems to be very specific when it comes to the interaction with cellulose (24). In other words, neither DMAc with other lithium salts nor DMAc with other chloride salts seem to work in the same way as DMAc/LiCl (24). The dissolution mechanism proposed by McCormic (44) consists on the hydroxyl groups of cellulose interaction with Cl^- via hydrogen bonding while Li^+ is solvated by DMAc (Figure 3). For this interaction to take place, no water can be present.

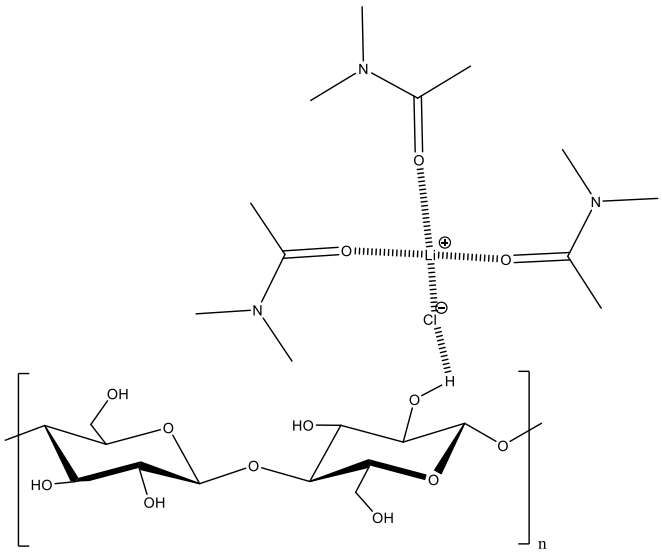

Figure 3 – Schematic representation of the interactions established between cellulose and DMAc/LiCl (based from (48)).

This solvent system is colourless and enables the investigation of dissolved cellulose by ^{13}C–NMR, size exclusion chromatography and light scattering techniques (38). Also, many reports were made regarding the electrospinning of cellulose using this solvent system (49-53). According to Li et al. (49) and Frenot et al. (50), there are some difficulties due to the concentration of cellulose and ions present in the solvent. Using low concentrations of cellulose it may occur electrospraying, forming particles instead of fibers (49). On the other hand, using high concentrations of cellulose it may obstruct the electrospinning due to the viscosity of the solution (49).

1.2.2 – Intrinsically Conductive Polymers

In 1977, the discovery of conductive polyacetylene was the starting point for researchers to find a new whole class of conductive materials: conjugated polymers (54). It led to the discovery of polyaniline (PANi), polypyrrole, polythiophene, among others (55). In 2000, a group of scientists who had discovered and studied conductive polyacetylene were awarded the Nobel Prize in Chemistry (56). Nowadays, the unique properties of these polymers makes them suitable for applications such as thin film transistors, supercapacitors, engineering scaffolds, implantable biosensors and implantable neural prosthetic devices (23,

57, 58). In the current work PANi will be used for the synthesis of BC conductive nanocomposites.

Intrinsically conductive polymers (ICP) possess a conjugated π–electron backbone (Figure 4) which exhibits unusual electronic properties such as low ionization potentials and high electron affinities (59). In the case of PANi, an amine group is found between the aromatic rings (Figure 4A) which should not present a polyconjugation system and therefore no conductivity. In order to assure polyconjugation, the lone pair of electrons from nitrogen participates in the π–electron backbone, giving the conductive properties (57). The electrical conductivity is possible when the electrons are able to move from one end of the polymer to another (55, 60). This property is closely related to the HOMO and LUMO orbitals, as depicted in Figure 4B. The lower the energy gap between these two orbitals, the easier it is for the electrons to flow through the material, conferring conductive properties (55). Although, polyconjugation alone is not possible to turn the polymer conductive. The oxidation of the material is required, creating "holes" in the HOMO orbitals, where an electron is missing. Neighbouring electrons can fill that position but they will create a new hole, and by repeating the process, it allows the charge to migrate long distances (61). The oxidation is possible by adding an acid to the reaction media (chemical oxidation), where the N radical is compensated by the counter ion of the acid (X^-). In the current work, the counter ion will be chlorine since the reaction will be in the presence of HCl. ICP are commonly obtained through either electro– or oxidative–polymerization (62).

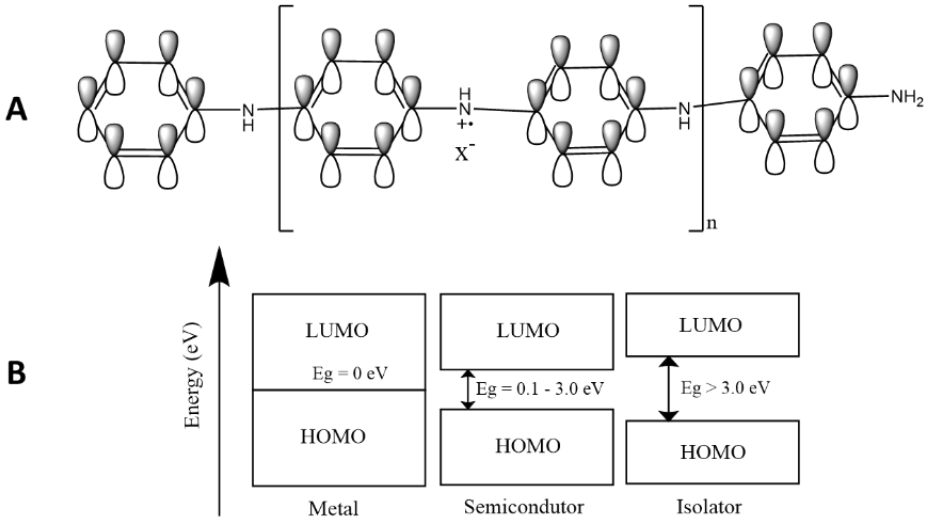

Figure 4 – Schematic representation of doped PANi π–system (A) and diagram demonstrating the energy gap (Eg) between metal, semiconductor and isolators (B) (based from (55)). X^- – anion that interacts with the positively charged groups of PANi.

Chemical oxidation occurs through the formation of covalent bonds between the monomer molecules at the expense of losing two protons with the aid of an oxidizing agent (57). Unlike radical oxidation, it requires large amounts of oxidizing agents since it is spent in every step of the chain–growth polymerization (57). In order for the polymerization process to occur, an oxidation potential of at least +1.05 V is required (57, 63). As such, persulfates are one of the most used oxidizing agents, which have an oxidation potential of +2.01 V (57). The properties of ICP synthesized via chemical oxidation are influenced by the reaction conditions, namely the chemical nature of the oxidants protonating acid, the concentration of the reactants (especially their molar stoichiometry), reaction temperature, templates added to the reaction mixture, among others (64).

PANi is one of the most used ICP due to its low–cost, stability in aggressive chemical environments, non–toxicity and low manufacturing cost (57, 64). The polymer depicts a "head–to–tail" configuration (Figure 5), which consists in *para*–substituted aniline monomer units coupled with each other (57, 65). The monomer aniline consists in a phenyl group attached to an amine group (Figure 5).

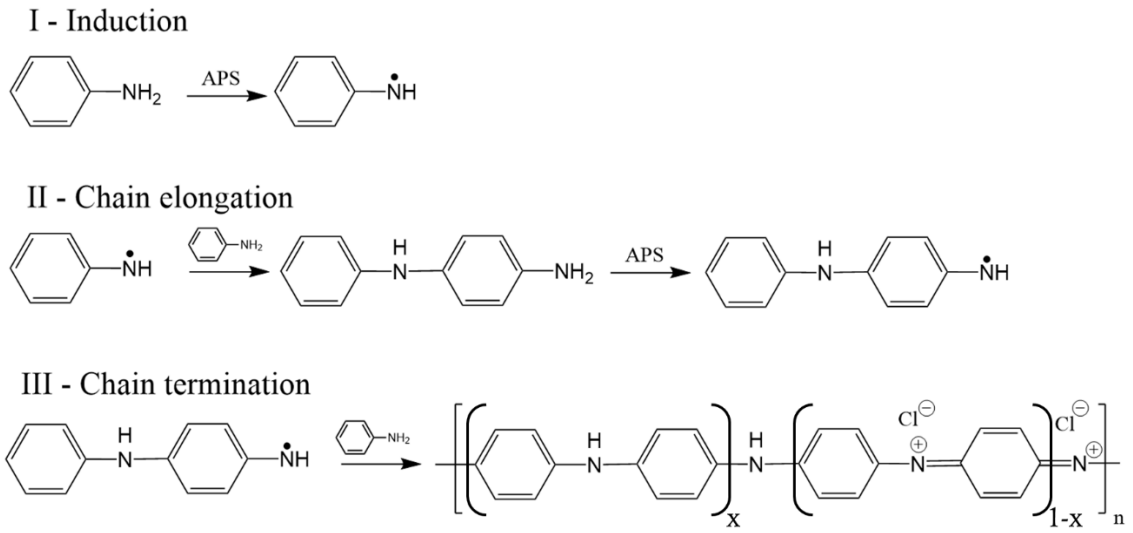

Figure 5 – Reaction mechanism representation of aniline polymerization through chemical oxidation (based from (57)). APS – ammonium persulfate. Polyaniline has three forms: leucoemeraldine (if x equals to 0), emeraldine (if x equals to 0.5) and pernigraniline (if x equals to 1).

Aniline (ANi) is easily oxidized due to its pronounced electron donor ability (57). Depending on the reaction conditions, it is possible to obtain PANi with different oxidation states. This polymer has three forms: a fully reduced (leucoemeraldine), half oxidized (emeraldine) and fully oxidized (pernigraniline), as seen in Figure 5. The reaction mechanism (Figure 5) encompasses three steps: the induction period followed by the chain propagation period and then the chain termination (57). In the induction period, the amine group in aniline is oxidized, generating a radical which reacts with another aniline molecule, resulting in a dimer. By further oxidizing the amine ends, the chain grows until either one of the reactants is depleted.

Several papers have reported BC/PANi nanocomposites, through different polymerization methods, obtaining a wide range of conductivity values, ranging between $1.61x10^{-4}$ and 5.1 S/cm (23, 26-29, 66-68). These conductivity values falls into the category of semiconductive range (10^{-7} and 10^{0} S/cm) (58).

1.3 –Inverse Gas Chromatography

The synthesis of new nanocomposites is of great importance, where it is explored new behaviours and functionalities beyond the starting materials (69). An array of advancements into functionalizing BC are presented in the literature, with the intent to create new BC nanocomposites (1, 70). These new materials need to be extensively characterized in order to give an insight in the properties obtained so that it can be designated into a potential application (69).

With the incorporation of PANi into the BC matrix, it is expected several changes to the starting material due to the changes in the established intermolecular forces. Thus, inverse gas chromatography (IGC) will be used, which will give us valuable information regarding changes in the surface moiety, pore availability and surface energy sites. Due to the relevance of this technique in the current work, the theoretical background will be further discussed.

IGC has been applied in the last years as a reliable source of physicochemical data for many non–volatile materials (71). It consists in the injection of probe molecules (specific molecules with known properties), under controlled experimental conditions, in order to obtain certain properties of the material (72). The term "inverse" is applied since, unlike conventional gas chromatography (GC), the material of interest is placed in a chromatographic column, acting as a stationary phase (73).

Applying this technique offers some advantages, such as its sensitivity and reproducibility, it requires low amount of material, can be run at a wide range of temperatures and it does not require pure solutes (72, 74). Additionally, unlike contact angle technique, in IGC the material does not require a previous treatment on the surface (75). For instance, in order to study powders via contact angle technique its necessary its compression, which results in surface morphology modifications (76).

This technique can be applied into a wide range of materials, from organic (such as polymers and pharmaceuticals) (77) to inorganic (such as silica and other minerals) (78).

1.3.1 – IGC instrumentation

In sum, IGC consists in a mass flow controller; two ovens: one for the solute reservoir and one for the column with the packed sample; a detector and a computer (Figure 6). Helium is used as the carrier gas since it is inert, avoiding interactions with the column and the adsorbate. Adsorbate–adsorbate interactions are neglected when tests are conducted at infinite dilution, where the amount of probe injected is near the limit of detection of the detector (79). At infinite dilution, the probe molecules only interact with the most energetic active sites, following the Henry Law's region (79). In that region, one should expect a symmetrical Gaussian peak and therefore a linear isotherm (80).

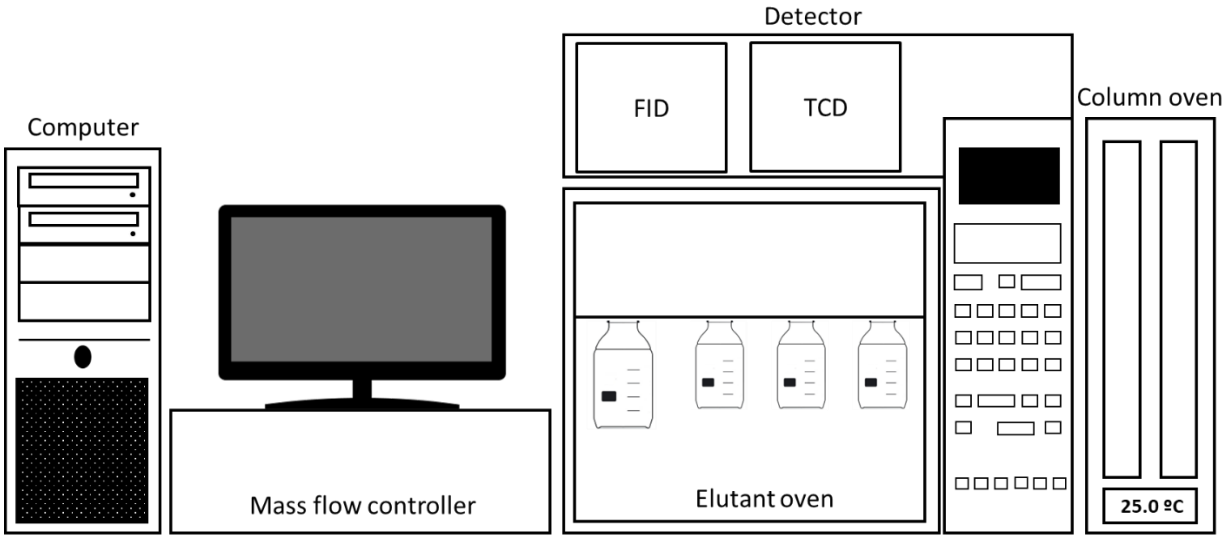

Figure 6 – Schematic representation of the inverse gas chromatographer apparatus.

IGC is equipped with two detectors: flame ionization detector (FID) and thermal conductivity detector (TCD). Compared to TCD, FID is better suited under infinite dilution tests since it has a higher sensitivity, up to 10^{-9} mol (81). Both detectors can detect organic molecules while FID, unlike TCD, cannot detect water (81).

In chromatography, retention time (t_R) is commonly used in order to characterize each peak, although it changes considerably according to the experimental conditions (namely carrier gas flow rate and the pressure drop in the column). The latter parameter is of great importance since in chromatography the volume of the gas changes when it crosses the column, due to its compressibility property (82). The James–Martin compressibility factor (j)

takes in account the inlet and outlet pressure of the carrier gas in the column, correcting the pressure variations along the run (82).

Retention volume (V_N) considers the aforementioned parameters, offering more reliable and reproducible results (83). Adapting to IGC, V_N can be defined as the volume of the mobile phase that left the column during the time the adsorbate was interacting with the analyte. This way, V_N can be used as a reference parameter since it is affected by the interactions between the adsorbate and the sample (83). Further parameters can be taken into consideration, such as the temperature and the sample mass (77). This way, the values of V_N are normalized, being now called specific retention volume (V_g), providing comparable results (84). It can be deducted from the following equation (1):

$$V_g = \frac{F.j}{m}.(t_R - t_0).\frac{273.15}{T} \quad (1)$$

where F is the carrier gas flow; m the sample mass; t_R and t_0 the retention time of the adsorbate and the inert reference gas respectively and T the absolute temperature.

1.3.2 – Surface energy

1.3.2.*1* – Dispersive component

The surface of a solid is composed of free bonding functional groups, establishing an interface with the surrounding environment. An important surface parameter is its free energy, being defined as the energetic difference between the surface and the bulk per unit area of surface. According to Fowkes, surface energy interactions can be split in dispersive forces (Van der Waals interactions) and specific forces, such as acid–base, hydrogen bond and metallic interactions (85). From the injection of a series of *n*–alkanes, Schultz et al. determined the dispersive component, by applying the following equation (2) (86):

$$\Delta G^D = RT\ln(V_g) = 2N_A.(\gamma_S^D)^{\frac{1}{2}}.a_m(\gamma_L^D)^{\frac{1}{2}} + K \quad (2)$$

where ΔG^D is the Gibbs free energy of adsorption of the dispersive component; R the perfect gas constant; N_A Avogadro's constant; a_m the cross–sectioned area of the adsorbate; γ_S^D the dispersive component of the material's surface energy; γ_L^D the probe surface tension and K a constant.

From the previous equation, one should obtain a linear trend in the data, usually designated as the alkane line, being the slope equal to $2N_A.\sqrt{\gamma_S^D}$. Basically, a probe with a certain $a_m\sqrt{\gamma_L^D}$ will have a given ΔG^D which corresponds to the vertical distance between the x axis and the data plotted (72).

1.3.2.2 – Specific component

In the case of polar molecules, the free energy of absorption is above the alkane line, since both dispersive and specific interactions take place between the surface and the adsorbate. The latter interaction corresponds to the vertical distance between the polar adsorbate and the alkane line (72). From the specific free energy of adsorption it is possible to obtain the surface donor (γ_S^-) and acceptor (γ_S^+) numbers, based on the Good–Van Oss concept (87). Experimentally, one should use two probe monopolar molecules: one acid and one basic. This way, it is possible to obtain the parameters indicated above (88) from the following equation (3):

$$\Delta G^{SP} = 2N_A a_m \left(\sqrt{\gamma_S^- \gamma_L^+} + \sqrt{\gamma_S^+ \gamma_L^-}\right) \quad (3)$$

where γ_L^+ and γ_L^- are the acceptor and donor numbers of the adsorbate and ΔG^{SP} the Gibbs specific free energy of adsorption.

After obtaining the donor and acceptor numbers of the surface, it is possible to estimate the specific free energy of adsorption from the following equation, which corresponds to the geometric mean of the aforementioned parameters (4):

$$\gamma_S^{SP} = 2\sqrt{\gamma_S^- \gamma_S^+} \quad (4)$$

Now with both specific and specific surface energy, it is obtained the total surface energy (γ_S^{Total}), corresponding to the sum of the two components.

1.3.3 – Acid-base character through Gutmann Method

Regarding the specific component of the surface, a different approach was taken by Gutmann (89). Similar to the Good–Van Oss method previously described, the adsorbates also have reference values, which are obtained experimentally. For the basic component, the donor number (DN) is defined as the enthalpy of interaction between the molecule being studied and $SbCl_5$ (used as a reference Lewis acid) in 1,2–dichloroethane, a neutral solvent (79). On the other hand, for the acid component, the acceptor number (AN) was determined by correlating the induced chemical shifts in ^{31}P NMR spectra of triethylphosphine oxide (used as a reference Lewis base) dissolved in the acid molecule being studied. Riddle & Fowkes issued that these chemical shifts can be influenced by Van der Waals interactions, improving the method by developing modified acceptor numbers (AN*) (90). By doing so, the donor and acceptor numbers can be compared and related to surface acidity and basicity from the following equation (5):

$$\frac{\Delta G^{SP}}{AN*} = \frac{DN}{AN*} K_a + K_b \quad (5)$$

being K_a and K_b acid and basic interaction constants that characterize the polarity of the surface. By plotting the results with the previous equation, the slope should correspond to K_a while K_b to the intercept with the Y axis.

1.3.4 – Surface nanomorphology

Surface nanomorphology gives us an insight about the deviation from a flat surface of a given sample due to the surface asperities, which is correlated to the retention time. Brendle

and Papirer have shown that a given isomer exhibited a lower retention time when compared to the corresponding linear alkane probe (91). In fact, the retention time can be either shorter due to the steric hindrance of the branched alkane probes to access the surface pores or longer if the probes can be inserted in the pores (91). The size exclusion effect is related not only from the surface morphology but also due to the molecular shape (92). In this study, *n*–octane isomers such as 2,5–dimethylhexane, 2,2,4–trimethylpentane and cyclooctane were used. The nanomorphology index is determined by the following equation (6):

$$\text{Morphology index} = e^{\frac{-\Delta G_a^M}{RT}} \quad (6)$$

where ΔG_a^M corresponds to the distance between the probe and the alkane line. If the morphology index is lower than 1 it indicates that the probe had steric hindrance with the surface of the material whereas values higher than 1 indicate the probe insertion into the pores. Thus, the closer the morphology index is to 1 it means that the given isomer behaves like the corresponding linear alkane, where it is considered that the surface is flat (92).

1.3.5 –Surface area

Surface area (S_{BET}) of materials are commonly obtained from the Nitrogen adsorption isotherm at 77K, using the Brunauer–Emmett–Teller (BET) equation (93). This method is based on the relationship between the amounts of gas adsorbed at different gas pressures, at a fixed temperature T. After a certain amount of gas pressure, the amount of gas adsorbed reaches a plateau, physically corresponding to the monolayer capacity (nm). IGC can evaluate these parameters, therefore being possible to determine the surface area. The original equation applied by Brunauer et al. is linearized (7), which is possible to obtain the monolayer capacity from the slope and the intercept.

$$\frac{p}{n(p_0 - p)} = \frac{c - 1}{n_m c}\frac{p}{p_0} + \frac{1}{n_m c} \quad (7)$$

being p_0 the gas pressure, p the adsorbate pressure, n_m the monolayer capacity, n the amount of probe adsorbed and c a constant.

If the area of the probe used in the BET measurements is known, it's possible to obtain the BET surface area (S_{BET}) by the following equation (8):

$$S_{BET} = an_mN_A \quad (8)$$

1.3.6 – Surface Heterogeneity

Using the sorption isotherm results it's possible to calculate the adsorption potential distribution, which will correspond to the energy profile of the surface (94). Firstly, to obtain the distribution function, partial pressures are converted into the adsorption potential (A) from the following equation (9):

$$A = RTln\left(\frac{p}{p_0}\right) \quad (9)$$

Then, the distribution parameter (Φ) is determined, corresponding to the 1st derivative of the adsorbed amount with the adsorption potential, which will give us the energy profile plot.

1.3.7 – Diffusion analysis

In diffusion analysis, different flow rates of mobile gas are used. The principle behind this procedure is that as the probe progresses from the inlet to the outlet, it spreads due to diffusion phenomena (80). The diffusion coefficient can be obtained from the width of the elution peak through the equation developed by van Deemter et al. as shown in equation (10).

$$H = A + \frac{B}{u} + Cu \quad (10)$$

where H is the height equivalent to the theoretical plate (cm) and u is the carrier gas speed (cm/s). The parameters A, B and C are independent of the velocity of carrier gas, related to the column, gases and operating conditions respectively (80, 95). The parameter A is called eddy diffusion and is related to the size of support particles and irregularity of packing (96). The parameter B describes the longitudinal diffusion of the probe along the stream of carrier gas (96). The third parameter (C) is related to peak broadening which is due to the mass resistance within the column (96). Through the constant C it is obtained the diffusion coefficient (Dp) through the following equation (11):

$$C = \frac{8}{\pi}\frac{K}{(1+K)^2}\frac{d^2}{Dp} \quad (11)$$

where K is the partition ratio and d the film thickness.

1.3.8 – Work of adhesion

When different solids contact each other, adhesion forces may occur. The intensity of the adhesion forces is intimately related to the surface energies of the materials one and two (97). Work of adhesion (W_{adh}) is a measure of the strength between two solid surfaces, being defined as the free energy required to separate reversibly a unit area of two phases in contact (98). This means that a higher W_{adh} value should reflect a stronger interaction between two materials. On the other hand, work of cohesion (W_{coh}) is related to the interactions that a solid establishes with itself. In the current work the determination of both W_{adh} and W_{coh} will be used to estimate the interactions between the membranes and the drug sodium sulfacetamide. The W_{adh} will represent the membrane-drug interactions while the W_{coh} corresponds to the interactions inside the membrane. The former parameter can be calculated by the following equation (12):

$$W_{adh} = 2\sqrt{\gamma^{D}_{S,1}.\gamma^{D}_{S,2}} + 2\sqrt{\gamma^{+}_{S,1}.\gamma^{-}_{S,2}} + 2\sqrt{\gamma^{-}_{S,1}.\gamma^{+}_{S,2}} \quad (12)$$

In the same way, W_{coh} can be calculated by the following equation (13):

$$W_{coh} = 2\sqrt{\gamma_{S,1}^{D}.\gamma_{S,1}^{D}} + 2\sqrt{\gamma_{S,1}^{+}.\gamma_{S,1}^{-}} + 2\sqrt{\gamma_{S,1}^{-}.\gamma_{S,1}^{+}} \quad (13)$$

Strzemiecka et al. (99) evaluated the dispersion of different carbon blacks on polyurethane, stating that not only the adhesion forces play an important role in the degree of dispersion but also the cohesion forces between the filler particles. Thus, it was presented the W_{adh}/W_{coh} ratio, stating that it can be used as an indicator of the degree of the dispersion of the filler particles into the matrix.

Aim of the study

The focus of the current work was the use of different BC modifications for the synthesis of a conductive BC/PANi nanocomposite with potential for drug delivery through electrical stimulus. In this regard, different BC matrixes were used (drained, freeze dried and regenerated), as well as different aniline polymerization methods (*in situ* and *ex situ*), obtaining different BC/PANi nanocomposites.

Initially the different BC matrixes were evaluated, regarding the drying method (oven dried and freeze dried), as well as the regeneration treatments applied. Then, the different BC modifications were assessed to evaluate the physico-chemical changes occurred with PANi incorporation onto BC. Thus, both matrixes and nanocomposites were assessed regarding their structural, morphological and surface characteristics through Fourier transformed infrared coupled with attenuated total reflectance (FITR–ATR), scanning electronic microscopy coupled with energy dispersive x-ray spectroscopy (SEM-EDX), ultraviolet-visible (UV–Vis), X-ray diffraction (XRD), thermogravimetrical analysis (TGA), atomic force microscopy (AFM), Swelling, Contact angle measurement and IGC.

Then, the different nanocomposites were tested in terms of drug loading capacity and antimicrobial activity studies on *Escherichia coli* (*E. coli)* using sodium sulfacetamide as the reference drug.

Chapter II – Materials and methods

The BC matrixes and the nanocomposites synthesized in this work were subjected to a series of analyses to fully characterize the materials, obtaining an insight of the changes occurred during the drying and regeneration treatments, as well as due to the incorporation of PANi onto BC.

2.1 – BC production

Gluconacetobacter sp. was statically cultivated in Hestrin and Schramm (HS) medium (previously autoclaved during 15 min at 121 ºC) in order to meet the bacteria cellular requirements for cellulose production. The composition of the HS medium can be found elsewhere (100). After being incubated for 7 days at 30 ºC, the membrane was removed and washed with NaOH 0.5 M, at 80 ºC during 2 h, and then neutralized with distilled water. The membrane was stored at 5 ºC until further use.

The BC membranes were oven dried (OD–BC) and freeze dried (FD–BC) in order to evaluate the drying effect and later on the influence of the matrix in the polymerization of aniline. Then, OD–BC was used to obtain regenerated BC (R–BC).

2.2 – BC dissolution optimization

Prior to dissolution, OD–BC was placed on an Erlenmeyer. DMAc was added to obtain a BC concentration of 0.5% (w/v). Likewise, LiCl was added to obtain a percentage of 8% (w/v). These proportions were based on the work published by Li et al. (49). Different parameters were considered for the optimization of the dissolution procedure, which are found in Table 1 in the same order as they were applied. Swollen samples were left static overnight at room temperature. Heat–treated samples were placed in an oil bath at 110 ºC during 1 h. An ultrasonic bath Ultrasons–H (Selecta) was applied during 1 h at room temperature for the ultrasound–assisted solutions.

Table 1 – Dissolution parameters tested on BC dissolution.

Cut	Swelling in DMAc	Swelling in DMAc/LiCl	Heat	Ultrasounds	Stirring overnight	Observation
			x		x	Swelling
x			x		x	Swelling
x	x		x		x	Swelling, loss of white colour
x	x		x	x	x	Dissolution
x		x	x	x	x	Dissolution

In order to confirm that BC was fully dissolved, a drop of sample was observed in an Olympus BX 41 optical microscope coupled with a Moticam 10 camera using the software Motic Image Plus 2.0.

The regeneration process was employed by adding water gently in the dissolved BC solution, leaving under slow stirring (< 100 rpm) during 1 h, so that the R-BC gains some firmness. Afterwards the samples were washed through dialysis during 72 h using a dialysis tubing (benzoylated) with a molecular weight cut–off of 2000 Da (Sigma Aldrich). In the end, the samples were oven dried at 40 ºC. Based on the optimization results, the dissolution of BC by adding both DMAc and LiCl at the same time was used for future tests.

2.3 – BC nanocomposites synthesis

For all the studies conducted, the BC nanocomposites were obtained through chemical oxidative polymerization with 3x3 cm BC membranes and solution reactions (aniline monomer and ammonium persulfate (APS)), both dissolved in HCl, and purged with N_2 during 30 min prior to polymerization. Afterwards, the reaction mixture was kept under low stirring (<100 rpm) at room temperature. After 24 h of polymerization, the membranes were washed thoroughly with distilled water until no aggregates of polymer were in solution. The nanocomposites were then oven dried overnight at 40 ºC and weight out to determine the PANi content. The ratios applied in this work are based on the optimization of the nanocomposites conductivity obtained by Wang et al. (27) with a BC:ANi mass ratio of 0.10 and molar ratio of Ani:HCl:APS of 1:1.2:1.

For ANi polymerization, three approaches were employed, including *in situ* and *ex situ* polymerization, as well as a novel method that polymerizes aniline during BC regeneration. The samples were named according to the type of BC matrix (drained – no prefix, freeze dried – FD, regenerated – R) and polymerization method (*in situ* – IS, *ex situ* – ES). The determination of the polymer content in the membranes was determined through the following equation:

$$\text{Polymer content} = \frac{w_{composite} - w_{BC}}{w_{composite}} \times 100 \quad (14)$$

where $w_{composite}$ corresponds to the dried weight of the nanocomposite and w_{BC} corresponds to the dry weight of BC used for the nanocomposite synthesis.

2.3.1 – Synthesis of the nanocomposites through *in situ* and *ex situ* polymerization

The BC membranes used in this work were either drained through manual pressure or freeze dried. *In situ* polymerization is employed by letting stand during 1 h the monomer solution in contact with the membranes prior to addition of the oxidizing agent in order to incorporate the monomer inside the BC network (Figure 7). For *ex situ* polymerization, the incorporation step was absent and the ANi and APS solutions were added simultaneously (Figure 7). Since the polymerization reaction occurs within the first minutes, the amount of monomer incorporated prior to complete polymerization is insignificant.

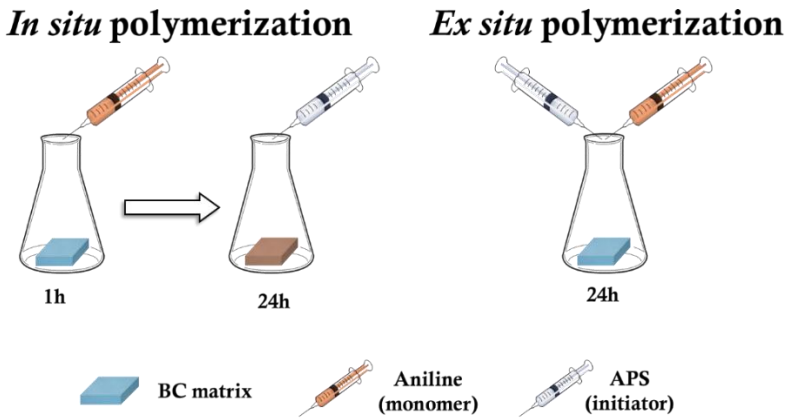

Figure 7 – Schematic representation of the methodology employed for *in situ* and *ex situ* PANi polymerization.

2.3.2 – Synthesis of the nanocomposites during the regeneration of BC

The dissolution process employed was the same as previously described, which consisted in swelling cut cellulose (0.5% w/v) into DMAc and LiCl (8% w/v) overnight, followed by heating at 110 °C and ultrasound treatment during 1 h each. Afterwards, it was added ANi, leaving under agitation during 4 h (Figure 8). Then it was added a solution of HCl and APS, leaving the reaction under low stirring (< 100 rpm) during 24 h. The proportions of ANi, HCl and APS were the same as the other nanocomposites synthesized (previous subsection). Then, the regenerated BC/PANi nanocomposite was washed with water to remove the excess polymer and then washed under dialysis during 72 h to remove the remnants of solvent used for BC dissolution.

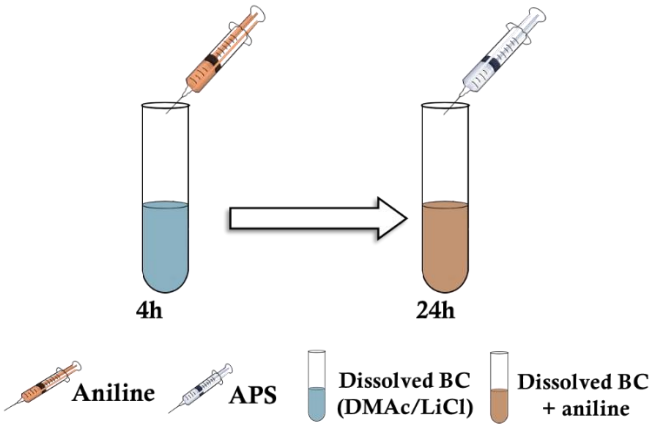

Figure 8 - Schematic representation of the methodology employed for the *in situ* aniline polymerization during BC regeneration.

2.4 – Drug loading capacity

The preparation of the drug–loaded samples was based on Trovatti et al. (99) and Almeida et al. (100) works, where membranes of 1x1 cm were soaked in 5 ml of 10% sodium sulfacetamide at room temperature during 24 h. Afterwards, the membranes were rinsed gently in distilled water during 5 min to remove the excess drug on the surface and then oven dried during 24 h at 40 ºC. Then, the drug content in the membranes were determined according to the following equation (14):

$$Drug\ content = \frac{w_L - w_U}{w_L} \times 100 \quad (14)$$

where w_U and w_L are the weight prior (unloaded) and after (loaded) drug incorporation.

2.5 – Antimicrobial Activity

The antibacterial activity of the drug loaded membranes was assessed through the optical density method. This experiment was based on the published work by Figueiredo et al. (101) and Ul–Islam et al. (102). First, a fresh culture of *E. coli* (DH5 α strain) in Luria-Bertani (LB) growth media was incubated in a shaking incubator at 37 ºC and 125 rpm during 24 h, which presented an absorbance of 0.645, corresponding to 6.78 x 10^7 cells/ml.

Then, in test tubes, 13.5 ml of LB growth media were added. In the same test tubes, 1.5 ml of fresh culture of *E. coli* was added, followed by the addition of the membrane. The absorbance was monitored at 0, 1, 2, 4, 6, 8, 10, 12, 24 and 48 h after exposure to the membranes (2x2 cm) by collecting 1 ml aliquots and measuring in a Genesys 10S spectrophotometer (Thermoscientific). The control of this experiment consisted in evaluating the bacterial growth in the absence of any membrane. The reference wavelength used was of 600 nm, which is the most common wavelength used for *E. coli* growth monitorization, corresponding to the turbidimetry caused by the cell suspension (103). The control and samples were run in duplicates.

The experimental set-up for the antimicrobial activity test through electrical stimulus is depicted in Figure 9, which consists in the immersion of the conductive membrane (3x1.5 cm) under the growth culture while applying a continuous potential difference of 5 V between the electrodes. The absorbance was monitored at 0, 1, 2, 4, 6, 8, 10, 12, 24 and 48 h after exposure to the membrane, by collecting 1 mL aliquots.

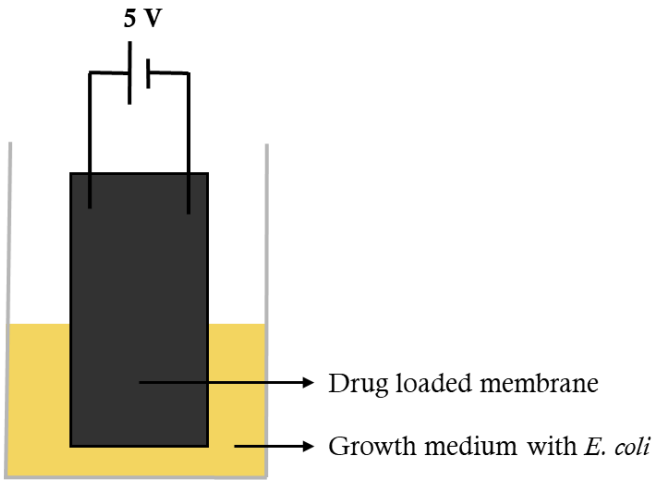

Figure 9 – Schematic representation of the experimental set-up for the drug release through electrical stimulus.

2.6 – Statistical analysis

The statistical analysis of the data was carried using the IBM SPSS Statistics 23 software. Differences in the measurements of a given parameter were assessed by one–way analysis of variance (ANOVA), followed by a Tukey's post hoc analysis. For IGC, the error of the measurements was of 3% and as such the upper and lower values from the experimental value were determined. p-values of <0.05 were considered statistically different.

2.7 – Characterization methods

2.7.1 – Attenuated total reflectance Fourier transformed infrared spectroscopy

FTIR–ATR spectra of the samples were obtained with a Perkin Elmer Spectrum Two coupled with a Diamond ATR accessory (DurasamplIR II, Smiths Detection, UK). 32 scans were acquired in the range of 4000–650 cm^{-1}, with a wavenumber resolution of 1 cm^{-1}.

2.7.2 – X–ray diffraction

The X–ray diffraction (XRD) measurements were carried out with a Phillips X'pert MPD diffractometer using Cu Kα radiation (λ of 1.54 Å) operating at 45 kV and 40 mA. The 2θ range under analysis was of 5–60º. The crystallinity index (CI) of the samples was determined through Segal et al. method (104) according to the following equation 14:

$$CI = \left(1 - \frac{I_{am}}{I_{110}}\right) \times 100 \quad (15)$$

where I_{am} corresponds to the intensities of the amorphous region (18.0º and 13.8º for type I and type II cellulose respectively) and I_{110} correspond to the intensity at the (110) plane (22.7º and 21.0º for type I and type II cellulose respectively). To determine the Z value for each sample, to know if the sample was rich in either cellulose I_α or I_β, the XRD profile were deconvoluted using PeakFit 4.12 software and then it was determined the *d*–spacing (*d*) at both (100) and (010) angles (around 14º and 16º respectively), by applying Bragg's equation (16):

$$d = \frac{n\lambda}{2\,sin\,\theta} \quad (16)$$

where *n* corresponds to the order of reflection (n=1) (105). After obtaining the *d*–spacing for both angles, the Z value was obtained through the following equation (17):

$$Z = 1693d_1 - 902d_2 - 549 \quad (17)$$

if Z>0 represents rich cellulose Iα samples, whereas Z<0 represents samples rich in cellulose Iβ (106).

2.7.3 – Thermogravimetrical analysis

The thermal stability of the BC matrixes, as well as the obtained nanocomposites were evaluated using a SETSYS Evolution 1750 thermogravimetric analyser (Setaram) from room temperature (25ºC) until 700 ºC, using a heat ramp of 10 ºC/min under an oxygen flow of 20 mL/min.

2.7.4 – Scanning electronic microscopy coupled with energy dispersive X–ray spectroscopy

The samples were mounted and gold–coated in preparation for the SEM–EDX imaging analysis, performed using a scanning electron microscope SU3500. SEM images were obtained using a magnification of 3000x. The EDX analysis was performed under an accelerated voltage of 5 kV, with the aim to identify the chemical compositions of samples at the surface, determining the weight percentages (wt. %) of elements C, O, N, S and Cl.

2.7.5 – Atomic force microscopy

To evaluate the surface topography of the samples, the AFM analysis was employed by an atomic force microscope (AFM, Solver PRO, NT–MDT, Russia) in tapping mode in air atmosphere. Samples were scanned with the standard Si (silicon) cantilever with a force constant of 22 N/m and at a resonance frequency of 325 kHz (tip radius was 10 nm and the

tip length was 95 μm), using a scan rate of 1.3 Hz. The surface roughness (R_q) was measured from representative images at 5x5 μm^2 area, which corresponds to the average value of the surface height, which can be determined through the following equation (19):

$$R_a = \frac{1}{L}\int_0^L |Z\,(x)|dx \tag{18}$$

where Z(x) is the function that describes the surface profile analysed in terms of height (Z) and position (x) of the sample over the evaluated length (L).

2.7.6 – Electrical conductivity measurement

The nanocomposite conductivity measurements were made at room temperature using the 4–probe technique, as depicted by Figure 10 (107). The system was comprised by a Fluke 87 RMS multimeter (to measure the current), a Leader multimeter 856G (to measure the voltage) and a CV regulated power supply Lab 502. Since the sample thickness (t, μm) is lower than the probe spacing (S, μm), the resistivity (ρ, Ω.cm) was measured according to the following equation (19):

$$\rho = \frac{\pi t}{ln(2)} \times \frac{V}{I} \tag{19}$$

where V is the voltage and I (A) the current intensity. Then, conductivity (σ, S/cm) was obtained through the following equation (20):

$$\sigma = \frac{1}{\rho} \tag{20}$$

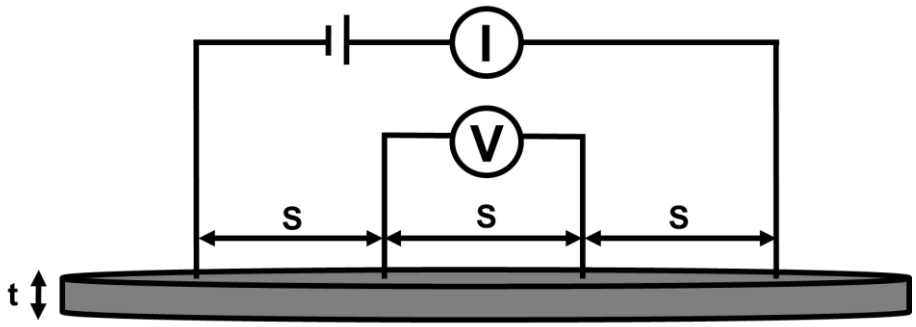

Figure 10 – Schematic representation of the 4–probe resistivity measurement principle (based from *107)*).

2.7.7 – Swelling capacity

Swelling studies were performed according to Figueiredo et al. (101) in order to evaluate the rehydration ability of the nanocomposites. This procedure comprises in the immersion of the membranes in distilled water, at room temperature, monitoring their weight increase during 48 h. Regarding the weight measurement, the samples were removed from the water and their surfaces were carefully wiped with dry filter paper. The swelling ratio (SW) was then determined from the following equation (21):

$$\mathrm{SW}\ (\%) = \frac{W_s - W_d}{W_d} \times 100 \qquad (21)$$

where W_s and W_d are the weight of the swollen and dried membrane respectively.

2.7.8 – Contact angle measurement

A water droplet was aliquoted onto each membrane and the contact angle measurement was recorded with Krüss DSA–100 contact angle analyser, by using on average 10 μL of ultrapure water. The image was processed with the software imageJ using the plug–in *drop_analysis*, using the low–bond axisymmetric drop shape analysis approach (LB–ASDA) developed by Stalder et al. (108).

2.7.9 – Inverse Gas Chromatography

The measurements were carried out on a commercial inverse chromatograph (Surface Measure Systems London, UK), equipped with both FID and TCD detector. The system was automatized with the Software SMS IGC Controller v1.8. Silanized glass columns with 3 mm inner diameter and 300 mm length were used (dimethyldichlorosilane, Repelcote BDH, UK), packing the sample through vertical tapping. The samples were conditioned overnight followed by 2 h at temperature measurement to stabilize.

Dispersive surface energy measurements were carried using a series of *n*–alkanes, from *n*–octane to *n*–undecane. For specific surface energy measurements, tetrahydrofuran, dichloromethane, ethyl acetate, acetonitrile and ethanol were used. For the nanomorphology index, cyclooctane, 2, 5–dimethylhexane and 2, 2, 4–trimethylpentane were used. In all previous analysis, a concentration of 0.2 p/p_0 was employed. The isotherm measurements of *n*–octane was carried at different concentrations, between 0.05 and 0.2 p/p_0. All measurements were carried with a flow rate of 10 mL/min and at 20–35 ºC for BC, 40–55 ºC nanocomposites and at 70–85 ºC for PANi sample. The higher temperatures applied for the nanocomposites and PANi powder is due to the strong interactions of the probes with the samples.

The probes were supplied by Sigma Aldrich, with analytic grade (> 99%). Methane was used as an inert reference gas and Helium was used as the carrier gas, both supplied by Air Liquide Company, with a purity above 99%. The physical constants used in IGC were taken from the literature and are displayed in Table 2 ((109)).

Table 2 – Physical constants of the applied probes in IGC.

Probe	γ_L^D (J/m^2)	a (10^{-19} m^2)	DN (kcal/mol)	AN* (kcal/mol)	γ_L^+ (mJ/m^2)	γ_L^- (mJ/m^2)	χ_t^c
n-undecane	0.0246	8.10	–	–	–	–	11
n-decane	0.0234	7.50	–	–	–	–	10
n-nonane	0.0227	6.90	–	–	–	–	9
n-heptane	0.0213	6.30	–	–	–	–	8
Tetrahydrofuran	0.0225	2.90	20.00	0.50	–	–	–
Dichloromethane	0.0245	2.45	–	3.90	124.58	0	–
Ethanol	0.0211	3.53	19.00	10.30	–	–	–
Ethyl acetate	0.0196	3.30	17.10	1.50	0	457.67	–
Acetronitrile	0.0275	2.14	14.10	4.70	–	–	–
2, 2, 4–trimethylpentane	–	–	–	–	–	–	7.40
2, 5–dimethylhexane	–	–	–	–	–	–	7.68
Cyclooctane	–	–	–	–	–	–	8.32

γ_L^D – Surface tension; a – cross–section area; DN – donor number from Gutmann method; AN* – acceptor number from Gutmann method; γ_L^+ – acceptor number from the Van Oss method γ_L^- – donor number from the Van Oss method; χ_t^c – topological indexes.

Chapter III – Results and discussion

3.1 – Influence of bacterial cellulose drying routes and regeneration on its final properties

The final characteristics of the BC matrixes depend on their microstructure, which, in turn, might be influenced by the processing methods prior to BC modification (110). Thus, in this section, the effect of BC regeneration and the drying method (freeze dried and oven dried) on the final BC matrixes properties (structural, morphological, wetting and surface) was studied. In addition, the optimization of BC regeneration was made.

3.1.1 – BC regeneration

The dissolution of cellulose has been used as an efficient route for cellulose modification (44). In the case of BC, due to the higher degree of polymerization it turns more difficult to accomplish a complete dissolution (46). In the current work, the dissolution of OD-BC was made by using the DMAc/LiCl solvent system, which can be found on the following subsection.

DMAc/LiCl solvent system is known for being time consuming essentially due to the solvent change process (49, 50, 111-113). Thus, to improve the dissolution procedure, parameters were considered and evaluated. These included the BC particle size, contact time with the solvent prior to activation, and activation of the solvent through heat and ultrasonic treatment.

Regarding the particle size, it was seen that large particles would only lead into cellulose swelling and not dissolution, thus BC was cut into small pieces to increase the contact with the solvent. The next attempt was letting BC into contact with DMAc during 24 h and then add LiCl, followed by heating and overnight moderate stirring. This process also led to BC swelling, but with a loss of the characteristic white colour of dried BC. By letting BC in contact with the DMAc, a higher permeation of the solvent was observed, although it was not strong enough to dissolve BC chains. As such, after heat treatment BC

was subjected to ultrasound treatment into the sample where, after 1 hour of continuous ultrasound treatment the BC dispersion into the solution was observed. However, the dissolution was not complete. Thus, to prompt the full solution of BC, it was left under moderate stirring overnight and no suspended particles in solution were observed (Figure 11). Throughout this process, the crucial steps for a successful dissolution of BC are cutting BC into small pieces, leaving under contact with the solvent overnight, as well as the ultrasonic treatment.

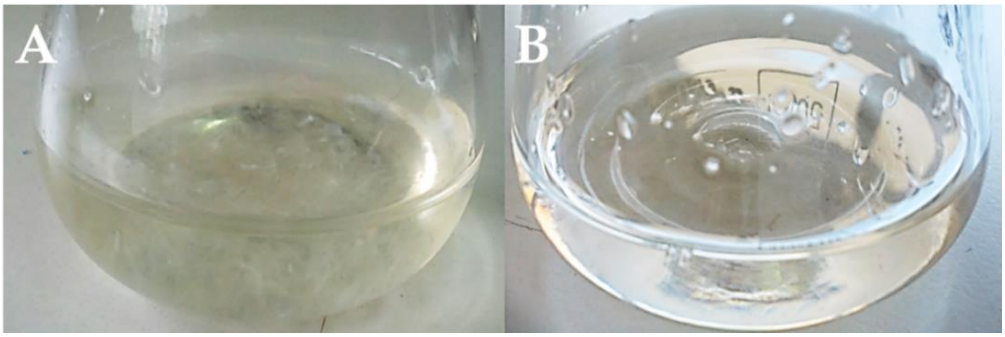

Figure 11 – Dissolution of BC in DMAc/LiCl prior to dissolution (A) and after dissolution(B).

Alternatively, another experiment was made by keeping BC in contact overnight with both the solvent and the salt, where a complete dissolution was also observed (Table 1). To confirm the complete dissolution of BC, a drop of partially dissolved and completely dissolved solutions were observed under the optic microscope (Figure 12). It was only seen traces of undissolved cellulose in the optimized process whereas in the unoptimized process (prior to stirring overnight) significant amounts of undissolved cellulose fibers were found.

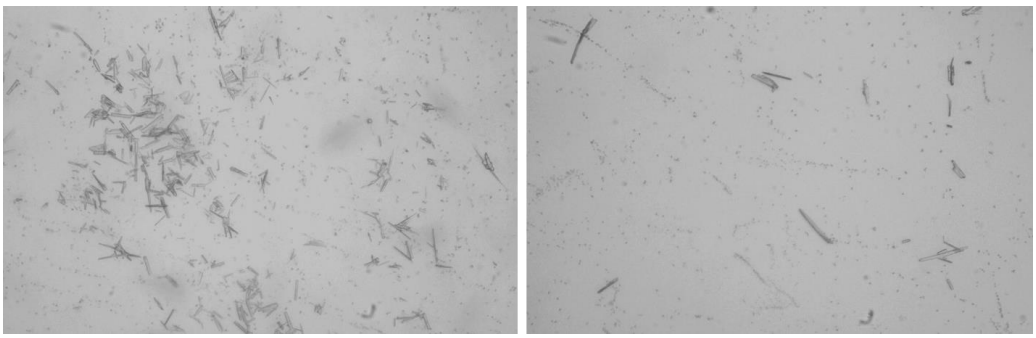

Figure 12 – Photomicrography (100x) of unoptimized BC dissolution (A) and optimized BC dissolution (B) in DMAc/LiCl.

The regeneration process was made by gently adding water into dissolved BC, and left static during one hour to let water permeate R–BC, giving a rigid material. Afterwards, the membranes were washed overnight in distilled water and oven dried. The weight of the sample was higher than the amount of BC added, which indicates that the drying method was not efficient to remove the solvent (Li and Cl ions, as well as DMAc). Thus, the membranes were washed through dialysis during 3 days to guarantee complete removal of the solvent.

3.1.2 – Structural properties

3.1.2.1 – Fourier transformed infrared spectrometer coupled to attenuated total reflectance

To assess the influence of BC regeneration and drying process on BC structural and surface properties, the obtained BC films were analysed by FTIR–ATR. In Figure 13, it is possible to observe that both OD–BC and FD–BC have the characteristic peaks of cellulose at 3340, 2894, 1632, 1434, 1373, 1312, 1162, 1051, 995, 894 and 666 cm^{-1} (Figure 13). The strong and broad band at 3340 cm^{-1} corresponds to the O–H stretching of the hydroxyl groups. Sharper peaks on FD–BC are observed, which indicates a more regular structure. This is the case of the peak presented at 1107 cm^{-1} that is clearly evident on FD–BC while for the remaining BC matrixes this peak is overlaid with the neighbouring peaks. The peaks obtained at 1632 and 666 cm^{-1}, corresponding to the O–H bending and out of plane bending respectively (114). The peaks obtained at 2894, 1434, 1373, 1312 and 1051 cm^{-1} correspond to the CH and CH_2 bond vibrations (114). Moreover, there is also a characteristic peak at 1162 cm^{-1}, corresponding to the stretching of ether groups (C–O–C), which can be found within the glucopyranose ring and between the glucose monomers (114).

When comparing the FTIR spectra of R–BC with the spectra of OD–BC, the same peaks are observed, indicating that no chemical changes during the regeneration process of BC occurred. The absence of other peaks than those from BC, in R–BC sample, shows that the dialysis was successfully employed in the solvent remnants removal. However, the slight

changes in the relative intensity of the peaks seem to suggest that a change in the BC crystal structure may have occurred.

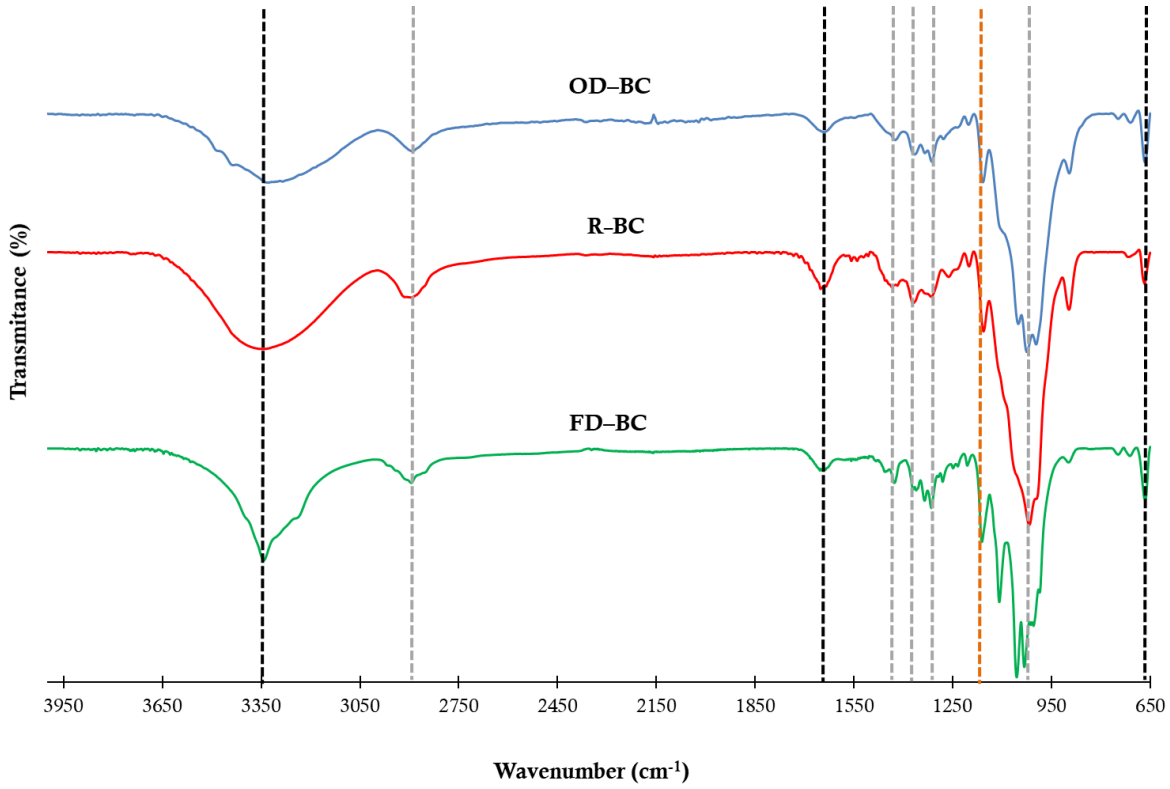

Figure 13 – FTIR–ATR spectra of oven dried (OD–BC), freeze dried (FD–BC) and regenerated (R–BC) BC. (▬) peaks corresponding to O-H bond (▬) peaks corresponding to the C-H bonds (▬) peaks corresponding to the C-O-C bonds.

3.1.2.3 – X-ray dispersive spectroscopy

The XRD spectra is found on Figure 14 and the CI were obtained by applying the equation developed by Segal et al. (104), which can be found on Table 3. OD–BC presented a CI of 79.15%, which is similar to the values found on literature, such as the ones reported by Yudianti et al. (115), of 75%, Cheng et al. (116), of 85%, and Tsouko et al.(117), of 81%. FD–BC presented a similar crystallinity index to OD–BC, which indicates that the same BC crystallinity is obtained by using both of drying methods. Both OD–BC and FD–BC present a XRD profile of cellulose type I, with characteristic peaks found at 14.5º, 16.73º and 22.7º,

corresponding to the (100), (010) and (110) planes, respectively (8, 115). The Z value for each sample was determined (Table 3), which suggests that the BC samples under analysis are rich in cellulose Iα (Z>1) (9).

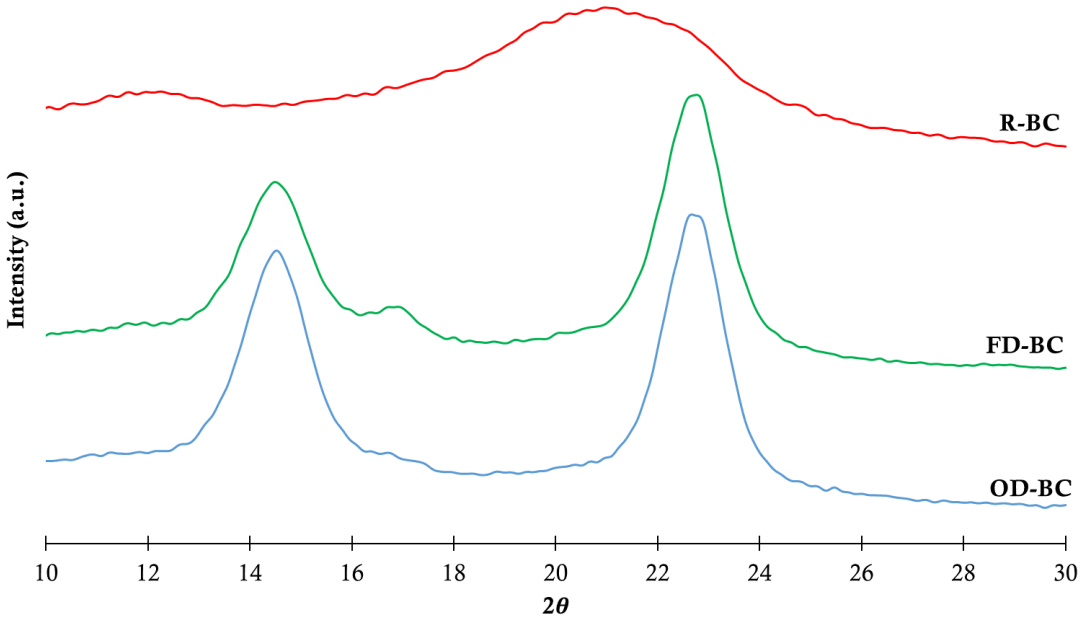

Figure 14 – X–ray diffraction profile of oven dried (OD–BC), freeze dried (FD–BC) and regenerated (R–BC) BC.

Table 3 – Crystallinity index (CI), crystallite size (CrS), Z value, and cellulose II/I ratio of oven dried (OD–BC), freeze dried (FD–BC) and regenerated (R–BC) BC.

	CI (%)	CrS (nm)	Z value	Cellulose II/I (A_{1370}/A_{666})
OD–BC	79.15	4.80	14.09	0.83
FD–BC	78.45	4.73	8.54	0.82
R–BC	47.74	1.14	–	1.70

In case of R–BC, it presents a CI of 47.74% which is lower when compared to both OD–BC and FD–BC. This is attributed to the rearrangement of the BC chains during the regeneration process, which led to an increase in the amorphous content (118). Not only the resulting cellulose matrix presented a lower crystallinity but it was also converted into type II cellulose, which is corroborated by a peak broadening on XRD as also by a small shift into

lower 2θ values (119). The peaks corresponding to the (110) and (002) are now found at 11.9º and 21.0º respectively (34, 43, 118). The peak broadening on XRD also indicates a lower crystallite size, as observed (1.14 nm), due to the amorphous content interference (120). The Z value for R–BC was not calculated since the equation is suited for cellulose I and the sample possesses the cellulose II allomorph. The conversion of BC from type I into type II of R–BC relative to OD–BC is supported by the ratio between the absorption at 1370 and 666 cm^{-1} (A_{1370}/A_{666}), according to Abbot et al. (119), presented on Table 3. It is observed an increase in the value for R–BC, whereas for FD–BC the value remains nearly constant, when compared to the OD–BC.

3.1.2.4 – Thermogravimetrical analysis

The thermal behaviour of the BC matrixes is depicted in Figure 15, representing the mass lost due to thermal degradation. All samples presented a slight mass loss until 125 ºC, corresponding to the residual moisture content. At higher temperatures, two degradation regions are observed (280–335 ºC and 335–506 ºC), in both OD–BC and R–BC, being more pronounced in the former. The presence of the second degradation region is characteristic when TGA is performed under an oxygen atmosphere, due do the extensive formation of char at the surface of the sample, which restricts the accessibility of oxygen (121-124). For FD–BC, a second degradation peak is nearly absent, where most of the sample was degraded on the first region. This could indicate a more regular structure, which corroborates the increase of the peaks sharpness on FTIR–ATR of FD–BC in comparison to OD–BC (Figure 13). The residue of the samples was lower than 1%, which means that for R–BC the dialysis was effective in the removal of Li^+ and Cl^- ions, as well as the initial step in the removal of the culture media impurities.

The onset degradation temperature obtained from TGA gives an indication of the thermal stability of the BC, where lower onset temperatures indicate that the thermal oxidation starts sooner, corresponding to a less stable material (125). Both OD–BC and FD–BC present a similar onset temperature (300.8 ºC for OD–BC and 304.9 ºC for FD–BC) which means that they present a similar thermal stability. In case of R–BC a lower onset temperature is observed (277.9 ºC) which evidences a lower thermal stability.

dTGA gives valuable information regarding the thermal degradation profile of the samples, where the peak minimum corresponds to the maximum temperature degradation (T_{max}). The main degradation step of oven dried BC presented a T_{max} at 335 ºC, which is close to the values found in the literature for other oven dried BC (350–360 ºC) (8, 118, 119). For FD–BC, the T_{max} value slightly decreases (3.6%), which indicates that the thermal stability is similar to OD–BC. On the other hand, for R–BC, an evident decrease in the T_{max} is observed (8.4%), which indicates a loss in the thermal stability of the sample. The decrease in both onset temperature and T_{max} value is closely correlated to the crystallinity index of the samples, where a decrease in the crystallinity index is followed by a loss in the thermal stability (8). For R–BC such happens because the solvent breaks the hydrogen bonds during the dissolution and in the regeneration step BC only partially recrystallizes, increasing the amorphous content when compared to the OD–BC, making cellulose more susceptible to thermal degradation (118).

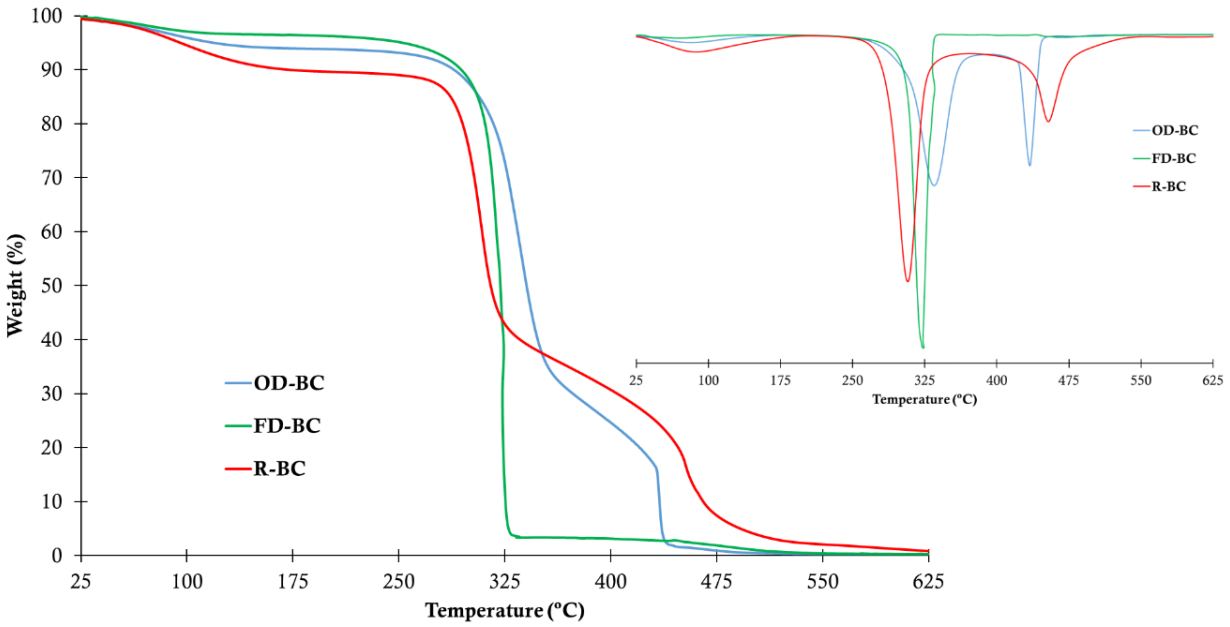

Figure 15 – Thermogravimetrical analysis (TGA and dTGA (inset)) of the oven dried (OD–BC), freeze dried (FD–BC) and regenerated (R–BC) BC.

3.1.3 – Morphological properties

3.1.3.1 – Scanning electronic microscopy and atomic force microscopy

The assessment of the changes at the BC surface through the employment of different drying methods and regeneration process was made by SEM and AFM. The SEM micrographs of the BC matrixes can be found in Figure 16. Through this figure it is possible to note that OD–BC presents entangled ribbon–shaped fibrils, producing a network–like structure, which agrees with the SEM micrographs found on literature (31, 115, 126). This structure confers BC unique properties such as large surface area and high water absorption ability (127). In FD–BC an evident increase in the number of fibrils is observed, which might be due to the preservation of its 3–D structure, making FD–BC more porous than OD–BC. OD–BC is more compact than FD–BC due to the collapse of the pores during oven drying. In case of R–BC, a smooth and compact surface is observed, with an absence of fibrils at the surface. The same observation was also reported by Lima et al. (34), Chen et al. (126) and Yudianti et al. (115). The most plausible explanation for the compact surface of R–BC is that during the regeneration process the BC chain aggregation was too fast, turning BC unable to create an organized structure.

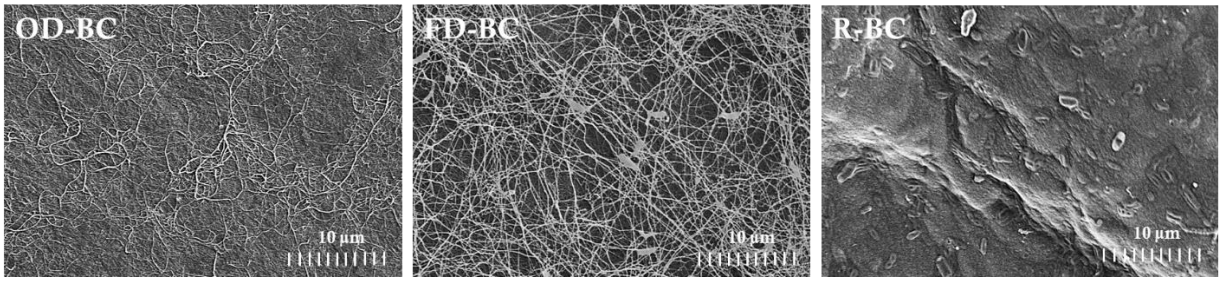

Figure 16 – SEM micrographs (3000x) of oven dried (OD–BC), freeze dried (FD–BC) and regenerated (R–BC) BC.

The surface morphology was further explored by AFM (Figure 17), where at a higher magnification for OD–BC and FD–BC the fibers can be clearly seen, presenting a width up to 0.1 µm. A smoother surface for FD–BC is observed (R_q of 16.2 nm), when compared to OD–BC (R_q of 25.2 nm). Moreover, the difference in the depth among the surface of the

sample is more pronounced on OD–BC when compared to FD–BC, which probably led into a rougher surface. This could mean that during the freeze drying process, the 3–D structure is preserved, whereas by oven drying BC the pores collapse leading to regions with different depths. This way, it is evidenced that the processing technique, applied prior to BC modification, has influence in its surface morphology.

In case of R–BC it does not present fibers at the surface (Figure 17C, F), which confirms the compact nature of the sample. Furthermore, a slight decrease in the roughness of the surface is observed (R_q of 22.0 nm) which could be correlated to a more constant depth of the sample.

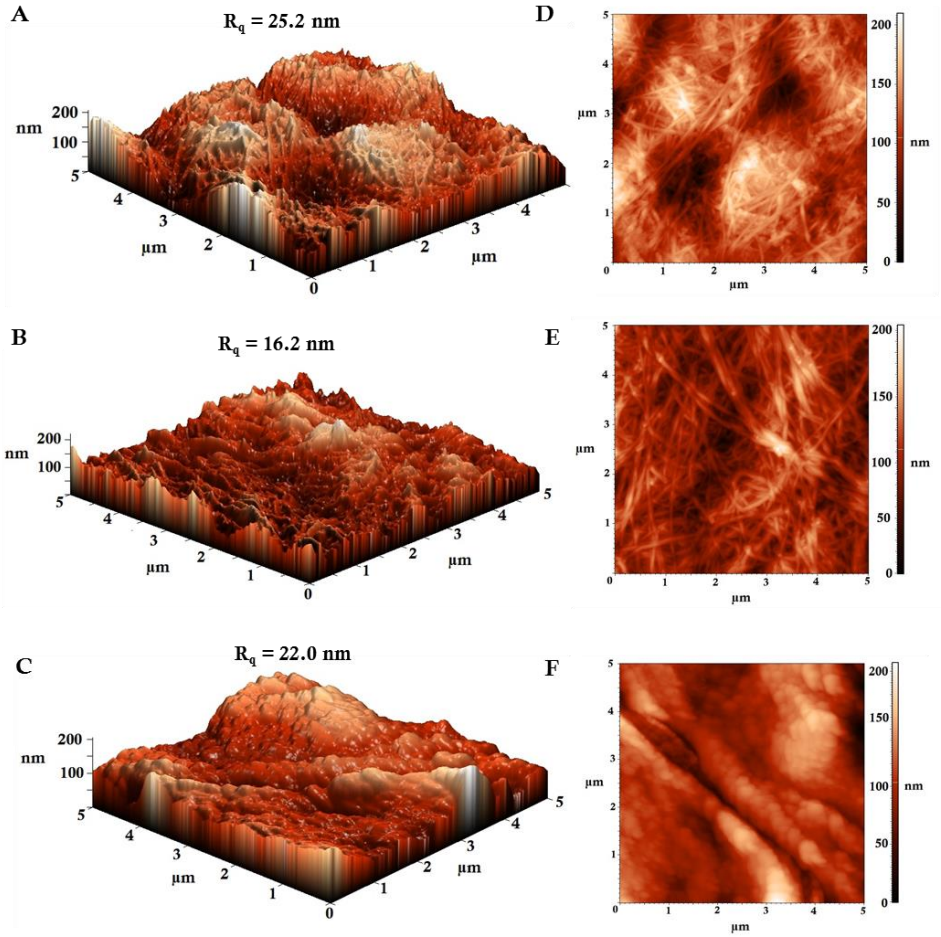

Figure 17 – 3D–and 2D–AFM of oven dried (OD–BC (A, D)), freeze dried (FD–BC (B, E)) and regenerated (R–BC (C, F)) BC.

3.1.4 – Swelling and contact angle analysis

The hydrophilic nature and water retention capacity of BC is positively affected by the fibril arrangement and high surface area per unit mass (128). To evaluate the rehydration capacity of the different BC matrixes, swelling studies were performed as can be seen in Figure 18. OD–BC presents a steady swell ability until 8 h, reaching a SW_{max} of 504% (Figure 18, Table 4). For FD–BC, the rehydration ability was greatly enhanced, being statistically different ($p < 0.05$), probably due to the preservation of the pores during the freeze drying process (Table 4). During oven drying the pores collapse, resulting in a compaction of the fibers, which is corroborated by the SEM photomicrographs (Figure 16). In case of the R–BC, the swelling stabilization occurs sooner, presenting a much lower SW_{max}, of 251%. This evidences that R–BC has a reduced reabsorption ability due to the compact structure.

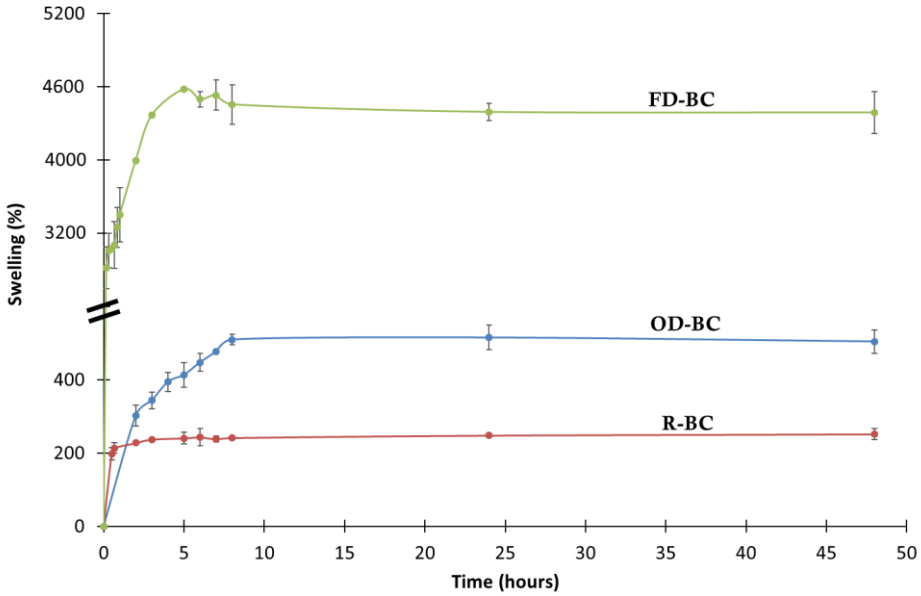

Figure 18 – Swelling behaviour of oven dried (OD–BC), freeze dried (FD–BC) and regenerated (R–BC) BC.

Table 4 – Swelling maximum (SW_{max}) and contact angle of oven dried (OD–BC), freeze dried (FD–BC) and regenerated (R–BC) BC.

	OD–BC	FD–BC	R–BC
SW_{max} (%)	504.0[a]	4515.8[c]	251.4[b]
Contact angle (°)	47.6	23.7	54.0

Values in same row not sharing a common superscript are statistically different ($p < 0.05$).

In addition to the swell ability, the contact angle measurements were performed for the several BC matrixes in order to search for changes in their hydrophilicity (Figure 19). OD–BC presented a contact angle of 47.6º, which is higher than the values reported in the literature (35.4º, 36.9º and 32.5º) (129-131). FD–BC presented a contact angle much lower (23.7º) than the value obtained for OD–BC, which indicates a higher hydrophilic behaviour. In contrast, R–BC presented a higher contact angle (54.0º), indicating an increase in the hydrophobic behaviour. The contact angle measurement agrees with the swelling maximum obtained, where the samples with higher contact angle presented lower swelling. A more hydrophobic behaviour is related to a lower water uptake of the sample. Thus, the hydrophobicity of the BC samples is the following: R–BC>OD–BC>FD–BC.

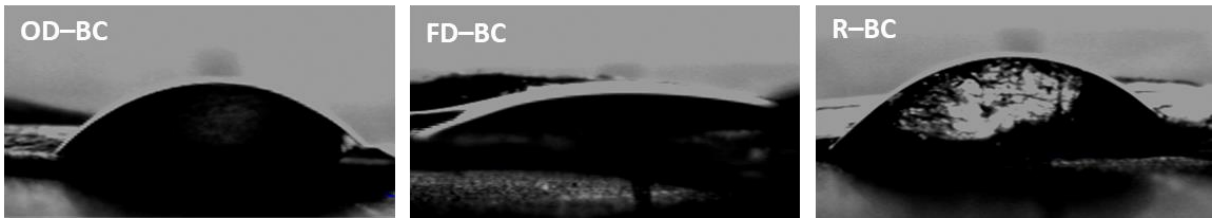

Figure 19 – Contact angle analysis of oven dried (OD–BC), freeze dried (FD–BC) and regenerated (R–BC) BC.

3.1.5 –Surface properties by IGC

To evaluate the effect of the drying method, as well as the regeneration process on the surface properties of BC, IGC was employed. Through this technique, the surface energy, the acid–base profile and surface nanomorphology were assessed. Regarding the surface energy, it was determined both surface components: γ_S^D and γ_S^{SP}. The acid–base profile was evaluated through the ΔG_S^{SP}, the K_a and K_b values. For the surface morphology S_{BET}, Dp and morphology index were determined.

3.1.5.1 – Surface energy

Papirer et al. (132) evaluated by IGC different cotton cellulose samples, stating that some factors such as crystallinity, diffusion of probes into the bulk and surface morphology

play an important role in the interaction between the probes and cellulose surface, thus influencing the IGC data. BC surface energy can be found in the literature, where Castro et al. (133) and Ferguson et al. (134) reported a γ_s^d value of 39.6 and 42.3 mJ/m^2 at 20 ºC and 30 ºC respectively. Although, some works that deviate from the previous BC surface energy values, such as by Pommet et al. (135), where a γ_s^d value of 61.0 mJ/m^2 was obtained. In this work, all BC matrixes had a γ_s^d close to the two values mentioned initially. Table 5 shows the surface energy values of the BC matrixes under study, as well as other parameters which will be further discussed.

Table 5 – Surface energy (γ_S^D, γ_S^{SP} and γ_S^{Total},) and acid/base behaviour (ethanol/tetrahydrofuran ΔG_S^{SP} ratio and K_b/K_a) of oven dried (OD–BC), freeze dried (FD–BC) and regenerated (R–BC) BC at 25 ºC.

Sample	γ_s^D (mJ/m^2)	γ_s^{SP} (mJ/m^2)	γ_S^{Total} (mJ/m^2)	ΔG_s^{SP} (Ethanol/Tetrahydrofuran)	Kb/Ka
OD–BC	37.65^a	37.64^a	75.29^a	0.79^a	0.75^a
FD–BC	35.15^{ab}	33.38^b	68.52^b	0.73^b	0.57^b
R–BC	34.58^b	28.51^c	63.08^c	0.70^b	0.57^b

Values in same column not sharing a common superscript are statistically different ($p < 0.05$). The error of the measurements was determined to be 3% and as such the upper and lower values from the average were determined. γ_S^D – Dispersive component of the surface energy; γ_S^{SP} – specific component of the surface energy, γ_S^{Total} – Total surface energy;

To understand the reason of the surface energy values fluctuations, the heterogeneity profile is assessed, which gives an indication of the number and energy of the surface active sites. The number of active sites is seen in the y axis whereas the energy of the active sites (adsorption potential) is related to the x axis. An increase in the y value corresponds to an increase in the number of active sites whereas an increase in the adsorption potential corresponds to an increase in the energy of the active sites. Compared with OD–BC, both FD–BC and R–BC showed a decrease in the γ_s^d value of 6.6% and 8.2%, respectively. Both results are supported by the heterogeneity profile of *n*–octane (Figure 20), where it is observed a decrease in the adsorption potential maximum (A_{max}), meaning the presence of active sites with lower energy. Taking OD–BC as a reference, it is observed that by freeze drying and regenerating BC, the A_{max} shifts into lower values while presenting a higher number of active

sites. Thus, it is observed that the drying treatments applied affect the BC chains at the surface.

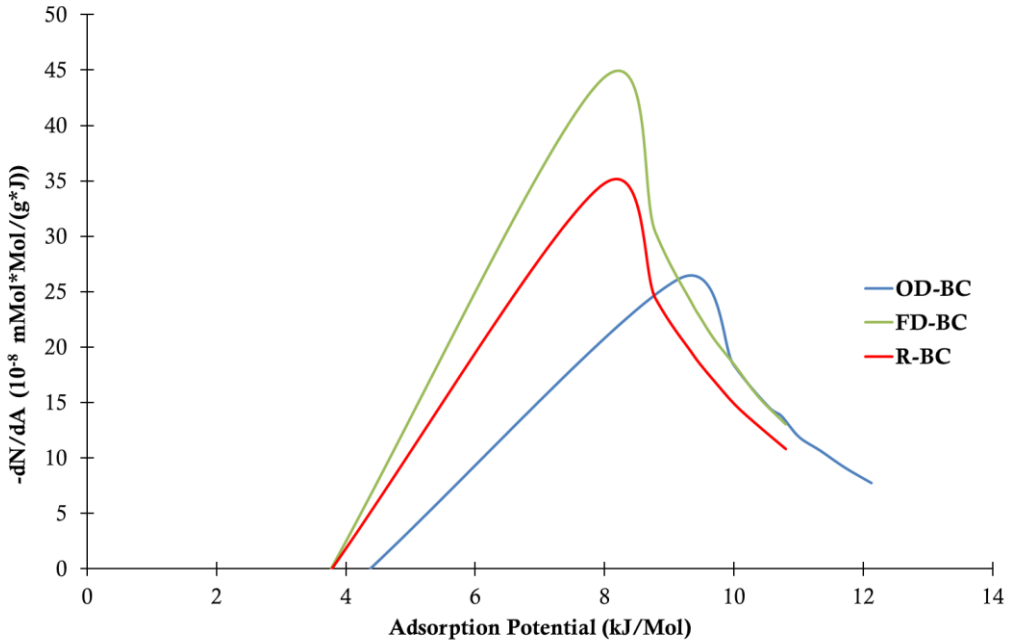

Figure 20 – Heterogeneity profile of *n*–octane on oven dried (OD–BC), freeze dried (FD–BC) and regenerated (R–BC) at 25 °C.

3.1.5.2 – Acid–base surface character

The injection of polar probes provided information regarding the acid–base properties of the BC surfaces under study. Differences in the ΔG_S^{SP} values of the BC matrixes in the polar probes were obtained (Figure 21), which indicates that the drying treatments applied on BC influence the polar groups arrangement at the surface. From the Figure 21, OD–BC presented higher interactions with all of the studied polar probes, followed by FD–BC and R–BC. This agrees with the polar surface energy (γ_s^{SP}), which follows the same trend (Table 5). The different probes have different energies of interaction since each probe interacts differently with the BC active sites. Acetonitrile has an amphoteric nature, which interacts with both acidic and basic groups. This means both acidic and basic groups can be found on the surface of the BC.

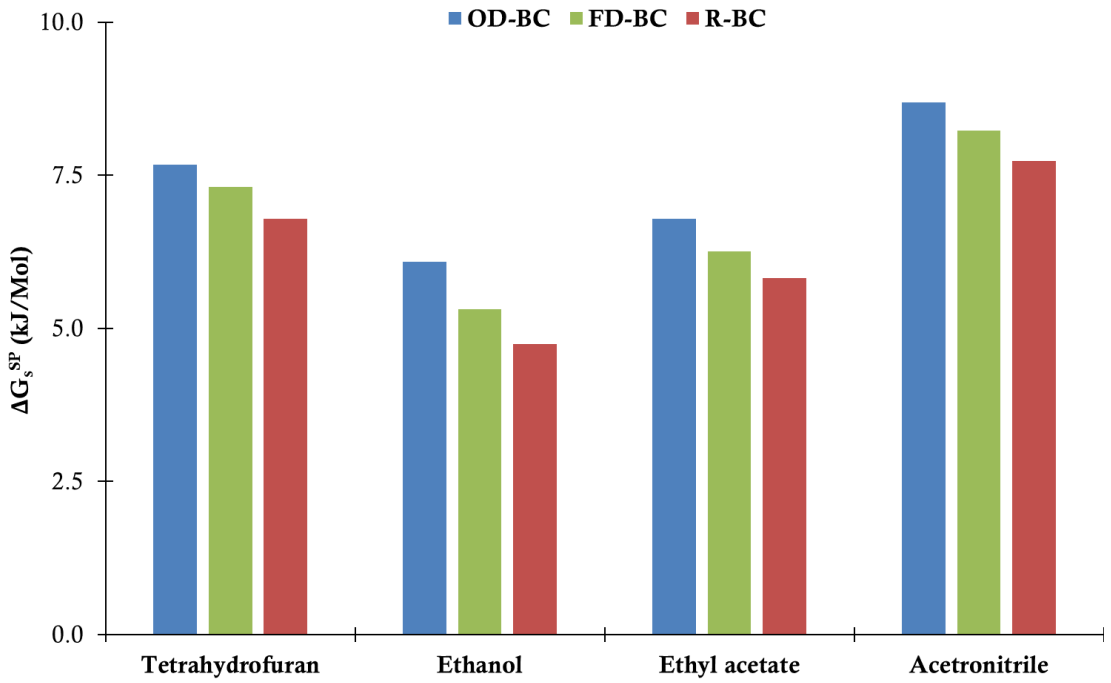

Figure 21 – Specific free energy of adsorption (ΔG_S^{SP}) of the polar probes on oven dried (OD–BC), freeze dried (FD–BC) and regenerated (R–BC) BC.

The interaction of the surface of BC matrixes with ethanol and tetrahydrofuran gives an insight about the basic and acid groups present in the surface, respectively. The ratio between these two probes is found in Table 5 (ΔG_S^{SP}(Ethanol/Tetrahydrofuran)). In both FD–BC and R–BC it is observed a decrease more evident in ethanol when compared to THF, indicating an increase in the acidic behaviour. The overall decrease in the interactions of the polar probes on R–BC in comparison to OD–BC is corroborated by both THF and EtOH heterogeneity profiles (Figure 22), which presents a lower amount of surface energy sites, as well as lower energy sites (lower A_{max} value). In case of FD–BC, through the heterogeneity profile of both THF and EtOH, the polar probes interacted with a higher amount of surface energy sites and at higher energies.

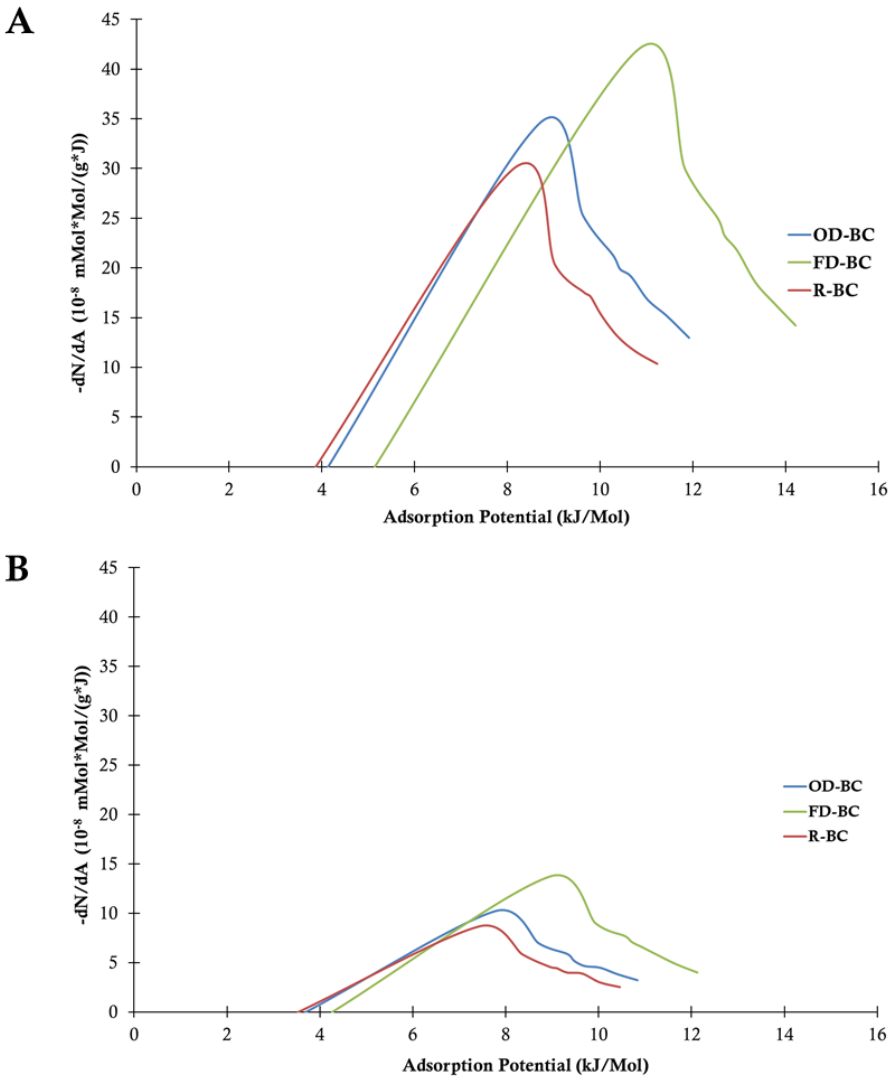

Figure 22 – Heterogeneity profile of ethanol (A) and tetrahydrofuran (B) on oven dried (OD–BC), freeze dried (FD–BC) and regenerated (R–BC) BC AT 25 ºC.

Observing cellulose chemical structure, it is expected an amphoteric behaviour, with a predominantly acidic character, due to the electron acceptor (H from hydroxyl groups) and electron donor (O from glucosidic bonds and hydroxyl groups) groups (136). The K_b/K_a ratio gives an indication of the basicity of the sample's surface, where: *(i)* a K_b/K_a higher than 1.1 indicates a basic surface, *(ii)* a K_b/K_a lower than 0.9 indicates a basic surface and *(iii)* a K_b/K_a between 0.9 and 1.1 indicates an amphoteric surface. OD–BC presented a K_b/K_a of 0.75, which shows an acidic behaviour. Castro et al. (133) reported the same acidic behaviour as the obtained OD–BC in the current work (Table 5). Other reports of acidic BC surfaces have

been found in the literature (135). Such phenomenon is observed due to the orientation of ether and hydroxyl groups in the BC surface. In both FD–BC and R–BC the acidic behaviour is more pronounced (K_b/K_a of 0.57), meaning that there is a higher number of acidic groups available in the surface, when compared to the basic groups. This parameter is corroborated by the ratio between the ΔG_s^{SP} of EtOH and THF presented in Table 5.

3.1.5.3 – Surface nanomorphology

As seen above, the drying and regeneration treatments influence the arrangement of the BC fibrils. Thus, the surface morphology properties of the BC matrixes were further explored by IGC, with the aim to complement the observations previously taken. The S_{BET} of OD–BC, FD–BC and R–BC were accessed through the isotherms using *n*–octane as the probe (Table 6). OD–BC presents a S_{BET} surface area of 4.59 m^2/g (Table 6), which is higher than the value reported by Castro et al., of 1.94 m^2/g (133). By freeze drying, a statistically significant increment ($p < 0.05$) of the S_{BET} surface area is observed which might be due to the preservation of the pore structure when compared to oven drying. The preservation of the pore structure made easier for probes to cross the sample, thus increasing the *Dp* value of FD–BC. The IGC measurements agrees with the SEM micrographs, where it is seen a more porous material in FD–BC when compared to OD–BC.

Also, it is observed that OD–BC presents a higher S_{BET} value when compared to R–BC (Table 6), which might be due to the compact nature of R–BC, as previously suggested. This property is corroborated by a lower *Dp*, which by having a more compact cellulose network, it takes longer for the probes to cross the sample. The SEM micrograph of R–BC corroborates the IGC measurements, where a more compact structure is observed when compared to OD–BC.

Table 6 – Surface area (S_{BET}), diffusion parameter (*Dp*) and morphology indexes of oven dried (OD–BC), freeze dried (FD–BC) and regenerated (R–BC) BC.

Sample	SBET (m^2/g)	Dp (cm^2/s)	Morphology index		
			2,5–Dimethylhexane	2,2,4–Trimethylpentane	Cyclooctane
OD–BC	4.59[a]	58.10[a]	0.66[a]	0.12[a]	1.92[a]
FD–BC	7.05[b]	76.78[b]	0.69[a]	0.57[b]	2.24[b]
R–BC	3.55[c]	12.9[c]	0.65[a]	0.60[b]	2.16[b]

Values in same column not sharing a common superscript are statistically different ($p < 0.05$). The error of the measurements was determined to be 3% and as such the upper and lower values from the average were determined.

The interaction of the probes with the surface is not only affected by the surface moiety of the sample but also by the topography of the surface (92). The morphology index gives the "deviation" of the sample surface from being planar, which was assessed with three probes: two branches alkanes (2,5–Dimethylhexane and 2,2,4–Trimethylpentane) and one cyclic alkane (cyclooctane). In all three matrixes, an adsorption phenomena (morphology index > 1) into the surface is observed for cyclooctane, whereas for the remaining probes a steric hindrance is depicted (morphology index < 1), as displayed by Figure 23. It is important to highlight that these differences are related to the volume of the probe. No statistical differences ($p < 0.05$) in the morphology index of 2,5–dimethylhexane were observed, as seen in Table 6, which indicates that this probe had the same accessibility to the surface in all samples, being unable to discern differences in the surface topography. On the other hand, with the other probes differences between OD–BC and the remaining BC samples were observed. Both probes had an increase in the morphology index in R–BC and FD–BC, which indicates that the surface of OD–BC is rougher than FD–BC and R–BC.

The morphology indexes are in accordance with the AFM results (see in section 3.1.3.1), where it is observed that the surface roughness (R_q) is lower when BC is freeze dried, when compared to the oven drying method. For R–BC, similarly to FD–BC, a decrease in the surface roughness is observed through AFM. This way, R–BC obtained a higher morphology index when compared to OD–BC.

In sum, through IGC results it is evidenciated that changes in the surface morphology occurred in regard to the different drying methods employed, as well through BC regeneration. OD–BC presented a more compact structure (lower S_{BET} and lower *Dp*) when compared to FD–BC which indicates a preservation of the supramolecular structure by freeze

drying. Troughout the regeneration process, the BC chains created a compact structure (lower S_{BET} and lower *Dp*) when compared to OD–BC. In terms of surface roughness OD–BC presented the lowest morphology index values indicating a rougher surface than FD–BC and R–BC, agreeing with the AFM results.

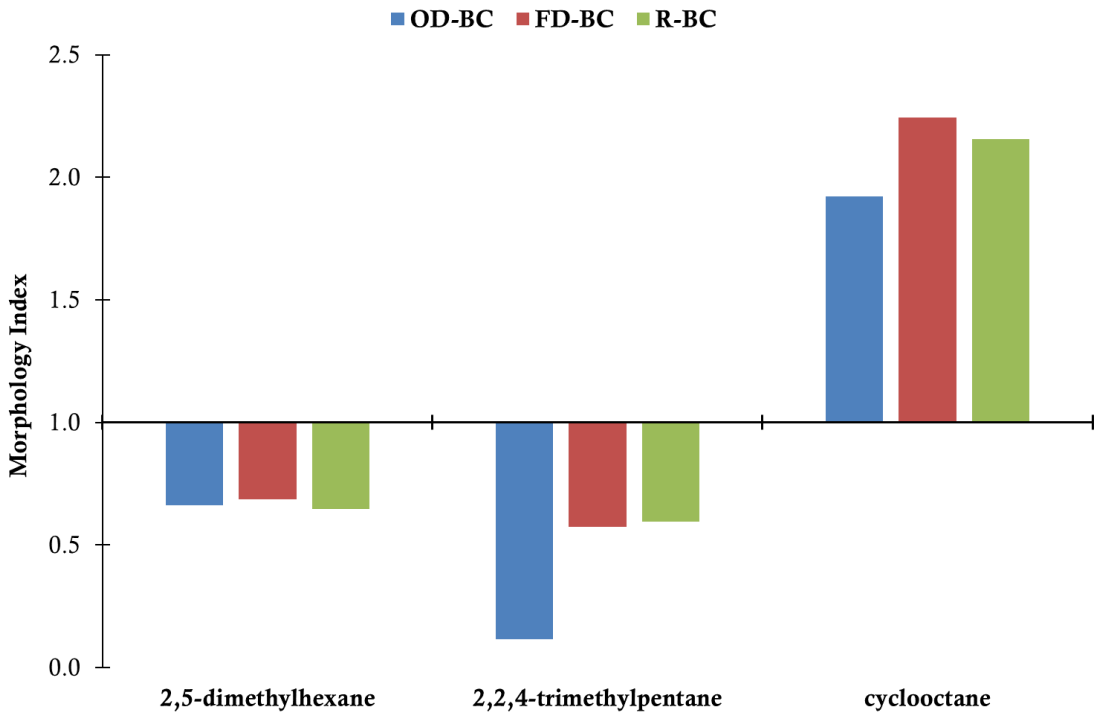

Figure 23 – Morphology index of oven dried (OD–BC), freeze dried (FD–BC) and regenerated (R–BC) BC.

3.2 – Influence of the different BC modification towards the synthesis of conductive BC/PANi nanocomposites

In the previous study, it was possible to observe that upon the processing technique the final properties of BC changed. For BC modification, FD–BC was chosen over OD–BC due to its increased swelling ability and BC structure preservation. Moreover, in this section, drained BC is added for comparative reasons, since BC is commonly modified in this way. In this section, a novel BC modification procedure, by using BC regeneration and aniline polymerization in one-step only, is presented and further discussed.

Conductive BC/PANi nanocomposites have been receiving increasing attention from the scientific community not only for electronic applications but also for the development of novel electro-responsive drug delivery mechanisms. However, despite these recent advances, the translation of the different polymerization methods on BC electrical, structural and surface properties have not been extensively studied. Thus, different modification methods comprising the use of different BC matrixes (drained, freeze dried and regenerated), as well as different polymerization methods (*in situ* and *ex situ* polymerization) were used. The samples were named according the type of BC matrix (drained – D, freeze dried – FD, regenerated – R) and polymerization method (*in situ* – IS, *ex situ* – ES).

3.2.1 – Structural properties

3.2.1.1 – Fourier transformed infrared spectrometer coupled to attenuated total reflectance

To confirm the polymerization of aniline onto BC network, FTIR–ATR was employed. Initially, PANi was studied, presenting characteristic peaks at 1557, 1483, 1332, 1290, 1235, 1128 and 788 cm^{-1} (Figure 24). The peaks at 1557 and 1128 cm^{-1} correspond to stretching of the C–N of benzenoid ring while the peaks at 1483 and 1373 cm^{-1} correspond to the stretching of C=N of the quinoid ring (68). Also, the peaks at 1290 and 1235 cm^{-1}

correspond to the stretching vibrations of C–N from secondary aromatic amines and C–N$^{\cdot+}$ in the polaron lattice of PANi, respectively (137). The peak at 788 cm^{-1} is related to the 1, 4–disubstitution of the aromatic ring (138), which is in agreement with the reaction mechanism presented in Figure 5.

The polymerization of aniline onto BC network was confirmed through the comparison of pure PANi and nanocomposite spectra (Figure 24) with the respective BC matrixes (Figure 13). Through the FTIR–ATR spectra it is possible to observe that the BC fibers were successfully coated with PANi, which means that both polymerization methods, as well as the BC matrixes used were viable for the synthesis of BC/PANi nanocomposites.

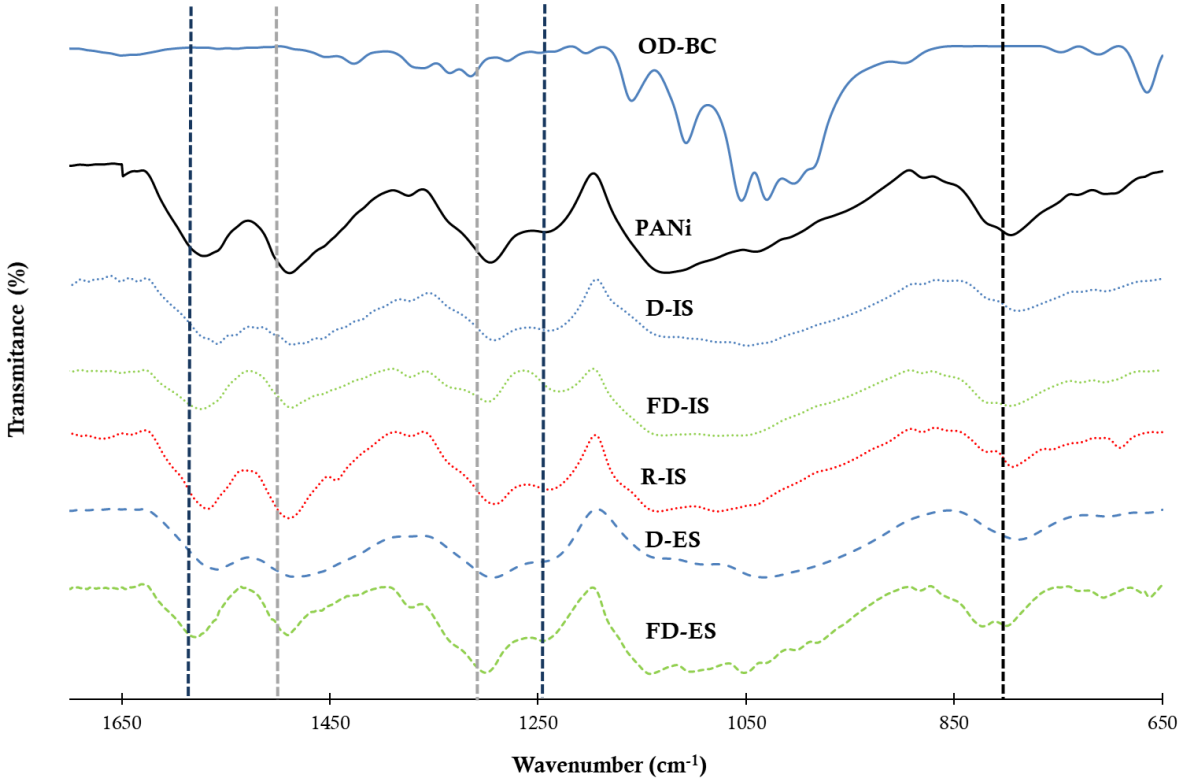

Figure 24 – FTIR–ATR spectra of PANi and BC/PANi nanocomposites. PANi – polyaniline; D–IS – drained BC/PANi *in situ* nanocomposite; FD–IS – freeze dried BC/PANi *in situ* nanocomposite; R–IS – regenerated BC/PANi nanocomposite; D–ES – drained BC/PANi *ex situ* nanocomposite; FD–ES – freeze dried BC/PANi *ex situ* nanocomposite.

3.2.1.2 – Electron dispersive X-ray spectroscopy

EDX was employed with the aim to evaluate the chemical composition at the samples surface. In Table 7, that displays the EDX data, it is possible to note several elements such as C, O, N, S and in some samples Cl were identified. The BC matrixes, prior to modification, presented only the elements C and O, indicating the absence of impurities. Furthermore. the presence of PANi on the surface of the nanocomposites is evidenced by the presence of N, along with an increase in the C due to the aromatic ring and a decrease on the amount of O, corroborating the data obtained from FTIR–ATR and IGC. A similar trend was previously reported by Shi et al. (2012) and Lee et al. (2012) through XPS, indicating the incorporation of PANi onto the BC fibers (23, 28). Moreover, the element S can be found on the nanocomposites due to the persulfate used in the synthesis, in which it is reduced into sulphate, establishing ionic interactions with the amine groups (23). Also, the presence of Cl was expected since the reaction was under a HCl acidic media.

Table 7 – Energy dispersive X–ray spectroscopy data of the BC matrixes and BC/PANi nanocomposites.

Sample	Elemental composition (%)				
	C	O	N	S	Cl
OD–BC	52.03	47.97	n.d.	n.d.	n.d.
FD–BC	59.37	40.63	n.d.	n.d.	n.d.
R–BC	47.96	52.04	n.d.	n.d.	n.d.
D–IS	71.15	14.22	10.66	3.97	n.d
FD–IS	70.78	16.94	10.91	1.36	n.d
R–IS	69.46	12.85	8.92	3.53	5.25
D–ES	68.52	14.81	7.93	8.09	0.66
FD–ES	73.23	12.03	12.29	2.20	0.25

n.d – not detected; OD–BC – oven dried BC; FD–BC – freeze dried BC; R–BC – regenerated BC; D–IS – drained BC/PANi *in situ* nanocomposite; FD–IS – freeze dried BC/PANi *in situ* nanocomposite; R–IS – regenerated BC/PANi nanocomposite D–ES – drained BC/PANi *ex situ* nanocomposite; FD–ES – freeze dried BC/PANi *ex situ* nanocomposite.

3.2.1.3 – X-ray dispersive spectroscopy

XRD was employed on the BC/PANi nanocomposites to study the effect of the polymerization of aniline onto BC network (Figure 25). With the introduction of the polymer into BC, it were obtained lower crystallinity indexes, when compared to the respective BC matrix prior to modification (Table 8). The decrease in the crystallinity index of BC with the polymerization of PANi was also reported by Wang et al. (28), Marins et al (68), Zhang et al. (69) and He et al. (152), which might be due to: *(i)* the introduction of amorphous PANi and/or *(ii)* the weakening of the intermolecular bonds established between the cellulose fibers in order to interact with the amine groups of polyaniline. Moreover, both drained and freeze dried BC/PANi nanocomposites present the characteristic type I cellulose peaks, while R–IS present type II cellulose, which indicates that no changes in the BC polymorph structure occurred with the PANi introduction, when compared to the initial matrixes (Figure 14).

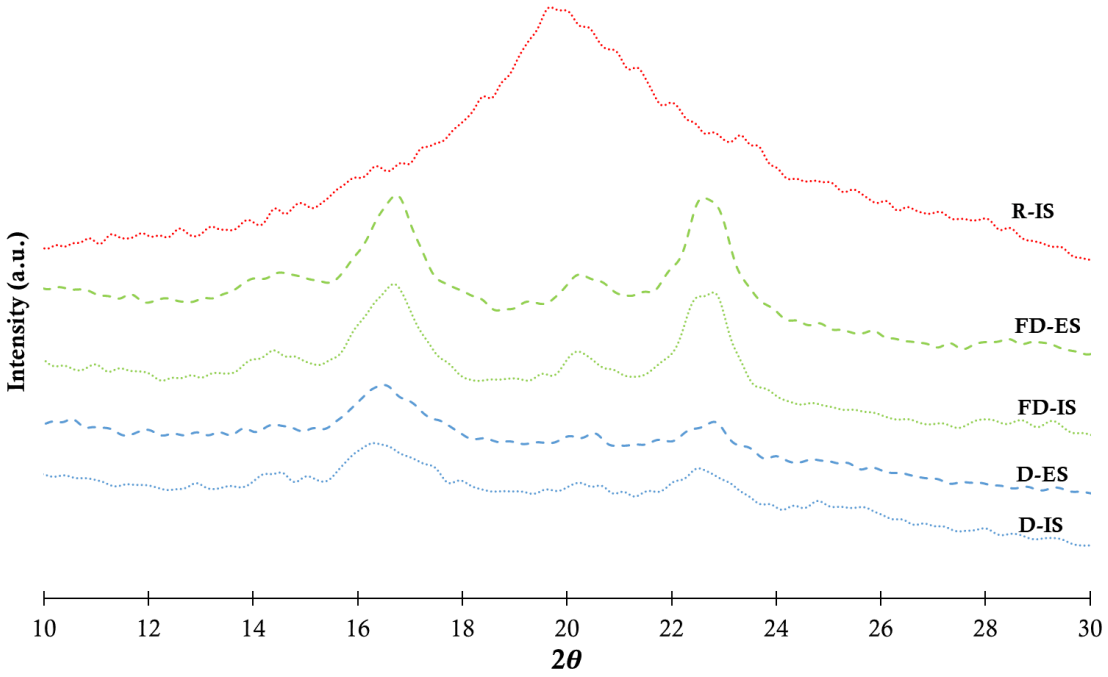

Figure 25 – X–ray diffraction profiles of BC/PANi nanocomposites. D–IS – drained BC/PANi *in situ* nanocomposite; FD–IS – freeze dried BC/PANi *in situ* nanocomposite; R–IS – regenerated BC/PANi *in situ* nanocomposite; D–ES – drained BC/PANi *ex situ* nanocomposite; FD–ES – freeze dried BC/PANi *ex situ* nanocomposite.

Slight differences in BC crystallinity are observed upon the different polymerization methods used (Table 8), meaning that the nanocomposite crystallinity is barely influenced by the employment of *in situ* or *ex situ* polymerization methods. This is observed in both BC matrixes (drained and FD–BC), where *in situ* and *ex situ* polymerization was applied. On the other hand, the crystallinity was greatly influenced by the BC matrix used on the polymerization process. The crystallinity of D–IS and D–ES BC/PANi nanocomposites greatly reduces (about 60%), whereas for FD–IS and FD–ES BC/PANi nanocomposites it decreases moderately (around 30%) in comparison to the corresponding BC matrix. This indicates that FD–BC could maintain its initial 3D structure, unlike drained BC. For R–IS BC/PANi nanocomposite, BC presents a type II cellulose due to the regeneration process, as discussed in the previous chapter, with a crystallinity index similar to R–BC.

Table 8 – Crystallinity index (CI), and Temperature maximum (T_{max}) obtained through XRD and TGA analysis, respectively, for the BC matrixes and BC/PANi nanocomposites.

Sample	CI (%)	$Tmax_1$ (ºC)	$Tmax_2$ (ºC)
OD–BC	79.15	335	-
FD–BC	78.45	323	-
R–BC	47.74	307	-
D–IS	19.48	254	452
FD–IS	46.22	251	491
R–IS	50.20	232	444
D–ES	18.59	254	449
FD–ES	53.72	276	475

OD–BC – oven dried BC; FD–BC – freeze dried dried BC; R–BC – regenerated BC; D–IS – drained BC/PANi *in situ* nanocomposite; FD–IS – freeze dried BC/PANi *in situ* nanocomposite; R–IS – regenerated BC/PANi nanocomposite; D–ES – drained BC/PANi *ex situ* nanocomposite; FD–ES – freeze dried BC/PANi *ex situ* nanocomposite.

3.2.1.4 – Thermogravimetrical analysis

TGA and dTGA were used to study the thermal stability of the nanocomposites. Figure 26 presents the degradation profiles obtained for the several samples studied. Most of the obtained BC/PANi nanocomposites present three degradation peaks, except for R–IS BC/PANi nanocomposite, where during the 400–475 ºC region it presents a complex degradation profile, as seen by its dTGA (Figure 26). This complexity, in the R–IS BC/PANi nanocomposite, could indicate different degrees of polymerization of PANi probably due to the different reaction media conditions (presence of DMAc and LiCl) during the polymerization.

For all nanocomposites, the first weight loss under 125 ºC corresponds to residual water that can be found on the samples, whereas the second weight loss, with a maximum temperature degradation (T_{max1}) at around 250 ºC, corresponds to the degradation of the BC chains (26, 66). In Table 8, it is possible to observe that lower T_{max1} were obtained for the BC/PANi nanocomposites when compared to the unmodified BC matrixes. This observation can be explained by the weakening of the hydrogen bonds between the cellulose chains due to the PANi introduction. This result corroborates the crystallinity indexes obtained through XRD, where it is observed a decrease on the crystallinity due to the incorporation of the conductive polymer. R–IS presented the lowest degradation temperature (231.8 ºC) when compared with the remaining nanocomposites which is probably due to the lower crystallinity of R–BC.

For the degradation step related to BC (T_{max1}) there are no significant differences between D–IS and D–ES BC/PANi nanocomposites, whereas for FD–IS and FD–ES BC/PANi nanocomposites, a small difference of 26 ºC is observed. Also, by using different BC matrixes, no significant differences in T_{max1} values are obtained. In case of BC/PANi nanocomposites, the last degradation region is attributed to the PANi backbone decomposition. This way, the TGA profile evidences the PANi incorporation into BC. Freeze dried BC/PANi nanocomposites (FD–IS and FD–ES) present a higher T_{max2} in comparison with drained BC/PANi nanocomposites (D–IS and D–ES). R–IS presents a similar T_{max2} as both drained BC/PANi nanocomposites. Changes in the T_{max2} value

indicate that PANi synthesized in the presence of a FD–BC led into a more thermal stable conductive polymer, probably due to changes in chain orientation and/or molecular weight.

Considering the overall TGA data, it is observed that with the introduction of the polymer a less stable nanomaterial is obtained (lower onset degradation temperatures).

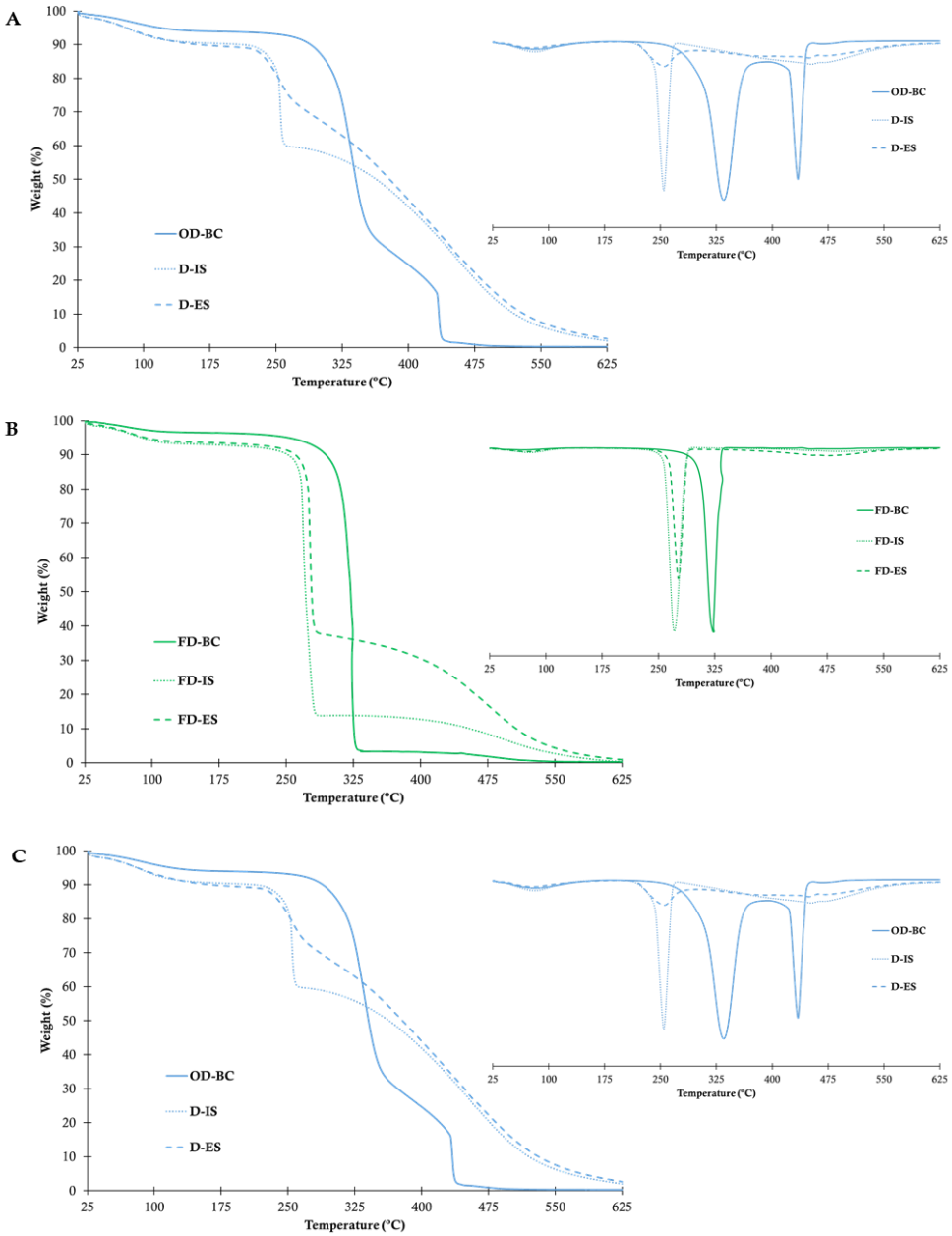

Figure 26 – Thermogravimetrical analysis (TGA and dTGA (inset)) of drained (A), freeze dried (B) and regenerated (C) BC/PANi nanocomposites. D–IS – drained BC/PANi *in situ* nanocomposite; FD–IS – freeze dried BC/PANi *in situ* nanocomposite; R–IS – regenerated BC/PANi nanocomposite; D–ES – drained BC/PANi *ex situ* nanocomposite; FD–ES – freeze dried BC/PANi *ex situ* nanocomposite.

3.2.2 – Morphological properties

3.2.2.1 – Scanning electronic microscopy and atomic force microscopy

SEM and AFM were carried out in the current study with the aim to observe the PANi incorporation into the BC matrixes. The polymerization of aniline onto the BC matrixes was successful, as seen by the SEM micrographs presented on Figure 27. On both D–IS and D–ES BC/PANi nanocomposites it can be seen fibers with a higher width when compared to OD–BC, indicating an effective coating of PANi on the BC fibers. In case of both FD–BC/PANi nanocomposites, the incorporation of PANi is slightly different, where it can be observed flakes/granules, and nearly absence of fibers at the surface. On R–IS BC/PANi nanocomposite the surface became less smooth with the presence of PANi flakes on the surface. In all nanocomposites, a more compact surface is observed which indicates that the PANi incorporation covered the pores of the BC matrixes.

The surface morphology of the BC/PANi nanocomposites was further explored through AFM (Figure 28). When comparing the surface roughness (R_q) values of D–IS and FD–IS BC/PANi nanocomposites with D–ES and FD–ES BC/PANi nanocomposites respectively, there are no large differences, meaning that the polymerization process used (*in situ* and *ex situ* polymerization) does not influence the surface roughness.

When using different BC matrixes, it is seen that D–IS and D–ES BC/PANi nanocomposites are slightly rougher when compared to FD–IS and FD–ES BC/PANi nanocomposites respectively. In case of R–IS, it presented the greatest increase in the surface roughness in comparison to the remaining BC/PANi nanocomposites. This corroborates the SEM results where R–BC shifts from a compact smooth surface into a rougher surface.

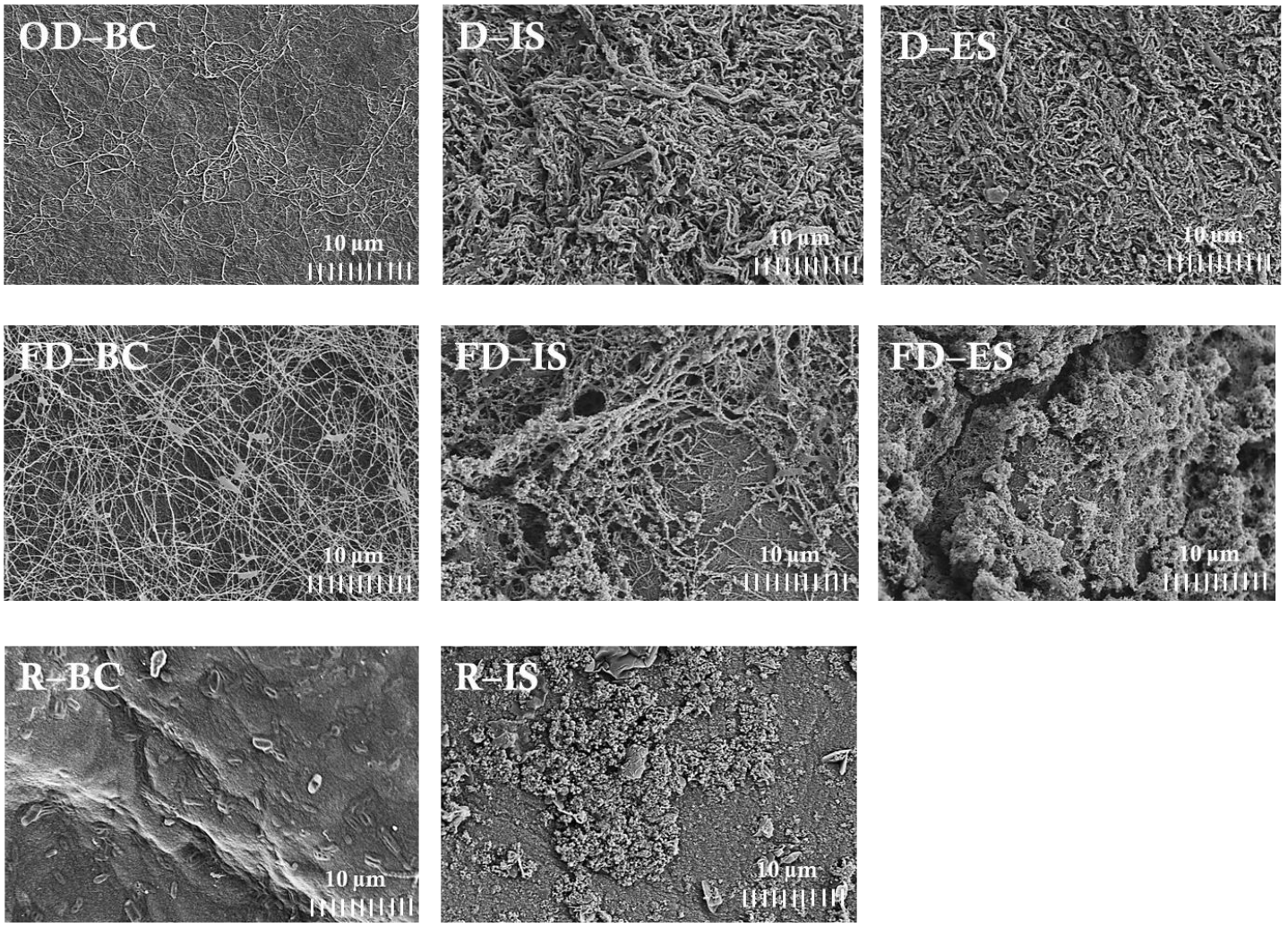

Figure 27 – SEM micrographs (3000x) of BC matrixes and BC/PANi nanocomposites. OD–BC – oven dried BC; D–IS – drained BC/PANi *in situ* nanocomposite; D–ES – drained BC/PANi *ex situ* nanocomposite; FD–BC – freeze dried BC; FD–IS – freeze dried BC/PANi *in situ* nanocomposite; FD–ES – freeze dried BC/PANi *ex situ* nanocomposite; R–BC – regenerated BC; R–IS – regenerated BC/PANi nanocomposite.

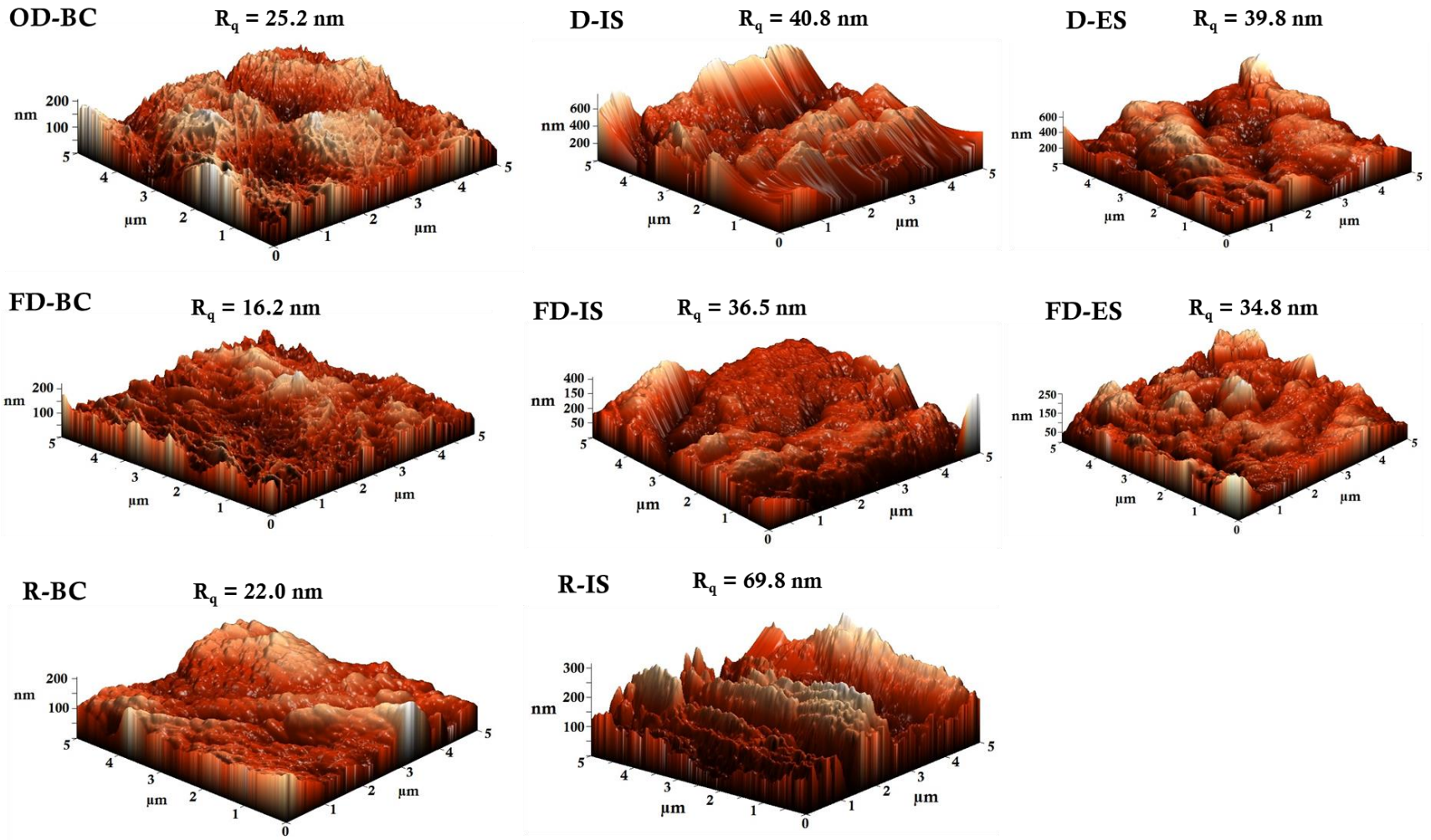

Figure 28 – 3D–AFM of BC matrixes and BC/PANi nanocomposites: OD–BC – oven dried BC; D–IS – drained BC/PANi *in situ* nanocomposite; D–ES – drained BC/PANi *ex situ* nanocomposite; FD–BC – freeze dried BC; FD–IS – freeze dried BC/PANi *in situ* nanocomposite; FD–ES – freeze dried BC/PANi *ex situ* nanocomposite; R–BC – regenerated BC; R–IS – regenerated BC/PANi nanocomposite.

3.2.3 – Polymer uptake and Electrical conductivity

The polymer uptake and electrical conductivity of BC/PANi nanocomposites were evaluated to assess the influence of the polymerization method, as well as the employment of different BC matrixes into the synthesis of BC/PANi nanocomposites. The results are presented on Table 9. The polymer content, which was determined by equation 14, indicates that the *in situ* polymerization positively influences the polymer content incorporated. Moreover, the electrical conductivity of both *in situ* nanocomposites (D–IS and FD–IS) is 1.9–2.6 times higher than the nanocomposites obtained through *ex situ* chemical polymerization, which could indicate changes in the PANi chain orientation and/or molecular weight. D–IS BC/PANi nanocomposite presented the highest conductivity. Thus, the underlying BC modification method should be highlighted as the most suitable for highly conductive BC/PANi nanocomposites synthesis.

D–IS and D–ES BC/PANi nanocomposites presented lower polymer contents in comparison to FD–IS and FD–ES respectively, which indicates the influence of the BC matrix used. FD–BC matrix presents a high porosity and high swelling ratio, which should contribute to higher incorporation yields when compared to drained BC. Nevertheless, higher conductivities were obtained for D–IS and D–ES BC/PANi nanocomposite in comparison to the remaining nanocomposites (FD–IS, FD–ES and R–IS). According to Kaur et al. (139), the materials obtained fall within the range of semiconductive materials (10^{-7}–10^{0} S/cm). In the literature, many authors reported BC/PANi nanocomposites, with different electrical conductivities, ranging from 10^{-7}–10^{-1} S/cm (23, 27, 59, 66, 67).

Table 9 – Polymer content and electrical conductivity of the BC/PANi nanocomposites.

Sample	Polymer content (%)	Conductivity (10^{-3} S/cm)
D–IS	$43.39^{a, b} \pm 2.93$	$139.24^{a} \pm 28.16$
FD–IS	$53.67^{b} \pm 7.44$	$3.11^{b} \pm 0.54$
R–IS	$42.90^{a} \pm 2.66$	$1.48^{b} \pm 0.16$
D–ES	$25.24^{c} \pm 4.19$	$55.32^{c} \pm 12.74$
FD–ES	$48.34^{a, b} \pm 1.42$	$1.60^{b} \pm 0.13$

Values in same column not sharing a common superscript are statistically different ($p < 0.05$). The error of the measurements was determined to be 3% and as such the upper and lower values from the average were determined. IS – drained BC/PANi *in situ* nanocomposite; FD–IS – freeze dried BC/PANi *in situ* nanocomposite; R–IS – regenerated BC/PANi nanocomposite; D–ES – drained BC/PANi *ex situ* nanocomposite; FD–ES – freeze dried BC/PANi *ex situ* nanocomposite.

3.2.4 – Swelling and contact angle analysis

Swelling studies were performed to evaluate the rehydration ability of the synthesized BC/PANi nanocomposites through the immersion in water and to evaluate the weight increase over time (Figure 29).

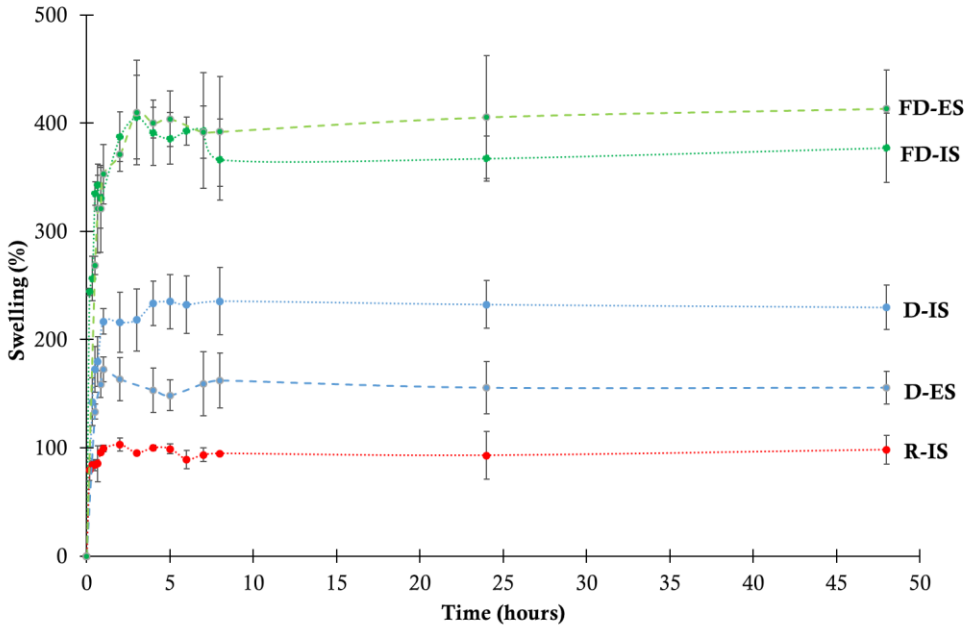

Figure 29 – Swelling behaviour of BC/PANi nanocomposites. D–IS – drained BC/PANi *in situ* nanocomposite; FD–IS – freeze dried BC/PANi *in situ* nanocomposite; R–IS – regenerated BC/PANi nanocomposite; D–ES – drained BC/PANi *ex situ* nanocomposite; FD–ES – freeze dried BC/PANi *ex situ* nanocomposite.

Comparing the swelling values of the BC matrixes (see in section 3.1.4) with the BC/PANi nanocomposites, by introducing PANi a significant decrease in the SW_{max} was observed (Table 10), which can be due to the hydrophobic nature of PANi. Taking the respective BC membranes as a reference, for FD–BC/PANi nanocomposites the swelling ratio decreases more significantly on (around 90%) when compared to the remaining BC/PANi nanocomposites, that present a decrease around 60% in their swelling ratio when compared to the reference BC matrix. Through the comparison of the BC/PANi nanocomposites, both FD–IS and FD–ES presented a higher swelling ratio when compared to D–IS and D–ES, while R–IS was the nanocomposite that presented the lowest swelling. This way, it is observed that the swelling ratio was influenced mostly by the BC matrix used.

Table 10 – Swelling maximum (SW_{max}) and contact angle of the BC matrixes and BC/PANi nanocomposites.

	SW_{max} (%)	Contact angle (º)
OD–BC	504.0[a]	47.6
FD–BC	4515.8[b]	54.0
R–BC	251.4[c]	23.7
D–IS	229.7[a]	54.3
FD–IS	377.3[b]	76.8
R–IS	98.1[c]	85.6
D–ES	155.6[d]	71.1
FD–ES	413.6[b]	64.8

Values in same row not sharing a common superscript are statistically different ($p < 0.05$). OD–BC – oven dried BC; FD–BC – freeze dried BC; R–BC – regenerated BC; D–IS – drained BC/PANi *in situ* nanocomposite; FD–IS – freeze dried BC/PANi *in situ* nanocomposite; R–IS – regenerated BC/PANi nanocomposite; D–ES – drained BC/PANi *ex situ* nanocomposite; FD–ES – freeze dried BC/PANi *ex situ* nanocomposite.

To understand the wetting properties of the BC/PANi nanocomposites, the water contact angle of the nanocomposites was determined, which can be found on Figure 30. It was observed an increase in the contact angle on all nanocomposites, when compared to the respective BC matrix (1.1–2.7 times higher). The D–IS BC/PANi nanocomposite presented the lowest contact angle (54.3º) whereas R–IS BC/PANi nanocomposite presented the highest contact angle (85.6º). However, no direct correlation observed between the water contact angle of the samples with the polymerization method or BC matrix employed for the synthesis of BC/PANi nanocomposites. This observation can be correlated with the electrical

conductivity obtained, where the samples with higher conductivity presented a lower water contact angle, similar to the results reported by Liu et al. (140).

Taking into account of the different contact angle values, the order of hydrophobicity of the samples is the following: R–IS>FD–IS> D–ES>FD–ES>D–IS.

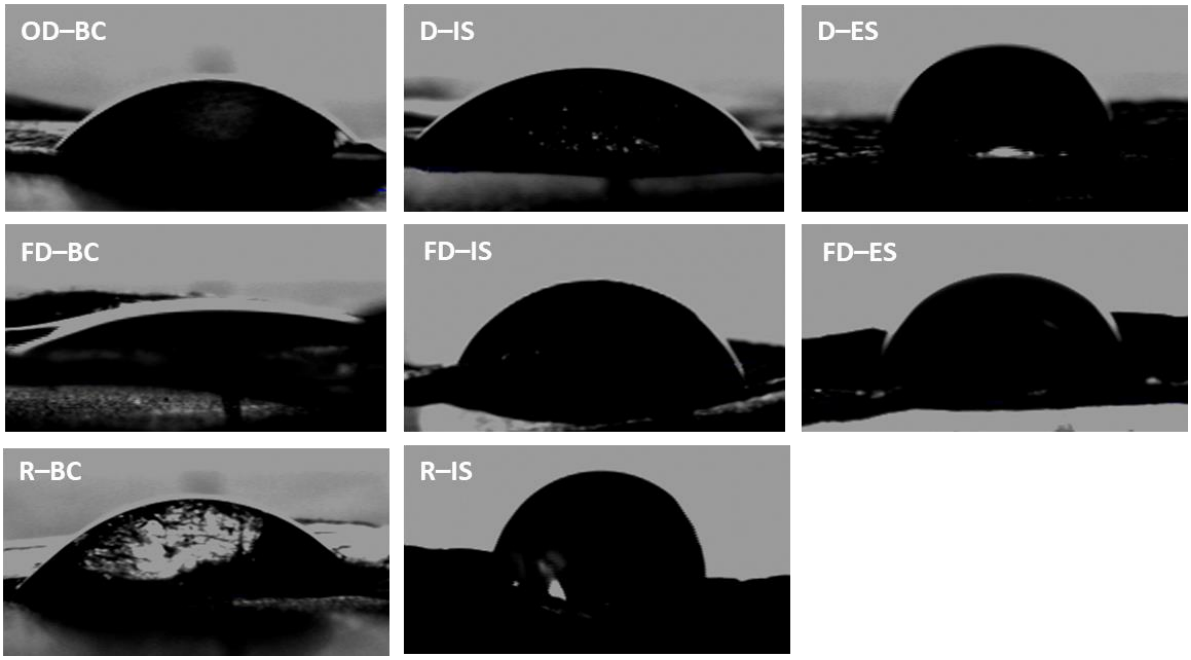

Figure 30 – Contact angle analysis of the BC matrixes and BC/PANi nanocomposites: OD–BC – oven dried BC; FD–BC – freeze dried BC; R–BC – regenerated BC; PANi – polyaniline; D–IS – drained BC/PANi *in situ* nanocomposite; FD–IS – freeze dried BC/PANi *in situ* nanocomposite; R–IS – regenerated BC/PANi nanocomposite; D–ES – drained BC/PANi *ex situ* nanocomposite; FD–ES – freeze dried BC/PANi *ex situ* nanocomposite.

3.2.5 – Surface properties by IGC

3.2.5.1 – Surface energy

IGC was employed to evaluate changes at the surface of BC with the incorporation of the PANi polymer. With the introduction of the conductive polymer, the γ_s^{total} of the BC matrixes significantly increases (Table 11) due to the PANi coating on the surface, which presents a high γ_s^{total} value (Figure 31). This is reflected in the increase of both γ_s^{sp} and γ_s^{d} values (Table 11). Through Tukey's post hoc analysis, it is possible to observe that the data for γ_s^{total} splits into three groups: *(i)* drained BC/PANi nanocomposites, *(ii)* regenerated and freeze dried BC/PANi nanocomposites and *(iii)* PANi powder (Table 11). This indicates that the BC matrix had an influence in the surface properties of the nanocomposite.

Table 11 – Surface energy (γ_S^D and γ_S^{SP}, γ_S^{Total}) and acid/base behaviour (K_b/K_a and ethanol/tetrahydrofuran ΔG_S^{SP} ratio) of BC/PANi nanocomposites at 25 ºC.

Sample	$\boldsymbol{\gamma_S^D}$ (mJ/m²)	$\boldsymbol{\gamma_S^{SP}}$ (mJ/m²)	$\boldsymbol{\gamma_s^{Total}}$ (mJ/m²)	ΔG_s^{SP} (Ethanol/Tetrahydrofuran)	Kb/Ka
OD–BC	37.65[a]	37.64[a]	75.29[a]	0.79[a]	0.75[a]
FD–BC	35.15[ab]	33.38[b]	68.52[b]	0.73[b]	0.57[b]
R–BC	34.58[b]	28.51[c]	63.08[c]	0.70[b]	0.57[b]
PANi	119.85[a]	123.8[a]	243.65[a]	1.20[ab]	3.46[a]
D–IS	64.40[b]	65.97[b]	130.37[b]	1.20[ab]	2.55[b]
FD–IS	67.74[b]	88.70[c]	156.44[c]	1.07[c]	1.88[c]
R–IS	51.91[c]	105.90[c]	157.81[c]	0.99[c]	1.91[c]
D–ES	63.70[b]	63.92[b]	127.62[b]	1.27[b]	2.26[d]
FD–ES	75.00[d]	88.88[c]	163.88[c]	1.12[ac]	3.77[e]

Values in same column not sharing a common superscript are statistically different ($p < 0.05$). The error of the measurements was determined to be 3% and as such the upper and lower values from the average were determined. OD–BC – oven dried BC; FD–BC – freeze dried BC; R–BC – regenerated BC; D–IS – drained BC/PANi *in situ* nanocomposite; FD–IS – freeze dried BC/PANi *in situ* nanocomposite; R–IS – regenerated BC/PANi nanocomposite D–ES – drained BC/PANi *ex situ* nanocomposite; FD–ES – freeze dried BC/PANi *ex situ* nanocomposite. γ_s^{Total} – Total surface energy; γ_s^{d} – Dispersive component of the surface energy; γ_s^{sp} – specific component of the surface energy.

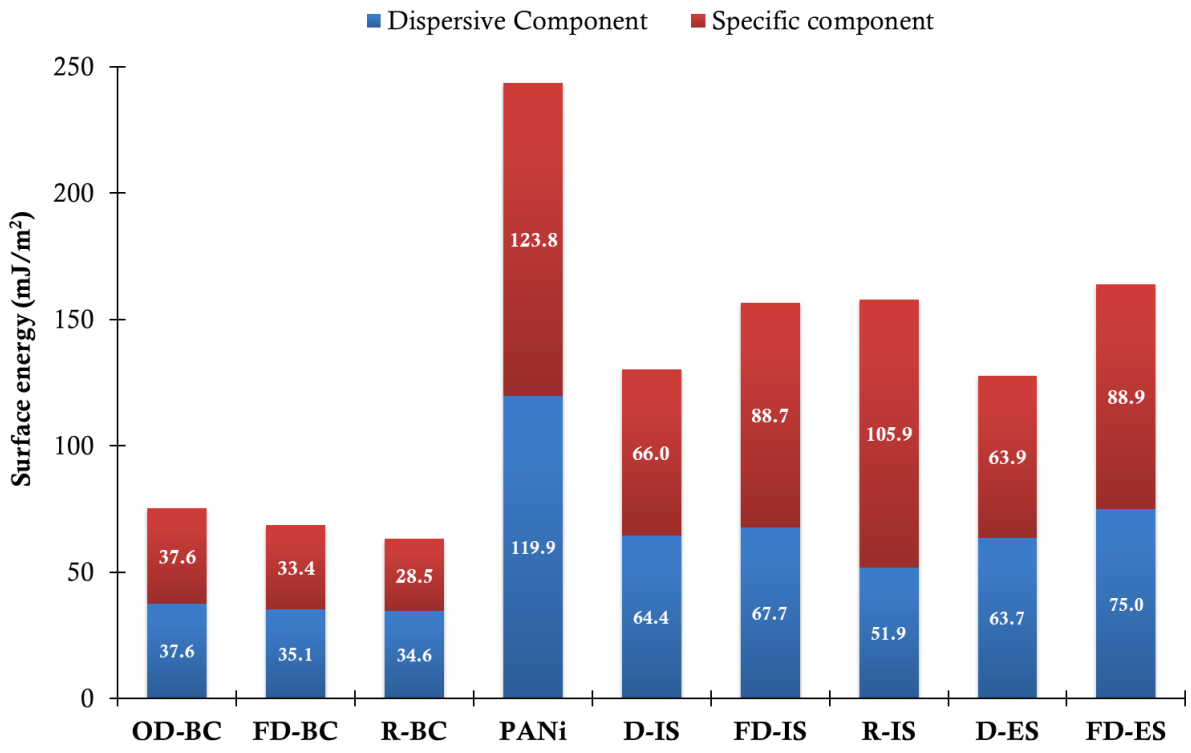

Figure 31 – Surface energy measurements obtained at 25 °C from BC matrixes and BC/PANi nanocomposites. OD–BC – oven dried BC; FD–BC – freeze dried BC; R–BC – regenerated BC; PANi – polyaniline; D–IS – drained BC/PANi *in situ* nanocomposite; FD–IS – freeze dried BC/PANi *in situ* nanocomposite; R–IS – regenerated BC/PANi nanocomposite; D–ES – drained BC/PANi *ex situ* nanocomposite; FD–ES – freeze dried BC/PANi *ex situ* nanocomposite.

The increased γ_S^D is corroborated by an increase of the C amount through EDX (Table 7), where a higher number of C-H groups are present at the BC/PANi nanocomposites surface, in comparison to the BC matrixes. The heterogeneity profile of n-octane for all samples studied in this work can be found in Figure 32. It is possible to observe that PANi presents higher adsorption potential values when compared to the BC matrixes. Thus, with the incorporation of PANi, is expected an increase in the energy of the active sites. Such was observed, which corroborates the increase in the γ_S^D values. Moreover, the increased γ_s^d can be related to an increase of the surface hydrophobicity, as seen through the contact angles.

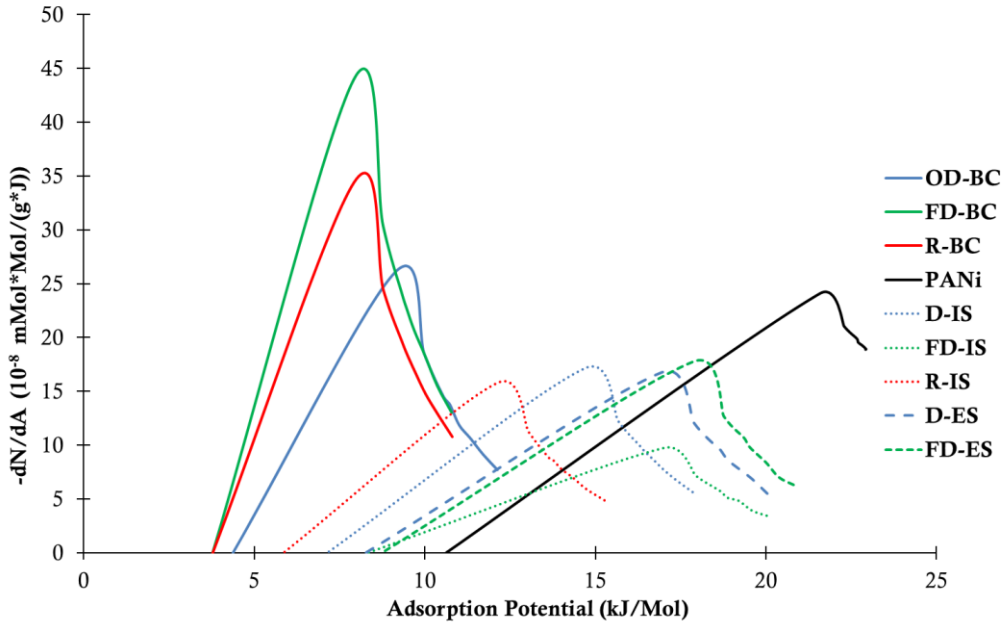

Figure 32 – Heterogeneity profile of *n*–octane from BC matrixes and BC/PANi nanocomposites at 25 °C OD–BC – oven dried BC; FD–BC – freeze dried BC; R–BC – regenerated BC; PANi – polyaniline; D–IS – drained BC/PANi *in situ* nanocomposite; FD–IS – freeze dried BC/PANi *in situ* nanocomposite; R–IS – regenerated BC/PANi nanocomposite; D–ES – drained BC/PANi *ex situ* nanocomposite; FD–ES – freeze dried BC/PANi *ex situ* nanocomposite.

Also, the increment of the specific surface energy (γ_s^{sp}) is supported by the increase in the adsorption potential maximum of ethanol and tetrahydrofuran, as observed in Figure 33. However, it is observed that the adsorption potential increases more significantly in ethanol (59.8–105.2%) when compared to tetrahydrofuran (24.2–61.5%), which indicates an increase in the basic surface nature in all nanocomposites. This indicates changes on the polar surface groups, which will be further explored with the evaluation of the specific free energy of adsorption (ΔG_s^{sp}).

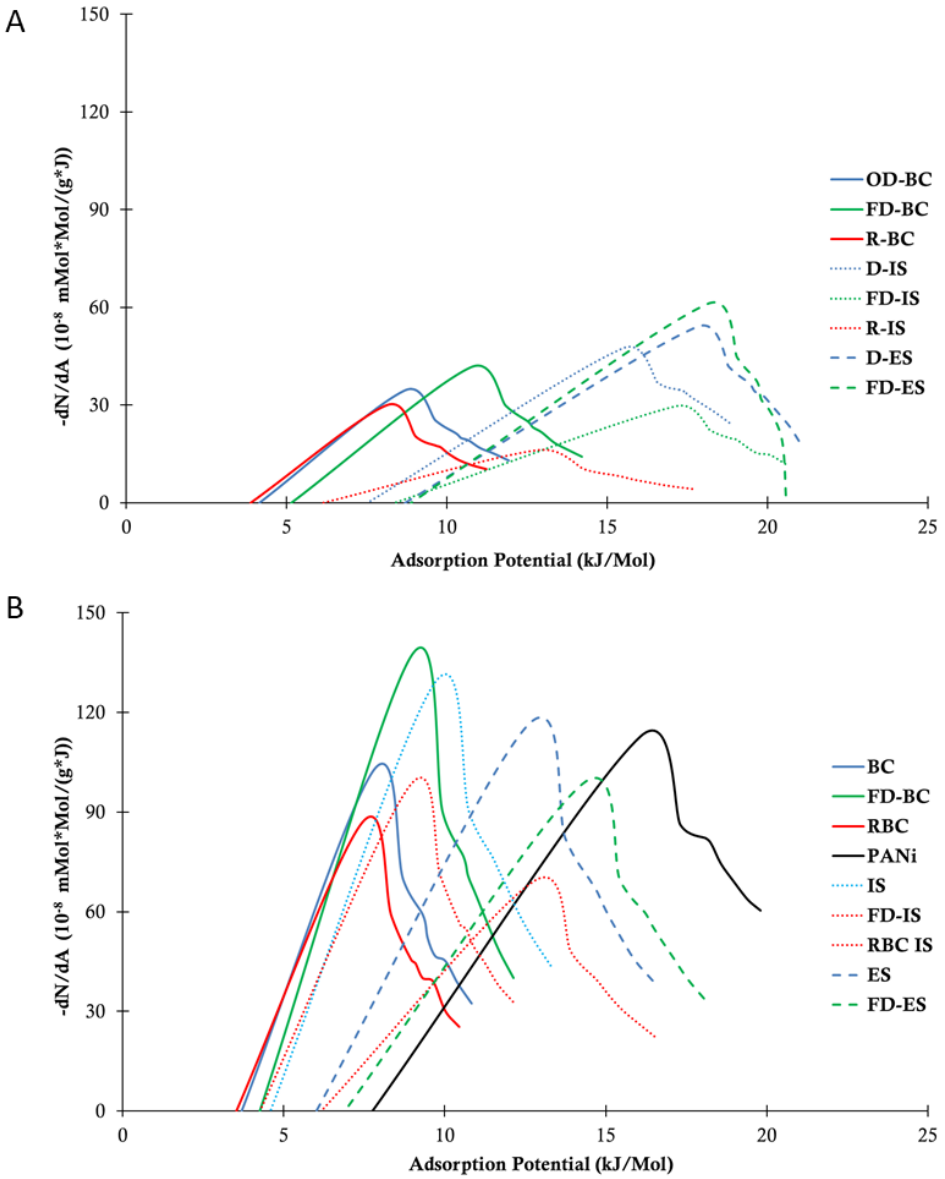

Figure 33 – Heterogeneity profile of ethanol (A) and tetrahydrofuran (B) from the BC/PANi nanocomposites at 25 ºC. BC – oven dried BC; FD–BC – freeze dried BC; R–BC – regenerated BC; PANi – polyaniline; D–IS – drained BC/PANi *in situ* nanocomposite; FD–IS – freeze dried BC/PANi *in situ* nanocomposite; R–IS – regenerated BC/PANi nanocomposite; D–ES – drained BC/PANi *ex situ* nanocomposite; FD–ES – freeze dried BC/PANi *ex situ* nanocomposite.

3.2.5.2 – Acid-base surface character

Through the incorporation of PANi in the BC matrix, the surface moiety was changed, as displayed by FTIR–ATR and EDX. Thus, the acid–base character of the surface

was evaluated through IGC. Concerning the specific free energy of adsorption, the data is shown in Figure 34. Considering the high ΔG_s^{sp} values of PANi, its coating onto the BC fibers should lead into stronger interactions with the polar probes. The different probes have different energies of interaction since each probe interacts differently with the active sites present at the surface. In general, to BC/PANi nanocomposites, there was an overall increase in the interactions with the polar probes, when compared to the BC matrixes, which indicates changes in the acid–base groups on the BC surface. When comparing the ΔG_s^{sp} values it is seen that higher values are obtained for both FD–BC/PANi nanocomposites. This result agrees with the γ_s^{sp} values, where it was higher for both FD–BC/PANi nanocomposites. With the polymerization of PANi on BC, the ΔG_s^{sp} of ethanol increases more significantly when compared to tetrahydrofuran (Table 11), suggesting an increase of the basic character at the surface of BC/PANi nanocomposites, due to the amine groups in PANi. Thus, through the evaluation of polar probes by IGC it was possible to confirm the presence of PANi in the nanocomposite surface.

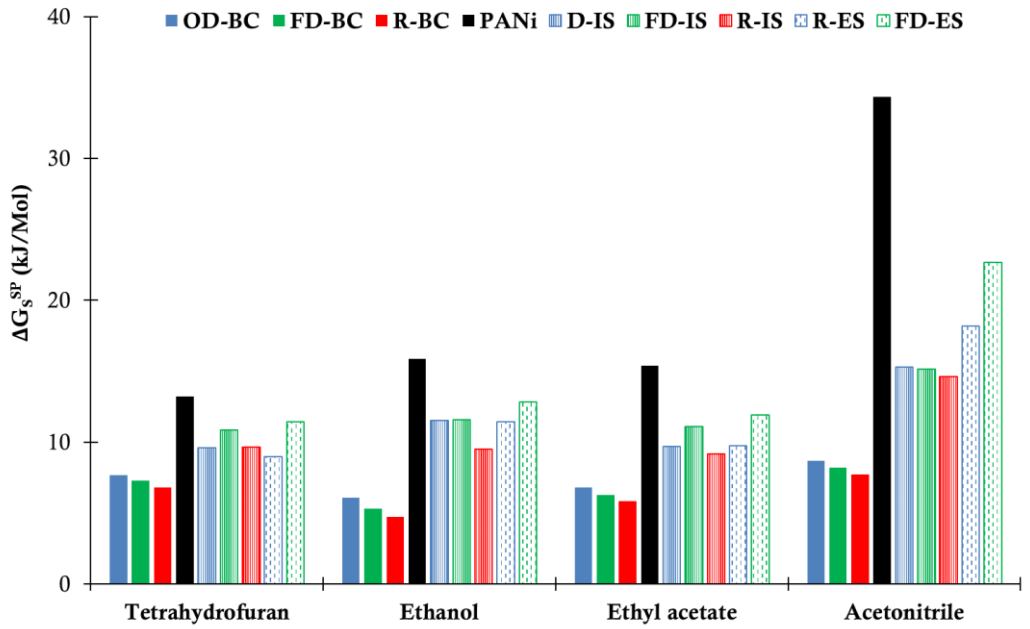

Figure 34 – Specific free energy of adsorption (ΔG_S^{SP}) of polar probes onto the BC/PANi nanocomposites at 25 °C BC – oven dried BC; FD–BC – freeze dried BC; R–BC – regenerated BC; PANi – polyaniline; D–IS – drained BC/PANi *in situ* nanocomposite; FD–IS – freeze dried BC/PANi *in situ* nanocomposite; R–IS – regenerated BC/PANi nanocomposite; D–ES – drained BC/PANi *ex situ* nanocomposite; FD–ES – freeze dried BC/PANi *ex situ* nanocomposite.

The *Kb*/*Ka* ratio of the BC matrixes shows an acidic character (0.57 to 0.75) due to the hydroxyl groups at the surface. For PANi powder a basic character is observed (Table 11), which results from the presence of amine groups throughout the polymer chains. With the introduction of PANi in the BC matrixes, the BC acidic behaviour is shifted into a basic behaviour (*Kb*/*Ka* ranging from 1.88 to 3.77), corroborating the fact that the polymer can be found at the surface. Also, the percentage of N and O, presented in Table 7, gives an indication of the relative basicity of the BC/PANi nanocomposites. The percentage of N is associated with the amine groups of PANi whereas the percentage of O is associated to the hydroxyl and ether groups of cellulose. When compared to the *Kb*/*Ka* values (Table 11), it is seen that the presence of N and lower O values is associated with higher *Kb*/*Ka* values.

The *Kb*/*Ka* values are too dispersed which means that there is no correlation with the polymerization method nor the BC matrix employed with the acid–base surface properties.

3.2.5.3 – Surface nanomorphology

IGC was also employed to evaluate the surface nanomorphology and the influence of the BC matrix and polymerization method used in the BC/PANi nanocomposite synthesis. With the incorporation of PANi, the BC S_{BET} is drastically reduced (64–85%). This decrease is probably due that during chemical polymerization, PANi incorporates on the fibers (higher widths) and pores are obstructed, which not only decrease the area available for probes to access (thus decreasing the S_{BET}) but also makes harder for probes to cross the sample (lower *Dp*, (Table 12)). Through SEM it is observed that the surface becomes more compact (Figure 27), corroborating the IGC results. This way, through S_{BET} and *Dp* analysis from IGC it is possible to obtain information regarding the pore availability.

The S_{BET} have no direct correlation with the polymerization method nor with BC matrix used for the synthesis of BC/PANi nanocomposites. On the other hand, the *Dp* values of D–IS and FD–IS BC/PANi nanocomposites are higher than the values obtained in D–ES and FD–ES BC/PANi nanocomposites, respectively. Thus, IGC evidences that the diffusion of the probes is influenced by the polymerization method applied, which indicates differences on the structure of the different nanocomposites. R–IS BC/PANi nanocomposite presented

the highest S_{BET} and lowest *Dp* value, which differentiates from the remaining nanocomposites. The low *Dp* value can be due to the compact structure of R–BC whereas the high S_{BET} value can be due to the surface roughness as seen through AFM.

Table 12 – Surface area (S_{BET}), diffusion parameter (*Dp*) and morphology indexes from the BC matrixes and BC/PANi nanocomposites at 25 ºC.

	S_{BET} (m^2/g)	*Dp* (cm^2/min)	Morphology index		
			2,2,4–trimethylpentane	2,5–dimethylhexane	cyclooctane
OD–BC	4.59[a]	58.10[a]	0.12[a]	0.66[a]	1.92[a]
FD–BC	7.05[b]	76.78[b]	0.57[b]	0.69[a]	2.24[b]
R–BC	3.55[c]	12.9[c]	0.60[b]	0.65[a]	2.16[b]
D–IS	1.61[a]	4.04[a]	0.60[a]	0.64[a]	0.84[a]
FD–IS	1.07[b]	0.13[b]	0.63[a]	0.71[b]	0.60[b]
R–IS	2.03[c]	0.02[b]	0.90[b]	0.88[c]	2.00[c]
D–ES	1.52[a]	0.64[c]	0.43[c]	0.55[d]	0.62[d]
FD–ES	2.04[c]	0.08[b]	0.47[c]	0.63[a]	0.53[b]

Values in same column not sharing a common superscript are statistically different ($p < 0.05$). The error of the measurements was determined to be 3% and as such the upper and lower values from the average were determined; OD–BC – oven dried BC; FD–BC – freeze dried BC; R–BC – regenerated BC; D–IS – drained BC/PANi *in situ* nanocomposite; FD–IS – freeze dried BC/PANi *in situ* nanocomposite; R–IS – regenerated BC/PANi nanocomposite D–ES – drained BC/PANi *ex situ* nanocomposite; FD–ES – freeze dried BC/PANi *ex situ* nanocomposite.

The morphology index of the BC/PANi nanocomposites was assessed observing on most probes a steric hindrance phenomena (morphology index < 1) (Table 12). Through Tukey's post hoc analysis, the data obtained by 2,2,4–trimethylpentane fall into three groups: *ex situ* composites, *in situ* composites and R–IS BC/PANi nanocomposite. This indicates that this probe did not detect changes in the pore availability using different BC matrixes but it was influenced by the polymerization method used. For 2,5–dimethylhexane the results are dispersed which means that this probe did not evidenced differences in the pore availability of the nanocomposites by employing different polymerization methods or different BC matrixes. When comparing to the BC matrixes, the morphology index obtained by cyclooctane shows that the pore availability decreases in the nanocomposites since it shifts from an adsorption (BC matrixes) to a steric hindrance (BC/PANi nanocomposites) behaviour. This observation agrees with the S_{BET} and *Dp* results (Table 12), since blocking the

BC pores results in a more compact surface, leading into lower S_{BET} values. The cyclooctane morphology indexes obtained for D–IS and FD–IS BC/PANi nanocomposites are slightly higher than the ones obtained in D–ES and FD–ES BC/PANi nanocomposites. Also, *in situ* nanocomposites (D–IS and FD–IS) present higher morphology indexes in comparison to *ex situ* nanocomposites (D–ES and FD–ES). Thus, cyclooctane evidenced differences in the surface availability using different polymerization methods and BC matrixes.

Through AFM it was observed that the BC/PANi nanocomposites are rougher than the BC matrixes (Figure 28), which explains the steric hindrance observed for cyclooctane. R–IS BC/PANi nanocomposite depicted the highest surface roughness of all nanocomposites which interestingly presented an adsorption behaviour for cyclooctane (morphology index >1). This indicates that the surface topography of the sample contributed to the adsorption of the probe, as also seen through S_{BET} measurement.

Thus, through IGC it was possible to observe an increase of the steric hindrance through the morphology index of cyclooctane, which is correlated with the incorporation of PANi on the surface. Moreover, this result corroborates the *Rq* values obtained through AFM, where a rougher surface is obtained. R–IS was the only nanocomposite who presented an adsorption phenomenon for cyclooctane which could mean that the surface topography was favourable for the adsorption of the probe. It was also evidenced differences in the surface morphology through the use of different polymerization methods (*in situ* and *ex situ* polymerization) as also through the use of different BC matrixes.

3.3 – Application of BC/PANi nanocomposites for potential drug delivery system

The development of novel electrical responsive membranes for drug delivery are of great interest, which could offer promising new treatments, as a transdermal patch, for chronic diseases that require daily injections of daily dosages of medication. The synthesis of BC/PANi nanocomposites offers a simple pathway to obtain an electro-responsive nanocomposite. This chapter aims to study which of the BC modifications previously made are the most suited for an efficient drug delivery system through electrical stimulus.

Due to the unique properties of PANi, for an effective drug delivery system, only charged and small drugs should be used (141). Sulfacetamide was chosen for this study, due to its antibacterial properties and negative charge. This compound acts as a competitor with *p*–aminobenzoic acid, which is an essential component of the bacterial growth (142). It is commonly used topically, against acne rosacea and seborrheic dermatitis (142).

3.3.1 – Work of adhesion and drug loading

The interaction of the drug with the BC matrixes and BC/PANi nanocomposites was studied through both W_{adh} and W_{coh} determined by IGC. The W_{adh} corresponds to the interactions between the drug and the membranes while the W_{coh} corresponds to the interactions established inside of the membrane. A higher W_{adh}/W_{coh} ratio indicates a higher interaction of the drug with the membrane. Moreover, the interfacial interactions were compared to the amount of drug absorbed (Table 13). In case of the BC matrixes, the ratio presented is close to 1 which indicates good dispersibility of sodium sulfacetamide in BC. For the BC/PANi nanocomposites, both W_{adh} and W_{coh} increased, more significantly in the last. This way the resulting ratio decreases, which indicates that the interactions between polyaniline chains found in the surface are stronger than the interactions between the nanocomposite surface and the drug. Based on this result it is estimated a lower dispersibility of the drug in the nanocomposite when they are compared to the BC matrixes. The same

analogy was made by Strzemiecka et al. when it evaluated the interactions between polyurethane and carbon black through IGC (99).

Table 13 – Work of adhesion (W_{adh}), work of cohesion (W_{coh}) and drug content (%) on BC matrixes and BC/PANi nanocomposites at 25 ºC.

	W_{adh} (mJ/m^2)	W_{coh} (mJ/m^2)	W_{adh}/W_{coh}	Drug content (%)
OD–BC	215.08	225.86	0.95	15.7 ± 1.0
FD–BC	204.31	203.80	1.00	75.9 ± 2.3
R–BC	193.57	183.18	1.06	7.2 ± 1.4
D–IS	284.64	393.52	0.72	5.4 ± 0.3
FD–IS	316.68	490.34	0.65	5.9 ± 0.3
R–IS	330.03	527.46	0.63	1.8 ± 0.1
D–ES	284.15	390.39	0.73	3.2 ± 1.1
FD–ES	302.54	428.29	0.71	3.8 ± 0.7

OD–BC – oven dried BC; FD–BC – freeze dried BC; R–BC – regenerated BC; D–IS – drained BC/PANi *in situ* nanocomposite; FD–IS – freeze dried BC/PANi *in situ* nanocomposite; R–IS – regenerated BC/PANi nanocomposite; D–ES – drained BC/PANi *ex situ* nanocomposite; FD–ES – freeze dried BC/PANi *ex situ* nanocomposite.

When comparing the drug content of each sample it is possible to observe that *(i)* BC matrixes absorbed higher amounts of drug than the nanocomposites and *(ii)* the freeze dried samples absorbed more than the drained–BC samples, followed by the regenerated samples. Regarding the observations done, BC matrixes presented a higher drug content probably due to a higher surface area (S_{BET}), as observed by IGC. This way, it is possible to conclude that the drug loading capacity of the nanocomposites is affected by the BC matrix employed for the synthesis of BC/PANi nanocomposites. Moreover, with the incorporation of PANi it was observed that the pores were obstructed and as such it is expected a lower ability to absorb the drug.

3.3.2 – Antimicrobial activity

The growth dynamic of *E. coli* was evaluated by measuring the optical density at 600 nm over time, in both unmodified and drug loaded membranes (Figure 35). Drug loaded samples are represented with the suffix (D) whereas unmodified samples are presented with no suffix. The control consists in the growth of *E. coli* in the absence of any membrane. The

antimicrobial activity of *ex situ* nanocomposites and regenerated BC/PANi nanocomposite were not evaluated due to the low drug loading contents. Figure 35 shows that in the first 2 h, there was no significant increase in the growth of *E. coli*, which corresponds to the lag phase, where the cells are adjusting to the new growth conditions. Followed by the lag phase, *E. coli* presented a fast growth, corresponding to the log phase. Until 10 h, in all samples, there are no significant differences when comparing to the control, which means that both unmodified and drug loaded membranes did not influenced the growth at this stage.

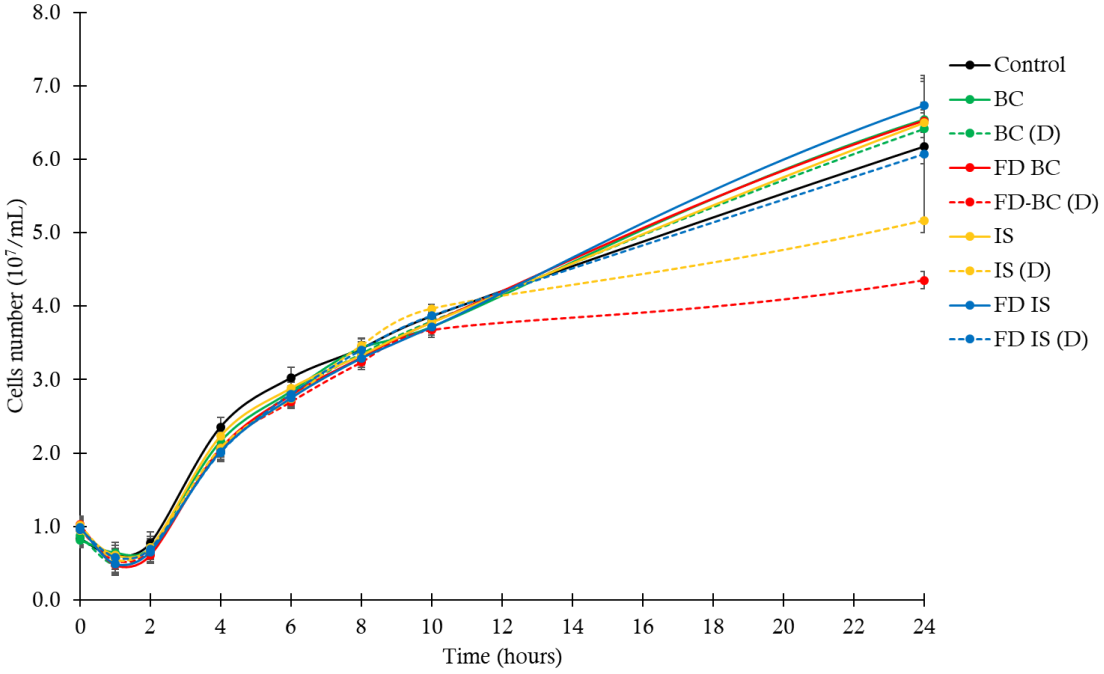

Figure 35 – Antimicrobial activity of the membranes determined through the optical density method at 600 nm. Unloaded membrane – no suffix; drug loaded membrane – (D); OD–BC – oven dried BC; FD–BC – freeze dried BC; R–BC – regenerated BC; D–IS – drained BC/PANi *in situ* nanocomposite; FD–IS – freeze dried BC/PANi *in situ* nanocomposite; R–IS – regenerated BC/PANi nanocomposite; ES – drained BC/PANi *ex situ* nanocomposite; FD–ES – freeze dried BC/PANi *ex situ* nanocomposite.

After 24 h, a decrease in the bacterial growth is seen on both drug loaded FD–BC and D–IS BC/PANi nanocomposite membranes, when compared to the control, indicating that the membranes released their drug content, depicted by a decrease in the maximum cells density (Figure 36). FD–BC membrane presents the highest drug loading capacity when

compared to the remaining samples, which means that a higher amount of drug can be effectively released onto the growth media and interact with the bacteria. Taking in consideration the time needed to observe an inhibition onto *E. coli* growth, the membranes present a slow diffusion of the drug onto the media. In the remaining drug loaded samples there was no inhibition in the bacterial growth which suggests that the following hypothesis might have occurred: *(i)* the drug loaded in the membranes was not released *(ii)* the lethal dose of the drug is higher than the one loaded and fully released by the membranes and/or *(iii)* the drug was partially released in amounts lower than the lethal dose.

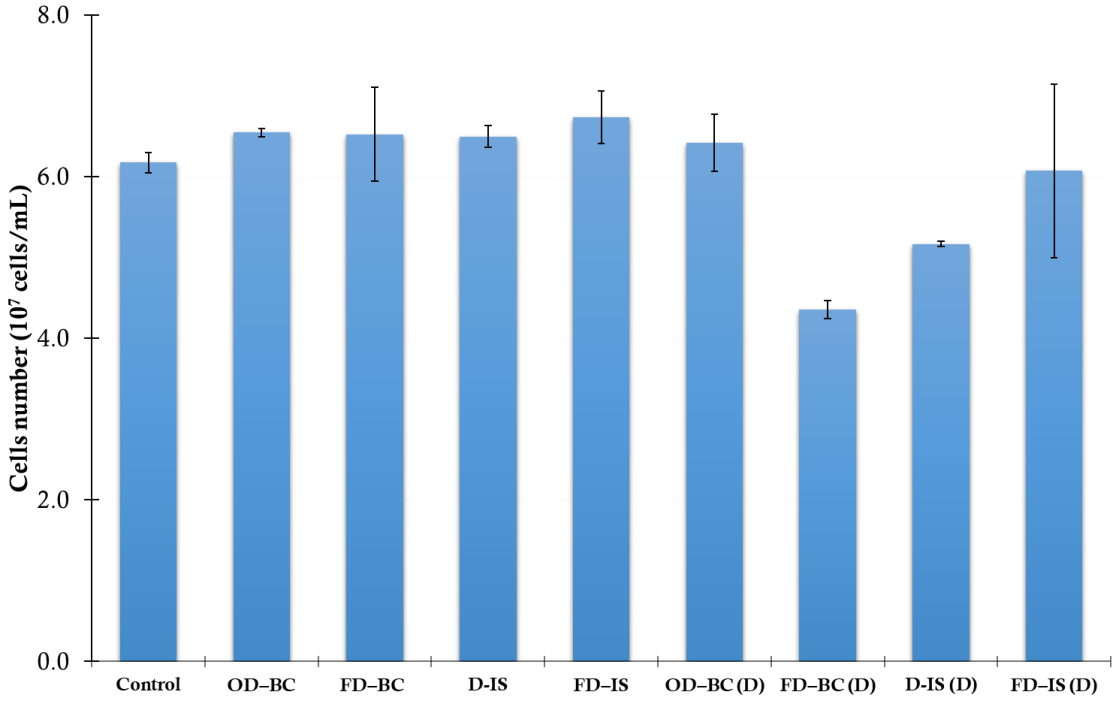

Figure 36 – Cells number of *E. coli* after 24 h of contact time with the membranes under analysis.

Drug loaded drained *in situ* BC/PANi (D–IS (D)) was the only nanocomposite that presented an inhibitory effect on *E. coli*. Also, it presented the highest electrical conductivity. Thus, this membrane will be the nanocomposite chosen for the antimicrobial activity through electrical stimulus to release the drug. On Figure 37 it is observed that the *E. coli* grown in the presence of the drug loaded membrane submitted to electrical stimulus (shock D–IS (D)) presents a lower cells number in comparison to both the control and to D–IS (D).

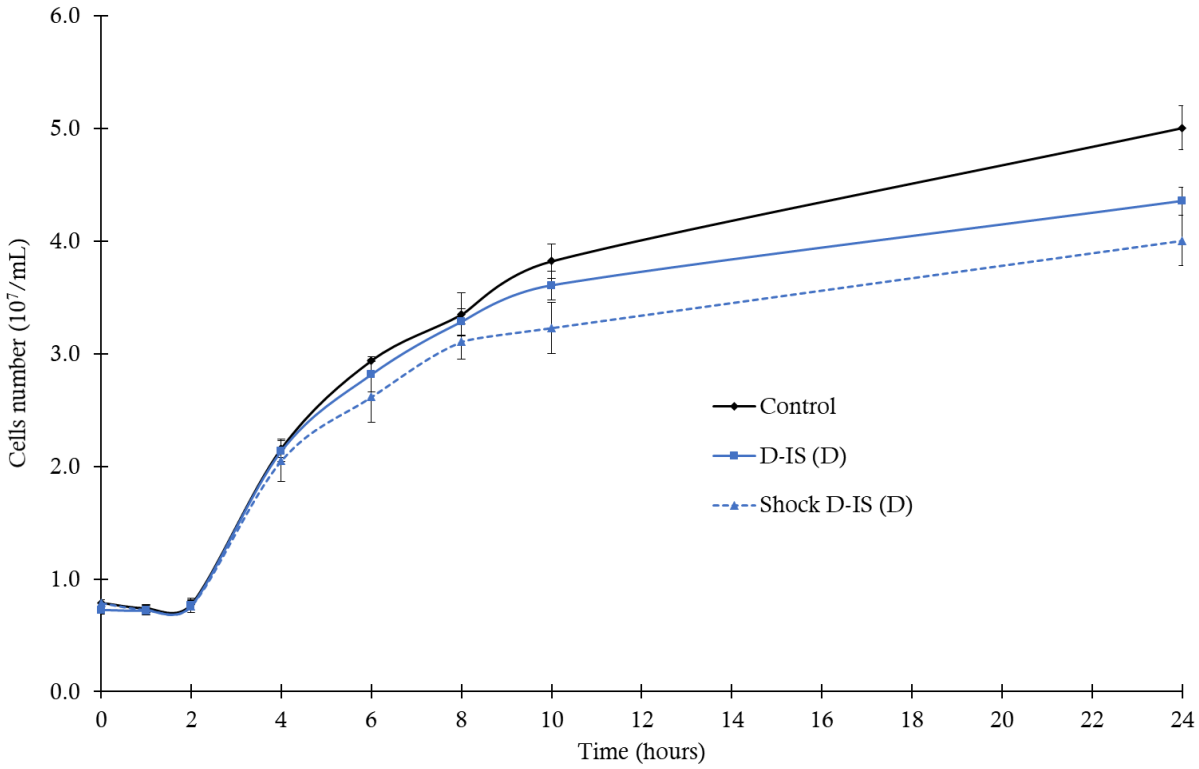

Figure 37 - Antimicrobial activity of the membranes determined through the optical density method. Control – *E.coli* grown without the presence of membrane; D–IS (D) – drug loaded drained BC/PANi *in situ* nanocomposite; Shock D–IS (D) - drug loaded drained BC/PANi *in situ* nanocomposite submitted to electrical stimulus.

The drug loaded nanocomposite without electrical stimulus (D–IS (D)) presented a lower growth inhibition on *E. coli* (13%) when compared to the drug loaded nanocomposite submitted to electrical stimulus (shock D–IS (D), 20%). Slight differences between the two membranes start at 4 hours after exposure, being accentuated over time. This preliminary test shows promising results regarding the use of drug loaded BC/PANi nanocomposites for drug release applications. Nevertheless, the current experiment was not optimized, needing further tests. Some parameters that should be taken into consideration during the optimization are the drug incorporation efficiency (using different drug concentration solutions) and the voltage applied onto the membrane. The current test was an indirect method to observe the release of the drug. Thus, a more suitable method for the direct quantification of the drug released should be considered, such as the determination through UV-Vis.

Chapter IV – Conclusion

The current work aims to determine the most suitable method for BC/PANi synthesis for drug delivery applications through electrical stimulus. The present research shows that the BC/PANi nanocomposites were successfully synthesized using different BC matrixes (drained, freeze dried and regenerated), as well as through different polymerization methods (*in situ* and *ex situ*). The electrical conductivities obtained varied between $1.48x10^{-3}$ to $1.39x10^{-1}$ S/cm, which fall within the range of semiconductive materials.

The BC/PANi nanocomposites were submitted through a series of analysis to evaluate the influence of the different BC modification methods in the physico-chemical properties of the resulting material. FTIR–ATR and EDX evidenced a successful coating of PANI on BC fibers, being visible through SEM. The thermal stability of the different nanocomposites decreased in comparison to the original BC matrix, which could be correlated to the loss of the crystallinity content of BC during the modification. In this regard, the crystallinity of the freeze dried BC/PANi nanocomposites were less affected than the drained BC/PANi nanocomposites.

Inverse gas chromatography (IGC) has proven to be a valuable technique in the evaluation of the changes occurred with PANi incorporation into BC. It is observed a significant increase in the surface energy of the nanocomposites, as well as a shift from an acidic surface (BC matrixes) to a basic surface (BC/PANi nanocomposites). Moreover, changes in the BC structure due to the different modification methods was observed, where the different BC/PANi nanocomposites presented a more compact (lower S_{BET} and lower Dp) and rougher surface. Thus, the current work evidence the influence of the different BC treatments in the properties of the resulting nanocomposite.

Through the antimicrobial activity tests, drug loaded drained BC/PANi *in situ* nanocomposite was the only BC modification that successfully presented an inhibitory growth on *E. coli* (up to 13%) without electrical stimulus. With the electrical stimulus, the inhibitory growth was further increased (up to 20%). Further investigation needs to be done, namely in the optimization of the drug loading efficiency, as well as the employment of different voltages. Also, the drug release kinetics should be studied, with the aim to understand the dynamic process of drug release.

References

1. Moon R, *et al.* Cellulose nanomaterials review: structure, properties and nanocomposites. Chem Society Reviews. 2011;40:3941-3994.

2. Esa F, *et al.* Overview of Bacterial Cellulose Production and Application. Agriculture and Agricultural Science Procedia. 2014;2:113-119.

3. Sulaeva I, *et al.* Bacterial cellulose as a material for wound treatment: Properties and modifications. A review. Biotechnol Advances. 2015;33(8):1547-1571.

4. Miao C, Hamad W. Cellulose reinforced polymer composites and nanocomposites: a critical review. Cellulose. 2013;20:2221-2262.

5. Chawla P, *et al.* Microbial cellulose: fermentative production and applications. Food Technology and Biotechnology. 2009;47:107-124.

6. Wang S, *et al.* Blood compatibility of oxidized bacterial cellulose/silk fibroin composite membrane. In: Chung S. LX, editor. Proceedings of 2014 International conference on materials science and energy engeneering. 1st Edition ed. Singapore: World Scientific Publishing; 2015. p. 700.

7. Isogai A, *et al.* Solid-state CP/MAS ^{13}C NMR study of cellulose polymorphs. Macromolecules. 1989;22:3168-3172.

8. Poletto M, *et al.* Structural characteristics and thermal properties of native cellulose. In: Ven T. GL, editor. Cellulose - fundamental aspects. 1: InTech; 2013.

9. Nishiyama Y, *et al.* Crystal structure and hydrogen bonding system in cellulose I from synchrotron X-ray and neutron fiber diffraction. Journal of American Chemical Society. 2003;125:14300-14306.

10. Maurer R, *et al.* Molecular simulation of surface reorganization and wetting in crystalline cellulose I and II. Cellulose. 2013;20:25-42.

11. Brown A. On an acetic ferment which forms cellulose. Journal of the Chemical Society. 1886;49:432-439.

12. Ji K, *et al.* Bacterial cellulose synthesis mechanism of facultative anaerobe enterobacter sp. FY-07. Scientific Reports. 2016;6(21863).

13. Berg J, *et al.* Glycolysis and Gluconeogenesis. Biochemistry. 5th Edition ed: Freeman W.; 2002.

14. Ross P, *et al.* Cellulose biosynthesis and function in bacteria. Microbiological reviews. 1991;55:35-58.

15. Keshk S, Samshima K. Evaluation of different carbon sources for bacterial cellulose production. African Journal of Biotechnology. 2005;4:478-482.

16. Rajwade J, *et al.* Applications of bacterial cellulose and its composites in biomedicine. Applied microbiology and biotechnology. 2015;99(6):2491-2511.

17. Keshk S. Bacterial cellulose production and its industrial applications. Bioprocessing & Biotechniques. 2014;4:1-10.

18. Mohite B, Patil S. A novel biomaterial: bacterial cellulose & its new era applications. Biotechnology and Applied Biochemistry. 2014;61:101-110.

19. Brown R. Bacterial cellulose. In: Kennedy PW, editor. Cellulose: structural and functional aspects: Ellis Horwood Ltd.; 1989. p. 145-151.

20. Stephens R, *et al.*, inventors; Weyerhaeuser Company, Tacoma assignee. Method of using bacterial cellulose as a dietary fiber component. United States of America1990.

21. Fontana J, *et al.* Acetobacter cellulose pellicle as a temporary skin substitute. Applied Biochemistry and Biotechnology 1990;24:253-264.

22. Iguchi M*, et al.* Review bacterial cellulose - a masterpiece of nature's arts. Journal of Materials Science. 2000;35:261-270.

23. Shi Z*, et al. In situ* nano-assembly of bacterial cellulose-polyaniline composites. RSC Advances. 2011;2:1040-1046.

24. Olsson C, Westman G. Direct dissolution of cellulose: background, means and applications. In: Ven T. GL, editor. Cellulose - fundamental aspects: Intech; 2003. p. 143-178.

25. Mittal V. Synthesis techniques for polymer nanocomposites Wiley-VCH; 2015. 314 p.

26. Hu W*, et al.* Flexible electrically conductive nanocomposite membrane based on bacterial cellulose and polyaniline. The Journal of Physical Chemistry B. 2011;115:8453-8457.

27. Wang H*, et al.* Bacterial cellulose nanofiber-supported polyaniline nanocomposites with flake-shaped morphology as supercacitor electrodes. Journal of Physical Chemistry. 2012;116:13013-13019.

28. Lee B*, et al.* Polymerization of aniline on bacterial cellulose and characterization of bacterial cellulose/polyaniline nanocomposite films. Current Applied Physics. 2012;12:75-80.

29. Park M*, et al.* Electromagnetic nanocomposite of bacterial cellulose using magnetite nanoclusters and polyaniline. Colloids and Surfaces B: Biointerfaces. 2013;12:238-242.

30. Ray D, Sain S. *In situ* processing of cellulose nanocomposites. Composites: Part A. 2016;83:19-37.

31. Pa'e N*, et al.* Effect of different drying methods on the morphology, crystallinity, swelling ability and tensile properties of *Nata de coco*. Sains Malaysiana. 2014;5:767-773.

32. Zhang C*, et al.* Effect of drying methods on structure and mechanical properties of bacterial cellulose films. Advanced Materials Research. 2011;239-242:2667-2670.

33. Clasen C*, et al.* Effects of different drying processes on the material properties of bacterial cellulose membranes. Macromolecules Symposium. 2006;244:48-58.

34. Lima G*, et al.* Characterization of the bacterial cellulose dissolved on dimethylacetamide/lithium chloride. 10º Congresso Brasileiro de polímeros; Foz de Iguaçu2009.

35. Lindman B*, et al.* On the mechanism of dissolution of cellulose. Journal of Molecular Liquids. 2010;156:76-81.

36. Wang S*, et al.* Recent advances in regenerated cellulose materials. Progress in Polymer Science. 2015;53:169-206.

37. Kimura M*, et al.* Versatile molding process for though cellulose hydrogel materials. Scientific Reports. 2015;5.

38. Liebert T. Cellulose Solvents – Remarkable History, Bright Future. Cellulose Solvents: For Analysis, Shaping and Chemical Modification. ACS Symposium Series. 1033: American Chemical Society; 2010. p. 3-54.

39. Painter P, Coleman M. Essentials of polymer science and engeneering: DEStech Publications; 2009.

40. Pandeym M*, et al.* Dissolution study of bacterial cellulose (nata de coco) from local food industry: solubility behavior & structural changes. International Journal of Pharmacy and Pharmaceutical Sciences. 2014;6:89-93.

41. Shen X*, et al.* Solubility of a high molecular-weight bacterial cellulose in lithium chloride/N,N-dimethylacetamide solution. Journal of Macromolecular Science, Part B. 2010;49:1012-1018.

42. Klemm D*, et al.* Comprehensive cellulose chemistry Wiley-VCH, editor1998. 260 p.

43. Zhang H*, et al.* Synthesis and characterization of quaternized bacterial cellulose prepared in homogeneous aqueous solution. Carbohydrate Polymers. 2016;136:171-176.

44. Shanshan G*, et al.* Preparation of cellulose films from solution of bacterial cellulose in NMMO. Carbohydrate Polymers. 2012;87:1020-1025.

45. Isik M*, et al.* Ionic liquids and cellulose: dissolution, chemical modification and preparation of new cellulosic materials. International Journal of Molecular Sciences. 2014;15:11922-11940.

46. Morgenstern B, Berger W. Investigations about dissolution of cellulose in the LiCl/N,N-dimethylformamide system. Acta Polymerica. 1993;44:100-102.

47. McCormick, inventorNovel cellulose solutions. United States Patent1981.

48. Zhang C*, et al.* Dissolution mechanism of cellulose in N,N-dimethylacetamide/lithium chloride: revising through molecular interactions. The Journal of Physical Chemistry B. 2014;118:9507-9514.

49. Li C*, et al.* Fabrication and characterization of electrospun nanofibers of high DP natural cooton lines cellulose. Fibers and polymers. 2011;21:345-351.

50. Frenot A*, et al.* Electrospinning of cellulose-based nanofibers. Journal of Applied Polymer Science. 2007;103:1473-1482.

51. Frey M. Electrospinning cellulose and cellulose derivatives. Polymer Reviews. 2008;48:378-391.

52. Costa L*, et al.* Nanopores structure in electrospun bacterial cellulose. Journal of Biomaterials and Nanobiotechnology. 2012;3:92-96.

53. Kim C*, et al.* Preparation of submicron-scale, electrospun cellulose fibers via direct dissolution. Journal of Polymer Science. 2005;43:1673-1683.

54. Vernitskaya T, Efimov O. Polypyrrole: a conducting polymer; its synthesis, properties and applications. Russian Chemical Reviews. 1997;66:443-457.

55. Molapo K*, et al.* Eelectronics of conjugated polymers (I): Polyaniline. International Journal of Electrochemical Science. 2012;7:11859-11875.

56. Shirakawa H*, et al.* Synthesis of electrically conducting organic polymers: halogen derivatives of polyacetilene (CH)x. Journal of the Chemical Society, Chemical Communications. 1977:578-580.

57. Sapurina I, Shishov M. Oxidative Polymerization of Aniline: Molecular Synthesis of Polyaniline and the Formation of Supramolecular Structures. In: Gomes AdS, editor. New polymers for special applications: InTech; 2012.

58. Kaur G*, et al.* Electrically conductive polymers and composites for biomedical applications. Royal Society of Chemistry Advances. 2015;5:37553-37567.

59. Catedral M*, et al.* Effect of dopant ions on the electrical condutivity and microstructure of polyaniline (emeraldine salt). Science Diliman. 2004;16:41-46.

60. Kuhn S. Synthesis of electrically conductive polypyrrole thin films via ammonium persulfate chemistry: Massashusetts Institute of Technology; 1990.

61. Hassan S*, et al.* A.C. Electrical condutivity for polyaniline prepared in different acidic medium. International Journal of Basic and Applied Science. 2012;1:352-362.

62. Smith J. Intrisically electrically conducting polymers: synthesis, characterization and their applications Progress in Polymer Science. 1998;23:57-59.

63. Ansari R. Polypyrrole conducting electroactive polymers: synthesis and stability studies. E-Journal of Chemistry. 2006;3:186-201.

64. Sapurina I, Stejskal J. The mechanism of the oxidative polymerization of aniline and the formation of supramolecular polyaniline structures. Polymer International. 2008;57:1295-1325.

65. Hand R, Nelson R. The anodic decomposition pathways of ortho- and meta-substituted anilines. Journal of Electrochemical Society. 1978;125:1059-1069.

66. Lee H*, et al.* Fabrication and evaluation of bacterial cellulose-polyaniline composites by interfacial polymerization. Cellulose. 2012;19:1251-1258.

67. Marins J*, et al.* Structure and properties of conducting bacterial cellulose-polyaniline nanocomposites. Cellulose. 2011;18:1285-1294.

68. Zhang D*, et al.* Nanocomposites of polyaniline and cellulose nanocrystals prepared in lyotropic chiral nematic liquid crystals. Journal of Materials. 2013;2013:1-6.

69. Mittal V. Characterization techniques for polymer nanocomposites. 1st Edition ed: Wiley-VCH; 2012. 378 p.

70. Missoum K*, et al.* Nanofibrillated cellulose surface modification: a review. Materials. 2013;6:1745-1766.

71. Voelkel A*, et al.* Inverse gas chromatography as a source of physiochemical data. Journal of Chromatography A. 2009;1216:1551-1566.

72. Thielmann F. Introduction into the characterization of porous materials by inverse gas chromatography. Journal of Chromatography A. 2004;1037:115-123.

73. Voelkel A. Inverse gas chromatography in characterization of surface. Chemometrics and intelligent laboratory systems. 2004;72:205-207.

74. Conder J. Physicochemical measurements: gas chromatography. In: M. C, editor. Encyclopedia of separation science. Detroit, USA: Academic Press; 2000.

75. Grimsey I*, et al.* Analysis of the surface energy of pharmaceutical powders by inverse gas chromatography. Journal of Pharmaceutical Sciences. 2002;91:571-583.

76. Chan H, Doelker E. Polymorphic transformation of some drugs under compression. Drug Development and Industrial Pharmacy. 1985;11:315-332.

77. Al-Saigh Z. Review: inverse gas chromatography for the characterization of polymer blends. International Journal of Polymer Analysis Characterization. 1997;3:249-291.

78. Rückriem M*, et al.* Inverse gas chromatography for determining the dispersive surface energy of porous silica. Colloids and Surfaces A: Physicochemical and Engeneering Aspects. 2010;357:21-26.

79. Mukhopadhyay P, Schreiber H. Aspects of acid-base interactions and use of inverse gas chromatography. Colloids and Surfaces A: Physicochemical and Engeneering Aspects. 1995;100:47-71.

80. Sen A. Inverse gas chromatography. India: Defense Scientific Information & Documentation Centre; 2005.

81. Mohammadi-Jam S, Waters K. Inverse gas chromatography applications: a review. Advances in Colloid and Interface Science. 2014;212:21-44.

82. James A, Martin J. Gas-Liquid partition chromatography: the separation and micro-estimation of volatile fatty acids from formic acid to dodecanoic acid. Biochemical Journal. 1952;50:679-690.

83. Domínguez J, Díez-Masa J. Retention parameters in Chromatography. Pure and Applied Chemistry. 2001;73:969-992.

84. Kurganov A. A mass-balanced definition of corrected retention volume in gas chromatography. Journal of Chromatography A. 2007;1150:100-104.

85. Fowkes F. Attractive forces at interfaces. Industrial & Engineering Chemistry. 1964;56:40-52.

86. Schultz J*, et al.* The role of the interface in carbon-fibre epoxy composites. Journal of Adhesion. 1987;23:45-60.

87. Oss V. Interfacial Lifshitz-van der Waals and polar interactions in macroscopic system. Chemical Reviews. 1988;88:927-941.

88. Goss K. Considerations about the adsorption of organic moelcules from the gas phase to surfaces: implication for inverse gas chromatography and the prediction of adsorption coefficients. Journal of Colloid and Interface Science. 1997;190:241-249.

89. Gutmann V. The donor-acceptor approach to molecular interactions. New York, U.S.A.: Springer; 1978.

90. Riddle F, Fowkes F. Spectral shifts in acid-base chemistry. 1 - Van der Waals contributions to acceptor numbers. Journal of the American Society. 1990;112:3259-3264.

91. Brendlé E, Papirer E. A new topological index for molecular probes used in inverse gas chromatography for the surface nanorugosity evaluation. Journal of Colloid and Interface Science. 1997;194:207-216.

92. Calvet R*, et al.* Study of the interaction of polybutadiene/fillers using inverse gas chromatography. Journal of Chromatography A. 2012;1253:164-170.

93. Walton K, Snurr R. Applicability of the BET method for determining surface areas of microporous metal-organic frameworks. Journal of American Chemical Society. 2007;129:8552-8556.

94. Balard H. Estimation of the surface energetic heterogeneity of a solid by inverse gas chromatography. Langmuir. 1997;13:1260-1269.

95. Ghazali M, Nawawi M. Diffusion coefficient estimations by thin-channel column inverse gas chromatography: preliminary experiments. Pertanika Journal of Science and Technology. 2000;8:1-18.

96. Jackson P, Huglin M. Use of inverse gas chromatography to measure diffusion coefficients in crosslinked polymers at different temperatures. European Polymer Journal 1995;31:63-65.

97. Buckley D. Adhesion. In: Elsevier, editor. Surface effects in adhesion, friction, wear and lubrication. 5. New York, USA: Elsevier Science; 1981. p. 245.

98. Shanahan M, Possart W. Handbook of Adhesion Technology: Springer; 2011.

99. Strzemiecka B*, et al.* Estimation of polyurethane-carbon black interactions by means of inverse gas chromatography. Journal of Chromatography A. 2013;1314:249-254.

100. Pourramezan G*, et al.* Optimization of culture conditions for bacterial cellulose production by *Acetobacter sp.* 4B-2. Biotechnology. 2009;8:150-154.

101. Figueiredo A*, et al.* Biocompatible bacterial Cellulose-poly(2-hydroxyethylmetacrylate) nanocomposite films. Biomed Research International. 2013;2013:1-14.

102. Ul-Islam M*, et al.* Synthesis of regenerated bacterial cellulose-zinc oxide nanocomposite films for biomedical applications. Cellulose. 2014;21:433-447.

103. Brown T. Gene cloning & DNA analysis: an introduction. 7th Edition ed: Wiley-Blackwell; 2016. 376 p.

104. Segal L*, et al.* An empirical method for estimating the degree of crystallinity of native cellulose using the X-ray diffractometer. Textile Research Journal. 1959;29:786-794.

105. Krässig H. Cellulose: structure acessibility and reactivity. Netherlands: CRC Press; 1993. 240 p.

106. Lee K, Bismarck A. Susceptibility of never-dried and freeze-dried bacterial cellulose towards esterification with organic acid. Cellulose. 2012;19:891-900.

107. Panta G, Subedi D. Electrical characterization of aluminium (Al) thin films measured by using four-point probe method. Kathmandu University Journal of Science, Engeneering and Technology. 2012;8:31-36.

108. Stalder A*, et al.* A snake-based approach to accurate determination of both contact points and contact angles. Colloids and Surfaces A. 2006;286:92-103.

109. Cordeiro N*, et al.* Natural fibers characterization by inverse gas chromatography. Carbohydrate Polymers. 2011;84:110-117.

110. Zeng M*, et al.* Bacterial cellulose films: influence of bacterial strain and drying route on film properties. Cellulose. 2014;21:4455-4469.

111. Ishii D*, et al.* Effect of solvent exchange on the supramolecular structure, the molecular mobility and the dissolution behavior of cellulose in LiCl/DMAc. Carbohydrate Research. 2008;343:919-928.

112. Hasani M*, et al.* Nano-cellulosic materials: The impact of water on their dissolution in DMAc/LiCl. Carbohydrate Polymers. 2013;98:1565-1572.

113. Dupont A. Cellulose in lithium chloride/N,N-dimethylacetamide, optimisation of a dissolution method using paper substrates and stability of the solutions. Polymer. 2003;44:4117-4126.

114. Fan M*, et al.* Fourier Transform Infrared Spectroscopy for natural fibres. In: S. S, editor. Fourier Transform - Materials Analysis: InTech; 2012. p. 45-68.

115. Yudianti R*, et al.* Properties of bacterial cellulose transparent film regenerated from dimethylacetamide-LiCl solution. Polymers Advanced Technologies. 2016;27:1102-1107.

116. Cheng K*, et al.* Enhanced production of bacterial cellulose by using a biofilm reactor and its material property analysis. Journal of Biological Engeneering. 2009;3.

117. Tsouko E*, et al.* Bacterial cellulose production from industrial waste and by-product streams. International Journal of Molecular Sciences. 2015;16:14832-14849.

118. Liu Z*, et al.* Characterization of the regenerated cellulose films in ionic liquids and rheological properties of the solutions. Materials Chemistry and Physics. 2011;128:220-227.

119. Abbott A, Bismarck A. Self-reinforced cellulose nanocomposites. Cellulose. 2010;17:779-791.

120. Zugenmaier P. Crystalline cellulose and derivatives: characterization and structures. 1st Edition ed: Springer; 2008. 285 p.

121. Liu D*, et al.* Cellulose nanofibril core-shell silica coatings and their conversion into thermally stable nanotube aerogels. Journal of Materials Chemistry A. 2015;3:15745-15754.

122. Alongi J*, et al.* Thermal stability, flame retardancy and mechanical properties of cotton fabrics treated with inorganic coatings synthesized through sol-gel processes. Carbohydrate Polymers. 2012;87:2093-2099.

123. Brancatelli G*, et al.* Effect of hybrid phosphorus-doped silica thin films produced by sol-gel method on the thermal behavior of cotton fabrics. Polymer Degradation and Stability. 2011;96:493-490.

124. Perotti G*, et al.* Bacterial cellulose as a template for preparation of hydrotalcite-like compounds. Journal of Brazilian Chemical Society. 2014;25:1647-1655.

125. Yeng L*, et al.* Thermal and flexural properties of regenerated cellulose (RC)/poly(3-hydroxybutyrate)(PHB)biocomposites. Jurnal Teknologi. 2015;75:107-112.

126. Chen C*, et al.* Bacterial cellulose: the nano-scalar cellulose morphology for the material of transparent regenerated membrane. Advanced Materials Research. 2012;586:30-38.

127. Czaja W, Krystynowicz, A., Bielecki, S., Brown, R. Microbial cellulose - the natural power to heal wounds. Biomaterials. 2006;27:145-151.

128. Ul-Islam M*, et al.* Water holding and release properties of bacterial cellulose obtained by *in situ* and *ex situ* modification. Carbohydrate Polymers. 2012;88:596-603.

129. Silva C*, et al.* Wettability and morphological characterization of a polymeric bacterial cellulose/corn starch membrane. Materials Research. 2015;18:109-113.

130. Lee K*, et al.* Surface functionalisation of bacterial cellulose as the route to green polylactide nanocomposites with improved properties. Composites Science and Technology. 2009;69:2724-2733.

131. Lopes T*, et al.* Bacterial cellulose and hyaluronic acid hybrid membranes: production and characterization. International Journal of Biological Macromolecules. 2014;67:401-408.

132. Papirer E*, et al.* Inverse gas chromatography investigation of the surface properties of cellulose. Journal of Adhesion Science and Technology. 2000;14:321-337.

133. Castro C*, et al. In-situ* glyoxalization during biosynthesis of bacterial cellulose. Carbohydrate Polymers. 2015;126:32-39.

134. Ferguson A*, et al.* Understanding the dispersion and assembly of bacterial cellulose in organic solvents. Biomacromolecules. 2016;X:X.

135. Pommet M*, et al.* Surface modification of natural fibers using bacteria: depositing bacterial cellulose onto natural fibers to create hierarchical fiber reinforced nanocomposites. Biomacromolecules. 2008;9:1643-1651.

136. Gamelas J. The surface properties of cellulose and lignocellulosic materials assessed by inverse gas chromatography: a review. Cellulose. 2013;20:2675-2693.

137. Trchová M, Stejskal J. Polyaniline: the infrared spectroscopy of conducting polymer nanotubes (IUPAC Technical Report). Pure and Applied Chemistry. 2011;83:1803-1817.

138. Langer J. N-substituted polyanilines II. Photoacoustic and FT-IR spectra of poly(N-methylaniline) and related copolymers. Synthetic Metals. 1990;35:301-305.

139. Kaur G. AR, Cass P., Bown M., Gunatillake P. Electrically conductive polymers and composites for biomedical applications. RSC Advances. 2015;5:37553-37567.

140. Liu M*, et al.* Influence of the doping conditions on the surface energies of conducting polymers. Synthetic Metals. 1994;63:67-71.

141. Jiang S*, et al.* Enhanced drug loading capacity of polypyrrole nanowire network for controlled drug release. Synthetic Metals. 2013;163:19-23.

142. Neligan P. Plastic surgery E-book: 6 3th Edition ed. G. G, editor: Saunders; 2013. 5648 p.